論文 / 著書情報
Article / Book Information

題目(和文)	電圧スイングとヘテロポリ酸を用いた高活性Tio[2]光触媒コーティングの設計
Title(English)	Design and photocatalytic activity of TiO[2] coatings by using voltage swing and heteropolyacids
著者(和文)	柳田さやか
Author(English)	Sayaka Yanagida
出典(和文)	学位:博士(工学), 学位授与機関:東京工業大学, 報告番号:甲第7549号, 授与年月日:2009年3月26日, 学位の種別:課程博士, 審査員:中島 章,岡田 清
Citation(English)	Degree:Doctor (Engineering), Conferring organization: Tokyo Institute of Technology, Report number:甲第7549号, Conferred date:2009/3/26, Degree Type:Course doctor, Examiner:,
学位種別(和文)	博士論文
Type(English)	Doctoral Thesis

平成 20 年度学位論文

Design and Photocatalytic Activity of TiO_2 coatings by using Voltage Swing and Heteropolyacids

電圧スイングとヘテロポリ酸を用いた高活性 TiO_2 光触媒コーティングの設計

東京工業大学大学院
大学院理工学研究科　材料工学専攻

柳田　さやか

Contents

CHAPTER 1 (Introduction)

CHAPTER 2 (Photocatalytic Decomposition Improvement using Electrophoretic Deposition and Voltage Application)

CHAPTER 3 (Preparation of Heteropolyacid-intercalated Layered Double Hydroxide)

CHAPTER 4 (Preparation of Keggin-type Heteropolyacid and Isopolyacid-TiO_2 hybrid thin films)

CHAPTER 5 (Photocatalytic Activity of Keggin-type Polyacid and TiO_2 Hybrid thin Films)

CHAPTER 6 (Photocatalytic Decomposition of Hydrofluorocarbons)

CHAPTER 7 (Summary)

CHAPTER 1

Introduction

1.1. Titanium dioxide (TiO_2)

Titanium dioxide is a well-known ceramic material that is commonly called titania, represented by the composition formula TiO_2. It is a colorless solid material that is used in industry as a white pigment, catalyst, and dielectric substance. Actually, TiO_2 is harmless to human health. It has been used for a wide range of applications as a pigment for paint, paper, plastics, cosmetics, toothpastes, and as a food coloring.

Two main industrial processes have been used for TiO_2 production: sulfate and chloride processes. In the sulfate process, TiO_2 is obtained from its raw material (ilmenite ore) via dissolving and sintering. The chloride process is a gas-phase reaction. Raw material (rutile ore or synthetic rutile) is reacted with Cl_2 gas and coke at 1000°C; then gas phase $TiCl_4$ is obtained. After gas purification, $TiCl_4$ is heated with O_2; then TiO_2 particles are obtained. High-purity TiO_2 is producible from both processes. However, the kind of impurity and TiO_2 surface condition depend on the processes [1].

Three main types of TiO_2 structures are rutile, anatase, and brookite. The rutile and anatase crystal structures are presented in **Fig. 1-1** [2]. Their X-ray data and physical properties are presented in **Tables 1-1** and **1-2** [1, 2]. Actually, TiO_2 of all types has a high refractive index ($n_D = 2.5$–2.9) and transparency for visible light. The types' respective chemical properties are the following: anatase and brookite change to rutile phase at high temperature (915°C and 650°C) [1]. Then they are dissolved in hot concentrated sulfuric acid and hydrofluoric acid, or dissolved using alkali fusion method. Under ambient air, they have high resistance against heat and chemicals. Because of such high stability, high brightness and low production cost, rutile and anatase have been produced commercially on a large scale as white pigments and fillers for various products [1]. Recently, demand for TiO_2 photocatalysts has increased and highly active anatase powders and coating sols have been produced by some chemical companies. Rutile and brookite are also produced, however for photocatalyst use, anatase is commonly used because of its high activity.

1.2. TiO_2 photocatalyst

1.2.1. Historical overview

The photocatalytic reaction itself has been well known among chemists and chemical engineers for many years: since the 1960s [3, 4]. In 1972, Fujishima and Honda discovered the photocatalytic splitting of water using rutile single crystal electrode [5], thereafter reporting the Honda–Fujishima effect, as presented in **Fig. 1-2**. Early research was aimed at H_2 generation from water and sunlight. However, TiO_2 photocatalysts can use only UV photons (ca. 5% in sunlight), so their quantum efficiency is quite low for practical energy conversion. Research efforts in enhancing the photocatalytic efficiency of TiO_2 and in preparing visible-light sensitive photocatalysts have been continuing.

An early study of TiO_2 application to environmental cleanup using artificial light was reported by Bird and co-workers [6] in 1977. Photogenerated holes on TiO_2 photocatalyst have strong oxidation power and decompose organic substance unselectively on the TiO_2 surface. This approach attracted the interest of many researchers. Subsequently, fundamental studies were undertaken.

In the 1990s, the Fujishima group and Toto Ltd. began to develop practical applications of TiO_2 for building materials. They also found photo-induced super hydrophilic effects in 1997 [7], it extended TiO_2 application for anti-fogging and self-cleaning coating. The number of research papers describing TiO_2 photocatalysts increased rapidly with development of its practical use. Practical application examples are presented in **Table 1-3** [8].

Recently, increased photocatalytic performance under weak UV light or visible light has been noted from the perspective of “passive photocatalysis” [9], which requires no special light source such as a UV lamp, and which works continuously under sunlight or indoor light. It would be an important approach for energy conservation and wide application of photocatalytic materials.

1.2.2. Mechanism of photocatalytic reaction

Actually, TiO_2 is a semiconductor photocatalyst: it has valence band consisting of O 2p orbitals and a conduction band consisting of Ti 3d orbitals. Oxidation and reduction levels of several semiconductor photocatalysts are presented in **Fig. 1-3** [10]. Furthermore, TiO_2 has a large band gap (3.2 eV for anatase and 3.0 eV for rutile); its photogenerated holes have high oxidation potential. **Figure 1-4** [11] shows the bonding energies of covalent bonds in organic compounds. Holes have sufficient oxidation power for decomposition without C–F bonding. The reduction potential is also sufficient for O_2 reduction. In addition, photocorrosion does not occur when TiO_2 is illuminated with UV. These are great advantages of TiO_2 for use as a practical photocatalyst. Anatase exhibits higher photocatalytic activity than rutile and is used in many cases. The small crystalline size of anatase, high electron mobility [12], and surface structure are considered reasons for its high performance.

When UV is illuminated onto a TiO_2 surface, electrons in the valence band are excited and hole and electron pairs are generated. Most holes and electrons are recombined and disappear with heat emission. However, some are diffused and trapped on the TiO_2 surface. Subsequently, reduction and oxidation occur on the TiO_2 surface (**Fig. 1-5**). Generally, photocatalytic reaction is defined as whole reactions including reduction by photogenerated electrons, oxidation by photogenerated holes, and series of radical reactions result of holes and electrons reaction. **Figure 1-6** shows a timescale of the photoexcitation [9]. The O_2 reduction is slow; it often becomes a late controlled step in all reactions.

In most cases, organic substance decomposition is initiated with an oxidation reaction. Free and trapped holes oxidize organic compounds directly and the generated radicals react indirectly with organic compounds. The kind and amount of radical species generated from redox on a TiO_2 surface were investigated. However, radical detection is difficult because of their short lifetimes. Free and trapped holes, $\cdot OH$ radicals, hydrogen peroxide (H_2O_2), super oxide ($O_2^{-}\cdot$), and $^1O_2$ were detected using flash photocatalysis and transient spectroscopy [13–15]. Proposed redox paths are presented in **Fig. 1-7**. Radicals and H_2O_2 can diffuse into air. Therefore, photocatalytic reactions occur not only at the TiO_2 surface but also near the surface [16, 17]. Finally, almost all organic compounds are mineralized to CO_2 and H_2O by photocatalytic reactions. However, the contribution of holes and each radical to decomposition has been discussed.

1.3. Environmental purification of the photocatalyst

1.3.1. Air purification

As described in section 1.2.1, environmental purification using TiO_2 photocatalysts has been attempted since the late 1970s [6]. In gaseous reactions, the photocatalytic decomposition rate depends on the kind and concentration of organic compound, light intensity, and humidity. Humidity is an important factor because H_2O and organic substances are competitively adsorbed onto the TiO_2 surface. The amount of H_2O can also affect radical generation on the TiO_2 surface. Generally, the decomposition rate is high because of the large diffusion constant in air; then the reaction tends to be controlled by light intensity. **Figure 1-8 (a)** portrays a TiO_2 surface in the surface-reaction controlled reaction. When the substance concentration is high and the light intensity is insufficient, the rate of surface reaction dominates the total decomposition rate.

To date, air purification is an extremely successful application of the TiO_2 photocatalyst. Photocatalytic decomposition of harmful volatile organic compounds (VOCs) such as formaldehyde [18], acetaldehyde [19], toluene [20, 21], and halocarbons [22, 23] have all been reported. In addition, TiO_2 can decompose bacteria and viruses. In fact, TiO_2-supported filters are employed in air purification systems for buildings.

1.3.2. Water purification

Most organic pollutants including aliphatic carbons, aromatic carbons, halocarbons, and polymers in water can be decomposed and mineralized completely through TiO_2 photocatalysis. The list of decomposed compounds was presented in Hoffman's review [13]. Although only UV light and O_2 are necessary for the reactions, many factors such as light intensity, pH, ions, kinds and concentrations of substrates, etc., have a great influence on the efficiency of the mineralization process. In aqueous phase, the decomposition rate was low because of the low diffusion constant (10^{-4} times as large as gaseous reaction): decomposition tends to be controlled by reactants and product diffusion (**Fig. 1-8 (b)**). Actual TiO_2 photocatalysis is regarded as feasible only for treatment of wastewater containing contaminants at low concentrations. Its water purification capability does not approach the level necessary for practical use. In combination with other methods, hybridization with other materials and addition of electron acceptors such as H_2O_2 or $S_2O_8^{2-}$ [24] are considered effective for acceleration of decomposition. Application areas for aqueous phase photocatalysis are drinking water disinfection for safe water supply [25], remediation of metal contaminants [26], and oxidation of arsenite [27]. For large-scale environmental water purification, the effective use of sunlight is important.

1.4. Preparation of High-performance TiO_2

1.4.1. Hybridization

To date, numerous studies have investigated improvement of the decomposition activity of TiO_2 photocatalysts against various target compounds. Surface modification using metals, other semiconductors, and adsorbents is an effective method. The photocatalytic activity of TiO_2 is enhanced remarkably by the addition of small amounts of noble metals such as Pt or Rh [28], which is explainable by the quick transfer of photogenerated electrons in TiO_2 semiconductors to the loaded metal particles (**Fig. 1-9(a)**). It provides efficient charge separation and prevents electron–hole recombination. An ESR study revealed the charge separation effect. **Figure 1-10** shows the growth of ESR signals attributed to Ti^{3+}, which were generated on Pt-loaded TiO_2 and unloaded TiO_2 photocatalysts under UV light irradiation [29]. The Ti^{3+} site is expected to arise from the Ti^{4+} site at which the photogenerated electrons are trapped. These results indicate clearly that photogenerated electrons in the Pt-loaded TiO_2 quickly transfer from TiO_2 to Pt particles. In addition, Pt is expected to enhance reduction by its catalytic property.

Hybridization of TiO_2 with adsorbent is another way to enhance decomposition for air and water purification. Usually, the concentration of the contaminant is very low in the environment (0.002–10 ppm). Therefore, decomposition reactions are often controlled by diffusion processes. As an absorbent, SiO_2 [30–32], activated carbon [33, 34], zeolite [35], and apatite [36] are used. Photocatalytic performance was increased by adsorbent loading in both gaseous and aqueous phase reactions. Suggested decomposition mechanisms are presented in **Fig. 1-9(b)**: (1) adsorbed molecules diffuse to the TiO_2 surface and are decomposed; (2) generated radicals on TiO_2 photocatalyst are diffused near the adsorbed molecule and are attacked. By virtue of these mechanisms, TiO_2-adsorbent photocatalysts have been used in air purifiers.

1.4.2. Visible-light-induced photocatalysis

Rutile and anatase mainly adsorbed UV light (< 400 nm) because of their wide band gaps. Nevertheless, solar light contains few UV photons (ca. 5%), and room light lamps emit mainly visible photons. Extending the spectral response of pure TiO_2 to visible light has been studied to increase reaction efficiency under these light sources. Metal and non-metal doping was attempted to introduce impurity levels between the TiO_2 band gap for narrowing the band gap. **Figure 1-11** presents an energy band model for pure TiO_2 and doped TiO_2 [9, 37]. For metal-doped TiO_2, Visible light adsorption occurs, but its activity is very low; the reduction level is insufficient for O_2 reduction and the doped ion is considered to be a charge recombination center. Recently, many researchers have investigated non-metal doping (N, S, C) [38–40]. In such cases, the conduction band is not changed and the impurity band is introduced near the valence band. These photocatalysts have a sufficient reduction level and decomposition occurs under visible light. Nevertheless, their activities have remained low. Therefore, many efforts have been devoted to increasing quantum efficiency under visible light.

Recently, Cu (II)-ion-grafted TiO_2 and WO_3 were reported as visible-light-sensitive photocatalysts [41]. Electrons in the TiO_2 valence band are transferred to Cu ions directly through interfacial charge transfer (IFCT) under visible light illumination (>400 nm) and catalytic multi-electron reduction of O_2 occur on Cu (I). It has been anticipated as a novel approach for designing visible light-sensitive photocatalysts.

1.5. Objective and strategy of present work

Fundamental and application-based studies of photocatalysts have advanced rapidly during the last decade. Highly active photocatalytic materials have been found. Nevertheless, TiO_2 is regarded as the most practical, widely applicable photocatalyst because of its high abundance and low cost. However, increased TiO_2 photocatalytic activity through manipulation of the crystalline shape and phase control must have a limit. Low affinity between TiO_2 surfaces and organic molecules and low charge separation efficiency are problems of TiO_2 photocatalytic decomposition. Especially in aqueous phase decomposition, the practical use of TiO_2 photocatalysts is only slightly developed because of slow diffusion and adsorption difficulty.

In previous works, hybridization of TiO_2 with adsorbents and combination with external field (magnetic field [42] and electric field [43]) or other methods (microwave [44], ultrasonic wave [45], etc.) have been carried out for increasing decomposition performance. However, in those studies, only hybridization was carried out: the effects of the material arrangement and adsorption field structure were discussed only slightly. The concept of nano–micro-scale catalyst design based on the decomposition condition has been lacking.

Actually, Pt loading is a successful method for increasing the charge separation efficiency. Unfortunately, it radically increases the photocatalyst cost; therefore, Pt-TiO_2 hybrids are not applicable to large scale applications. Pt nanoparticles on a TiO_2 surface show a black color therefore transparent coating is difficult for preparation. That Z-scheme (explained later in chapter 4) is another method to prevent hole-charge recombination. High efficiency was obtained for water splitting [46, 47]. However, the system requires a charge mediator for electron transfer. For that reason, almost all studies examine suspension systems: only Tada et al. have reported an all-solid-state Z-scheme (TiO_2-Ag -CdS hybrid [48]). In these cases, the rates of electron transfer and O_2 reduction are important. For wide application, transparent thin film coating is desirable because it provides high visibility and does not hide the substrate color. In view of the points described above, the research objectives of this study can be described as follows:

Presentation of a design concept of an adsorption and reaction field in nano–micro-scale based on decomposition target properties

Strategies:

- 1,4-dioxane decomposition in water
- Layer structure control by electrophoretic deposition.
- Application of an electric field

Proposal of a new hybrid system for high separation efficiency and preparation of transparent nanocoatings

Strategies:

- High adsorption capabilities of heteropolyacids
- Two-step photoexcitation in TiO_2-heteropolyacid system
- Layer-by-layer method
- Heteropolyacid-layered double hydroxide hybridization

From these approaches, new methods and concepts for TiO_2-based photocatalysts were developed. All contents are described in chapters 2–6.

References

[1] Kiyono, M. *Sankatitan*, Gihodoshuppan Co., Ltd.: Tokyo (1991) in Japanese.

[2] Diebold, U. *Surf. Sci. Rep.*, **48**(5-8), 53-229 (2003).

[3] Markham, M. C.; Laidler, K. J. *J. Phys. Chem.* **57,** 363-369 (1953).

[4] Kennedy, D. R.; Ritchie, M.; Mackenzie, J. *Trans. Faraday Soc.*, 54 (1958).

[5] Fujishima, A.; Honda, K.; *Nature*, **238**, 37-38 (1972).

[6] Flank, S. N.; Bird. A. J. *J. Am. Chem. Soc.*, **99**, 103-104 (1977).

[7] Wang, R.; Hashimoto, K.; Fujishima, A.; Chikuni, M.; Kojima, E.; Kitamura, A.; Shimohigoshi, M.; Watanabe, T.; *Nature*, **388**, 431-432 (1997).

[8] Hashimoto, K.; Ohtani, B.; Kudo, A. *Photocatalyst*, NTS Inc.: Tokyo (2005). in Japanese.

[9] Fujishima, A.; Zhang, X.; Tryk, D. A. *Surf. Sci. Rep.*, **63**, 515-582 (2008).

[10] Hashimoto, K.; Fujishima, A. *Ceramics*, **31**, 815 (1996).

[11] Horikoshi, S.; Abe, M. *J. Jpn. Soc. Mater.*, **81**(11), 449-458 (2008).

[12] Kavan, L.; Grätzel, M.; Gilbert, S. E.; Klemenz, C.; Scheel, H. J. *J. Am. Chem. Soc.*, **118**(28), 6716-6723 (1996).

[13] Hoffmann, M. R.; Martin, S. T.; Choi, W.; Bahnemann, D. W. *Chem. Rev.*, **95**, 69-96 (1995).

[14] Nosaka, Y.; Daimon, T.; Nosaka, A.; Murakami, Y., *Phys. Chem. Chem. Phys.*, **6**(11), 2917-2918 (2004).

[15] Tachikawa, T.; Fujitsuka, M.; Majima, T. *J. Phys. Chem. C*, **111**, 5259-5275 (2007).

[16] Tatsuma, T.; Tachibana, S.; Miwa, T.; Tryk, D. A.; Fujishima, A. *J. Phys. Chem. B*, **103**, 8033-8035 (1999).

[17] Kubo, W.; Tatsuma, T. *J. Am. Chem. Soc.*, **128**, 16034-16035 (2006).

[18] Peral, J.; Ollis, D. F. *J. Catal.*, **136**, 554-565 (1992).

[19] Sopyan I.; Watanabe M.; Murasawa S.; Hashimoto K.; Fujishima A. *J. Photochem. Photobiol. A: Chem.*, **98**(1-2), 79-86 (1996).

[20] Butler, E. C.; Davis, A. P. *J. Photochem. Photobiol. A: Chem.*, **70**, 273-283 (1993).

[21] Lichtin, N. N.; Dong, J.; Vijayakumar, K. M. *Water Pollut. Res. J. Can.*, **27**, 203-210 (1992).

[22] Kormann, C.; Bahnemann, D. W.; Hoffmann, M. R. *Environ. Sci. Technol.*, **25**, 494-500 (1991).

[23] Ozaki, S.; Zhao, L.; Amemiya, T.; Itoh, K.; Murabayashi, M. *Appl. Catal. B: Environ.*, **52**(2), 81-89 (2004).

[24] Agustina, T. A.; Ang, H. M.; Vareek, V. K. *J. Photochem. Photobiol. C: Photochem., Rev.*, **6**, 264-273 (2005).

[25] McCullagh, C.; Robertson, J. M. C.; Bahnemann, D. W.; Robertson, P. K. *J. Res. Chem. Intermediates*, **33**(3-5), 359-375 (2007).

[26] Litter, M. I. *Appl. Catal. B: Environ.*, **23**, 89-114 (2004).

[27] Ferguson, M. A.; Hoffmann, M. R.; Hering, J. G., *Environ. Sci. Technol.*, **27**, 1776-1782 (2005).

[28] Sato, S.; White, J. M. *Chem. Lett.*, **72**, 83-86 (1980).

[29] Anpo, M.; Takeuchi, M. *J. Catal.*, **216**, 505-516 (2003).

[30] Anderson, C.; Bard, A. J. *J. Phys. Chem. B,* **101**(14), 2611-2616 (1997).

[31] Tada, H.; Akazawa, M.; Kubo, Y.; Ito, S. *J. Phys. Chem. B,* **102**(33), 6360-6366 (1998).

[32] Jung, K. Y.; Park, S. B. *Appl. Catal. B: Environ.* **25**(4), 249-256 (2000).

[33] Uchida, H. Itoh, S.; Yoneyama, M. *Chem. Lett.*, 1995 (1993).

[34] Tryba, B.; Morawski, A. W.; Inagaki, M. *Appl. Catal. B: Environ.*, **41**(4), 427-433 (2003).

[35] Xu, Y.; Langford, C. H. *J. Phys. Chem. B,* **101**, 3115-3121 (1997).

[36] Nakajima, A.; Takakuwa, K.; Kameshima, Y.; Hagiwara, M.; Sato, S.; Yamamoto, Y.; Yoshida, N.; Watanabe, T.; Okada, K. *J. Photochem. Photobiol. A: Chem.*, **177**, 94-99 (2006).

[37] Umebayashi, T.; Yamaki, T.; Itoh, H.; Asai, K. *J. Phys. Chem. Solid*, 1909-1920 (2002).

[38] Asahi, R.; Morikawa, T.; Ohwaki, T.; Aoki, K.; Taga, Y. *Science*, **293**, 269-271 (2001).

[39] Tachikawa, T.; Tojo, S.; Kawai, K.; Endo, M.; Fujitsuka, M.; Ohno, T.; Nishijima, K., Miyamoto, Z.; Majima, T. *J. Phys. Chem. B*, **108**(50), 19299-19306 (2004).

[40] Chatterjee, D.; Dasgupta, S. *J. Photochem. Photobiol. C: Photochem. Rev.*, **6**, 186-205 (2005).

[41] Irie, H.; Miura, S.; Kamiya, K.; Hashimoto, K. *Chem. Phys. Lett.*, **457**, 202-205 (2008).

[42] Butterfield, I. M.; Christensen, P. A.; Curtis, T. P.; Gunlazuardi, J. *Water Res.*, **31**(3), 675-677 (1997).

[43] Wakasa, M.; Suda, S.; Hayashi, H.; Ishii, N.; Okano, M. *J. Phys. Chem.: B*, **108**(32), 11882-11885 (2004).

[44] Horikoshi, S.; Hidaka, H.; Serpone, N. *Environ. Sci. Technol.*, **36**(6), 1357-1366 (2002).

[45] Stock, N.L.; Peller, J.; Vinodgopal, K.; Kamat, P. V. *Environ. Sci. Technol.*, **34**(9),

1747-1750 (2000).

[46] Sayama, K.; Yoshida, R.; Kusama, H.; Okabe, K.; Abe, Y.; Arakawa, H. *Chem. Phys. Lett.*, **277**(4)**,** 387-391 (1997).

[47] Sasaki, Y.; Iwase, A.; Kato, H.; Kudo, A. *J. Catal.*, **259**(1), 133-137 (2008).

[48] Tada, H.; Mitsui, T.; Kiyonaga, T.; Akita, T.; Tanaka, K. *Nature Mater.*, **5**, 782-786 (2006).

(a) Rutile

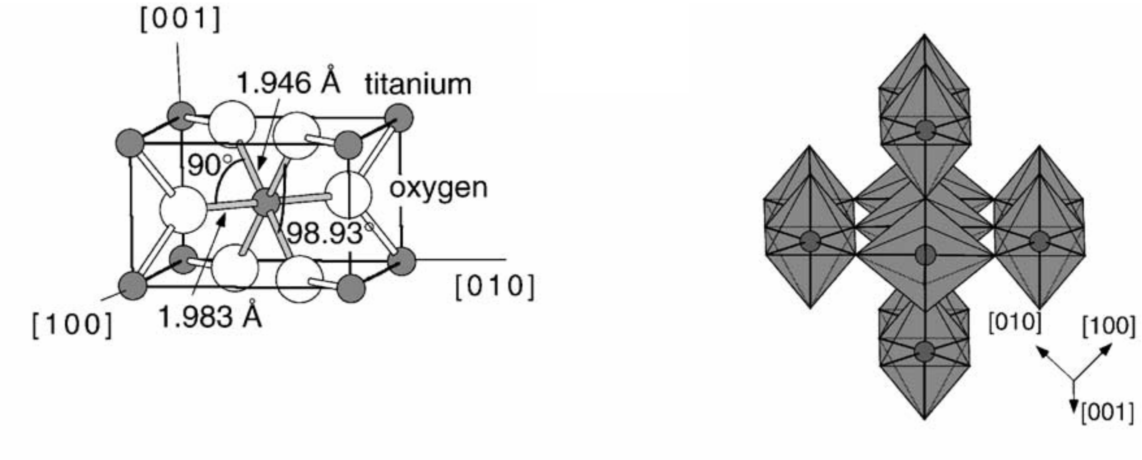

(b) Anatase

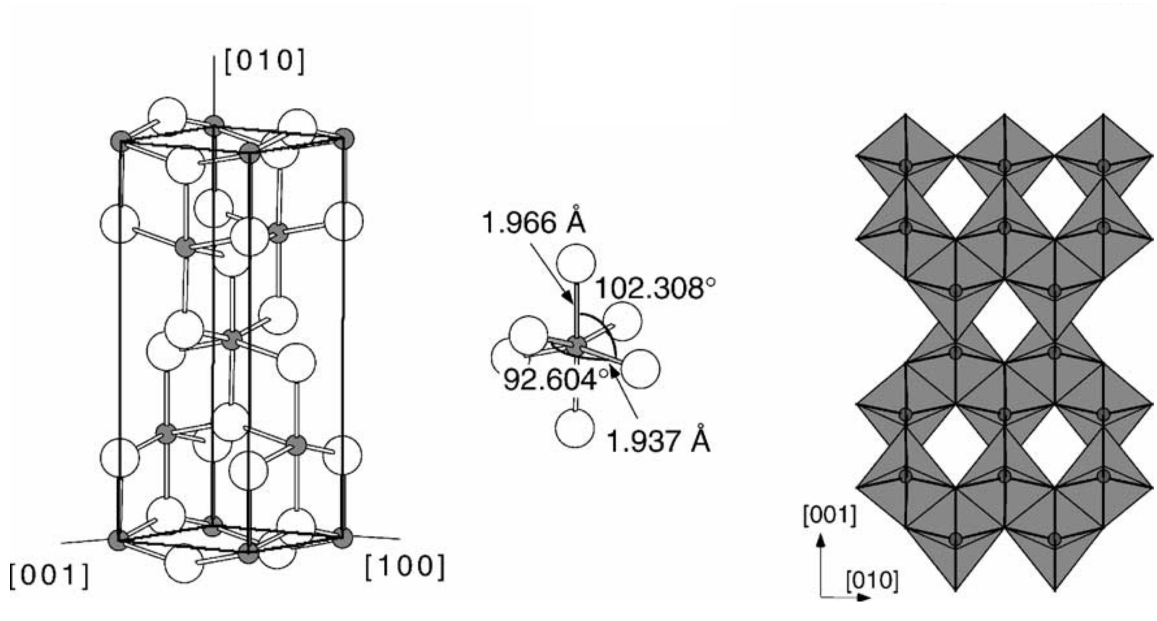

Figure 1-1. Crystal structures of rutile and anatase [2].

Table 1-1. Crystallographic data of TiO_2 polymorphs [1, 2]

	System	Space group	Z	Lattice parameter (Å)			Density (g cm^{-3})
				a	*b*	*c*	
Rutile	Tetragonal	D_{4h}^{14} = p4_2/mnm	2	4.5933		2.9592	4.250
Anatase	Tetragonal	C_{4h}^{19} = I4_1/amd	4	3.7852		9.5139	3.893
Brookite	Rhombohedral	D_{2h}^{15} = pbca	8	5.4558	9.1819	5.1429	4.14

Table 1-2. Physical properties of rutile, anatase, and brookite [1, 2]

	Rutile	Anatase	Brookite
Refractive index			
n_g	2.908	2.488	2.700
n_m	–	–	2.584
n_p	2.621	2.561	2.583
Mohs scale hardness	7.0–7.5	5.5–6.0	5.5–6.5
Heat capacity at 298.15 K (J/kg·K)	691.0	696.7	–
Linear coefficient of thermal expansion ($\alpha \times 10^{-6}$/ ºC)			
Parallel to c-axis	9.94	6.64	–
Perpendicular to c-axis	7.18	2.88	–
Electrical resistivity (Ωm)			
at 25ºC	10^{15}–10^{16}	10^{15}–10^{16}	–
at 500ºC	3×10^5	2×10^9	–
Permittivity	114	48	78 (a-axis)
Melting point (ºC)	1825	–	–

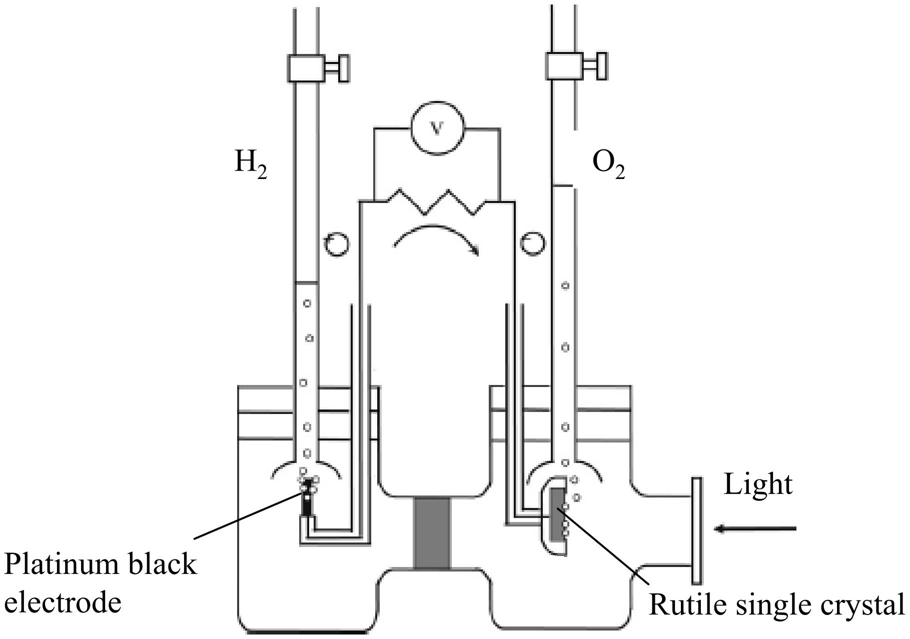

Figure 1-2. Photoelectrochemical cell used in the photolysis of water [9].

Table 1-3. Application of TiO_2 photocatalyst [8]

	Application	Light source	Reaction
Building Material	Wall paint Glass coating Mirror coating	Sunlight Indoor light	Decomposition Hydrophilic conversion
Indoor purification	Air purifier Water purifier Deodorizer	UV light Indoor light	
Outdoor purification	Air, wastewater, and soil purification	Sunlight	Decomposition
Energy saving	Cooling of building	Sunlight	Hydrophilic conversion

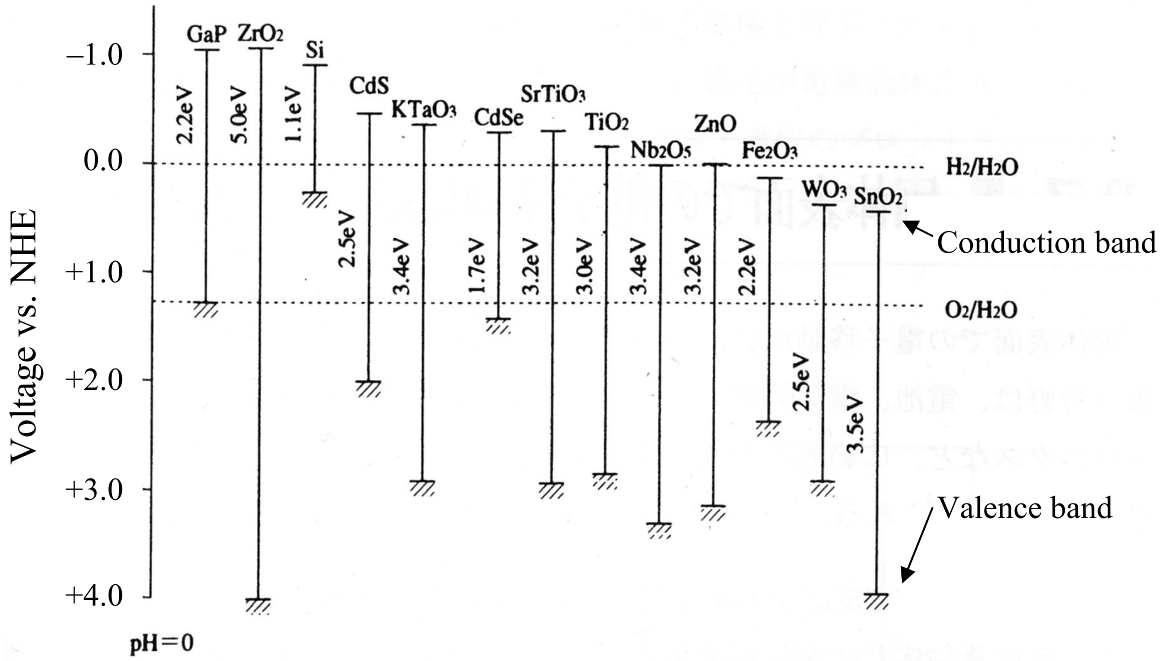

Figure 1-3. Energies for various semiconductors in aqueous electrolytes at pH = 0. [10]

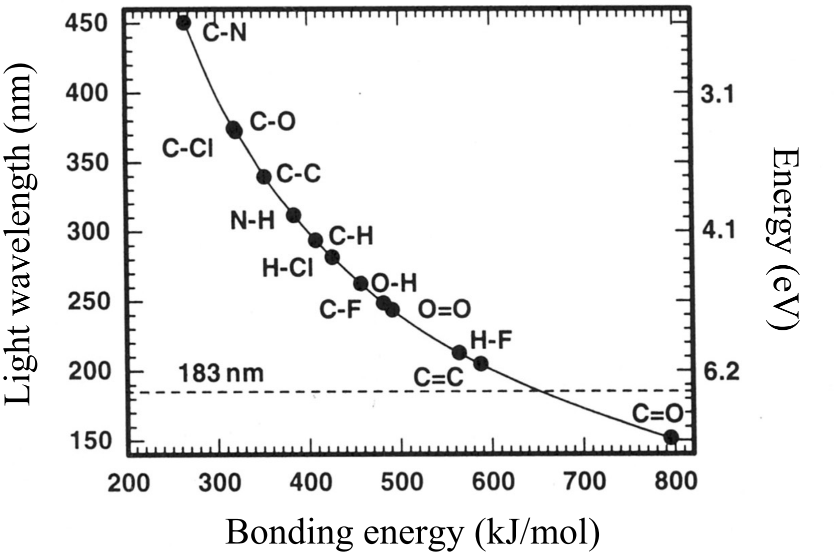

Figure 1-4. Bonding energy of covalent bond in organic molecules [11]

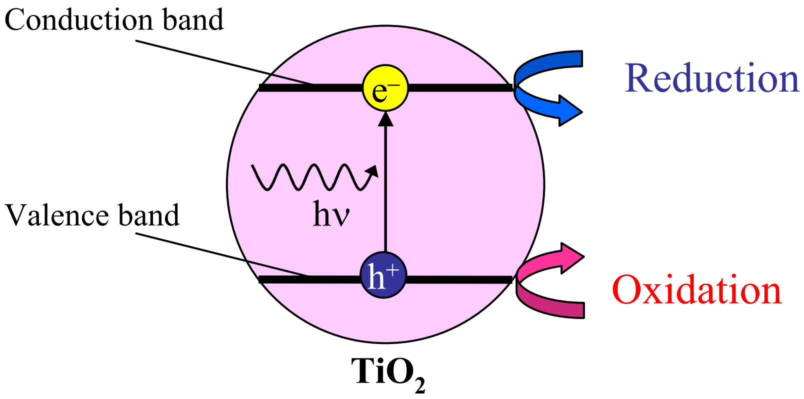

Figure 1-5. Energies for various semiconductors in aqueous electrolytes at pH = 1.

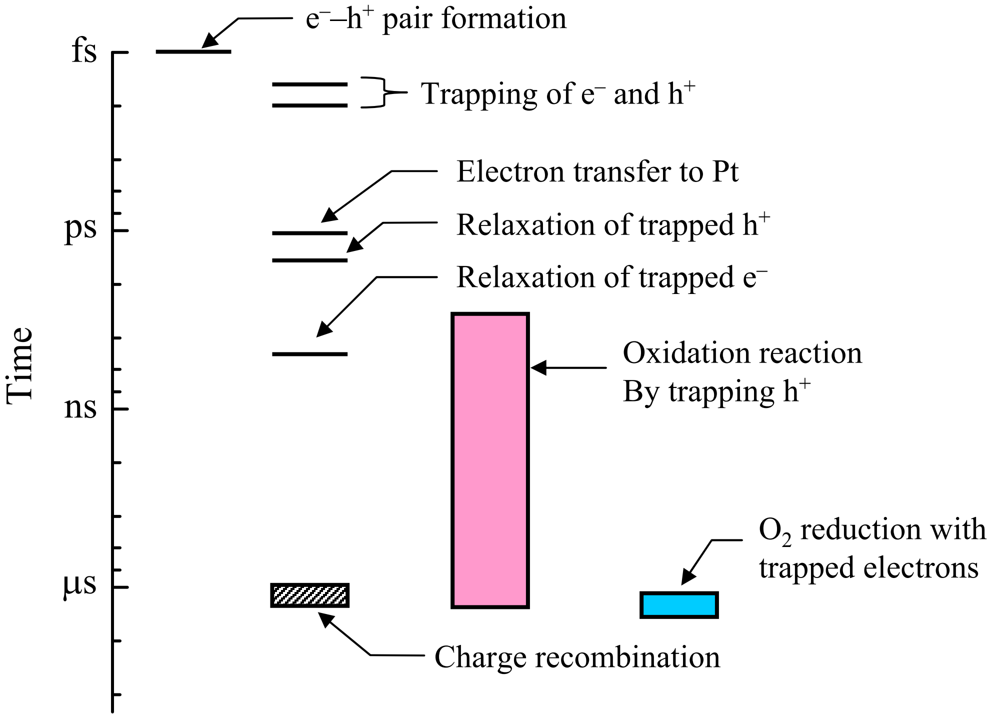

Figure 1-6. Time scales of photocatalytic reaction [9].

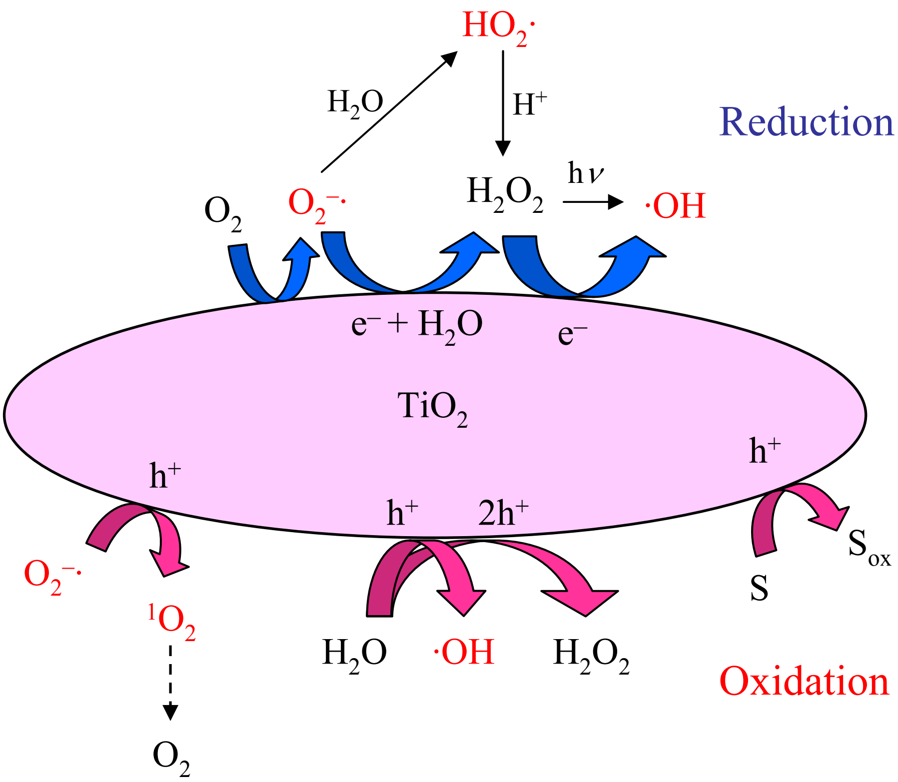

Figure 1-7. Organic substance (S) oxidation and radical generation on TiO_2 photocatalyst.

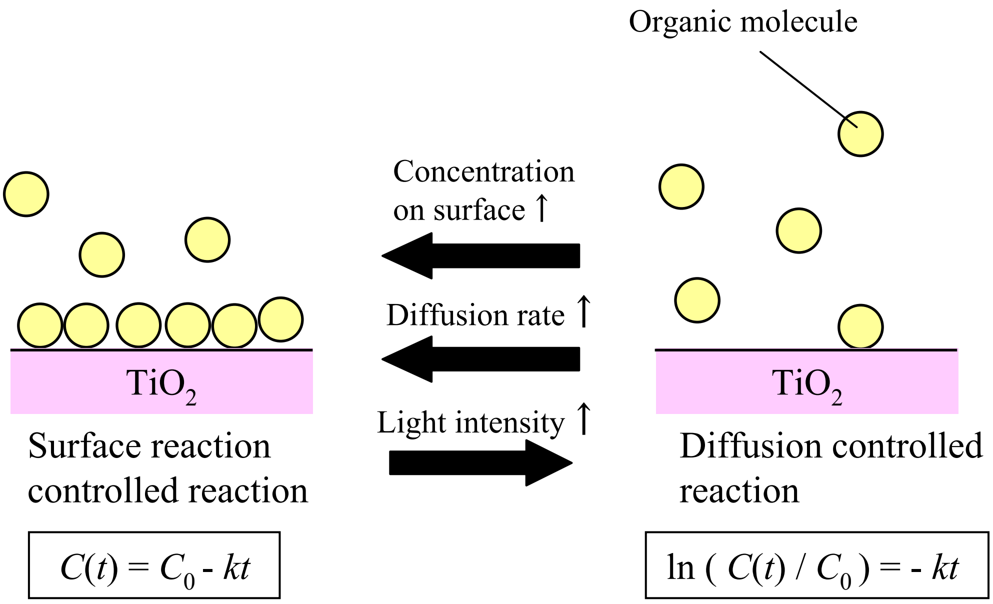

Figure 1-8. Rate-controlling reaction change by condition of photocatalytic reaction. $C(t)$, concentration of organic molecules; C_0, initial concentration.

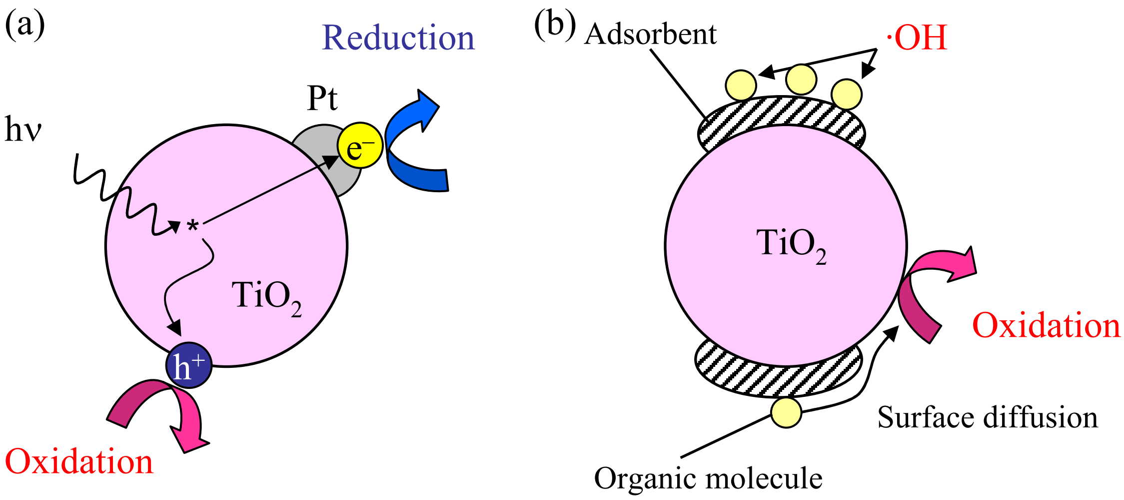

Figure 1-9. Reaction model of surface modified TiO_2 photocatalyst: (a) Pt loaded TiO_2, (b) Absorbent loaded TiO_2.

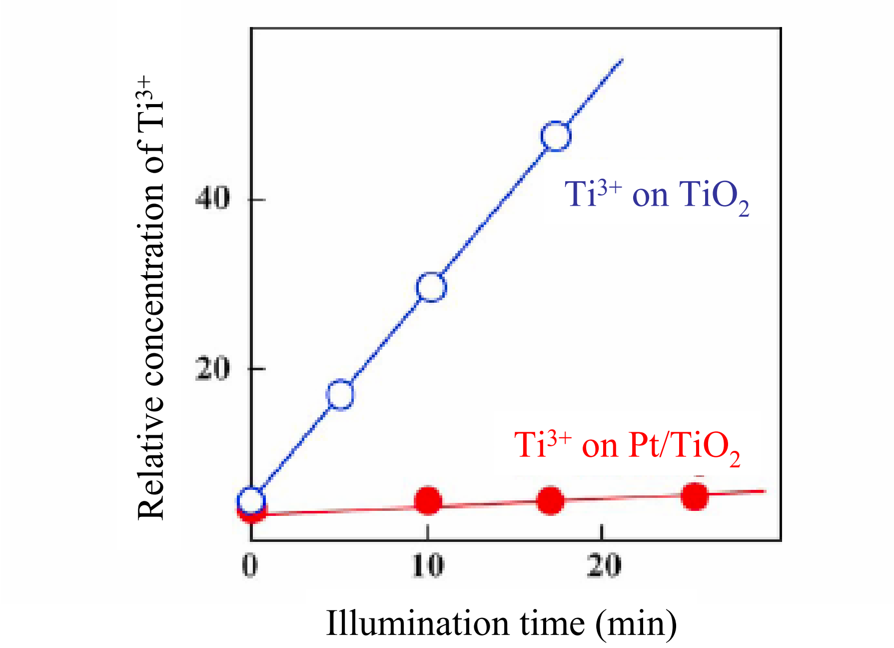

Figure 1-10. Ti valence change during UV illumination [29].

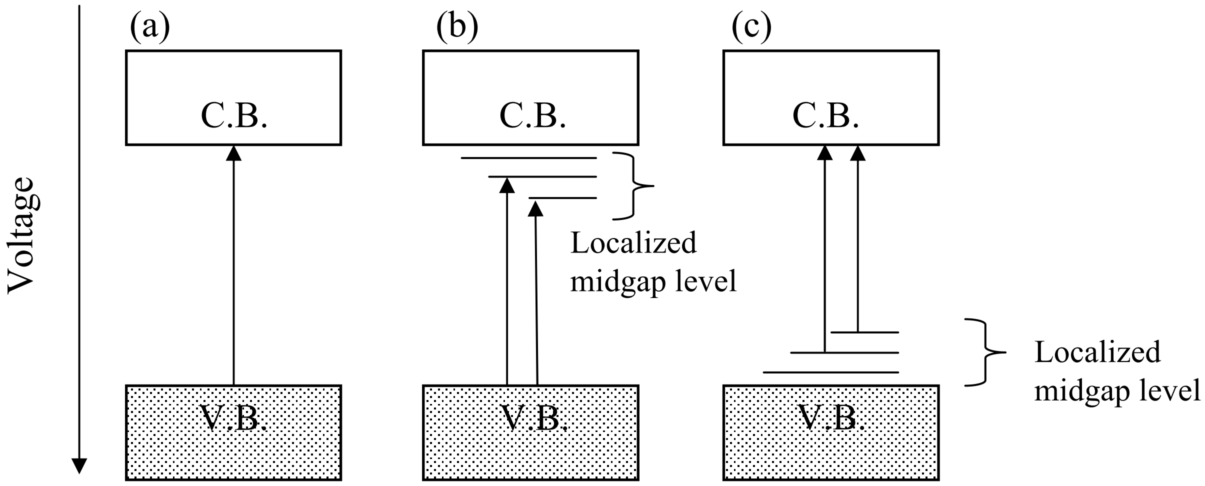

Figure 1-11. Band structure of pure and doped TiO_2: V.B., valence band; C. B., conduction band; (a) pure TiO_2; (b) Cr doped TiO_2; (c) N doped TiO_2.

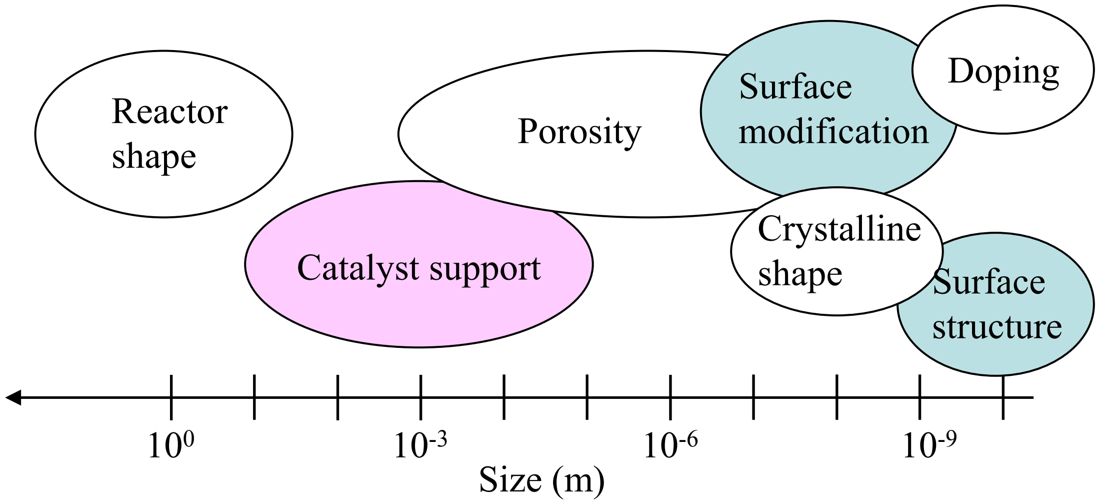

Figure 1-12. Factors contributed to performance of TiO_2 photolysis.

CHAPTER 2

Photocatalytic Decomposition Improvement using Electrophoretic Deposition and Voltage Application

2.1. Introduction

Direct use of TiO_2 powder for photocatalytic purification presents an obstacle to powder separation from treated air or water. For that reason, porous TiO_2 filters are commonly used for various systems. Such filters are commonly prepared by coating a TiO_2 sol, slurry, or precursor liquid onto porous ceramic substrates or ceramic foam by spray coating or dip coating [1]. Then, heat treatment at around 500°C is generally conducted after coating. Although porous metal substrates offer better toughness, better malleability, and lower cost than ceramic substrates, they are not used for photocatalyst filters. A principal weak point of metal substrates for this application is the generation of cracking or peeling of the surface TiO_2 coating after heat treatment because of the different thermal expansion coefficients of TiO_2 and the substrate metal. Investigations of a TiO_2 coating that develops no cracks or peeling on porous metal substrate during heat treatment remain insufficient.

As a solvent for 1,1,1-trichloroethane and as a stabilizer for chlorinated solvents, 1,4-dioxane has been used widely. This chemical, which is known as a by-product of some surfactant production processes [2], has physical properties resembling those of water (d = 1.03, b.p. = 101°C). For those reasons, 1,4-dioxane is widely believed to migrate swiftly throughout aquifers, and consequently, widely contaminate drinking water resources [3, 4]. Moreover, this compound apparently resists degradation in conventional industrial biotreatment processes and under aerobic and anaerobic conditions in natural environments [3, 4]. Monitoring by the Japanese Ministry of the Environment detected 1,4-dioxane at high frequencies in water, especially in groundwater [5]. In addition, the International Agency for Research on Cancer (IARC) has assigned 1,4-dioxane to Group 2B: Possibly carcinogenic to humans [6].

A treatment technology that is currently used for removing 1,4-dioxane from contaminated water streams is distillation [2]. However, because of its high affinity with water, precise condition controls are required; even if attained, the separation efficiency is low. Other treatments such as Fenton’s reagent [7], γ-ray irradiation [8], and sonolysis [9] do not provide sufficiently high efficiency for decomposition, nor do they meet practical requirements for water treatment. Consequently, development of a treatment method with a higher decomposition rate is necessary. Decomposition of 1,4-dioxane must be carried out in aqueous systems because of the difficulty in removing it from water. Advanced oxidation processes (AOPs) such as ozone/ UV treatment and TiO_2 photocatalysis are expected to be effective.

2.2. Electrophoretic Deposition (EPD)

Electrophoretic deposition (EPD) is one method to form a ceramic layer from powder suspensions. **Figure 2-1** is a schematic illustration of the EPD process. When an electric field is applied between electrodes, charged and suspended particles in the solution move toward oppositely charged electrodes. Consequently, particles are deposited on the electrode, forming a thick coating. Advantages of this method are: (1) applicability to large areas, (2) easy coating onto conductive substrates with complex shape, (3) easy control in coating thickness, and (4) low cost [10]. Various ceramic coatings have been prepared using this process to date [11]. Several researchers have performed titania coating by EPD on carbon and SiC fiber [12], conductive glass plate for dye-sensitized solar cell [13, 14], and metal fiber or plate [15, 16]. However, crack-free sintered bodies are difficult to prepare on metal substrate because of stress during shrinkage in drying and sintering.

Recently, we prepared a crack-free TiO_2 (anatase) coating on stainless mesh using EPD processing with an isopropyl alcohol (IPA)-based suspension [17]. The lower surface tension of IPA and its submicrometer size (200 nm) particle usage are preferable for suppressing stress. Rough surface TiO_2 coating was also prepared from pre-UV illuminated suspension. Rough coatings exhibited higher decomposition rates than smooth coatings [18].

2.3. Photocatalytic decomposition of 1,4-dioxane

Several researchers have examined photocatalytic decomposition of 1,4-dioxane in water and have identified a reaction pathway [19, 20] (**Fig. 2-2**). Ethylene glycol diformate (EGDF) generation from 1,4-dioxane is the primary step, and EGDF decomposed to ethylene glycol monoformate (EGMF). Finally, 1,4-dioxane is decomposed to CO_2 and H_2O. Once EGDF is destructed, no intermediate with a slow decomposition rate exists in the following oxidation reaction by photocatalysis. Therefore, promoting the decomposition of EGDF is an important requirement for mineralization of 1,4-dioxane by photocatalysis in aqueous systems. Hybridization of functional materials with TiO_2 is an effective approach to improve the decomposition efficiency. Nakajima et al. combined $Cs_{2.5}H_{0.5}PW_{12}O_{40}$, a solid acid, with TiO_2 and enhanced EGDF adsorption and decomposition in 1,4-dioxane photocatalysis [21]. Combination of the TiO_2 photocatalytic reaction with other reactions or methods is another approach to accelerate decomposition. Maurino and Coleman et al. investigated the combined effect of radical reaction by peroxides and TiO_2 [19, 22]. The presence of peroxydisulfate ($S_2O_8^{2-}$) enhances the photocatalytic decomposition of 1,4-dioxane [19]. Nakajima et al. revealed that HF-treated TiO_2 and an ultrasonication combination system is effective for 1,4-dioxane decomposition [23]. The HF-TiO_2 surface enhances its absorption capabilities for both 1,4-dioxane and EGDF while improving the overall decomposition rate of 1,4-dioxane through sonophotocatalytic treatment. They also reported that TiO_2 particle addition accelerates sonochemical reactions [24].

In the current work, we applied voltage to a stainless mesh coated with TiO_2 powder by EPD and examined its synergy effect on photocatalysis of both 1,4-dioxane and EGDF.

2.4. Experimental Procedure

2.4.1. Preparation of TiO_2 coated stainless mesh

The method of preparing TiO_2-coated stainless mesh is identical to those described for a previous study [17]. Commercial high purity TiO_2 (anatase) powder (ST-41; Ishihara Sangyo Kaisha Ltd., Osaka, Japan) was dispersed into reagent grade 2-propanol (concentration: 2.0 g powder/100 ml IPA, purity: 99.5%; Wako Pure Chemical Industries Ltd., Tokyo, Japan). After stirring for 60 min, ultrasonication was conducted for 10 min. Thereby, a stable suspension was obtained. The stainless steel mesh (SUS 316; wire diameter, 0.375 mm; open area, 0.64 × 1.04 mm; P-type; Nippon Filcon Co. Ltd., Tokyo, Japan) used as the substrate was cleaned with 1 M of NaOH and subsequently washed with distilled water and acetone. The TiO_2 particles were positively charged in the IPA suspension. Then the stainless mesh was contacted with the cathode. The aluminum plate was used as an anode. The electrodes' sizes were 70 × 35 mm; the distance separating electrodes was 1.0 cm. During EPD, a constant voltage (195 V) was applied to electrodes using a standard DC power supply (GP0250-1; Takasago Ltd., Tokyo, Japan). The deposition time was 15 and 30 s. After EPD, drying was carried out at room temperature for 1 day. Samples' microstructures were observed using a scanning electron microscope (SEM: JSM-5310; JEOL, Tokyo, Japan).

2.4.2. Evaluation of attraction and photocatalytic decomposition

Attraction of 1,4-dioxane and EGDF to the TiO_2 coated electrode under voltage was evaluated using the following procedure. Reagent-grade 1,4-dioxane (Wako Pure Chemical Industries Ltd.) and EGDF (Frinton Laboratories Inc., Vineland, NJ, USA) were used in this study. Initial concentrations of stock solutions for adsorption experiments were 5.0, 10, and 50 ppm. A 30 s deposited sample was used as an electrode for this experiment. Before the attraction test, the TiO_2-coated mesh electrode was soaked in ion-exchanged water; then it was degassed in a glass chamber with an aspirator for 2 h to remove air from inside the TiO_2 porous coating. Platinum wire was used as a counter electrode to minimize the amount of materials adsorbed to the counter electrode surface. The distance separating the electrodes was 1.0 cm. These electrodes were soaked in the 150 ml of stock solution for 2 h without applying voltage. Then, concentrations of 1,4-dioxane and EGDF were measured and defined as C_0. Subsequently, voltage (0.4, 2.0, -0.4, and -2.0 V) was applied to the electrodes for 2 h in the dark and the solution concentration was evaluated. Concentration measurements were carried out using gas chromatography (GC-14A; Shimadzu Corp., Tokyo, Japan). That device was equipped with a flame ionization detector and a Sunpak-A column (Shimadzu Corp.). Nitrogen was used as the carrier gas; the respective temperatures for the detector, injection port, and column were 200, 180, and 180°C.

Concentrations of 1,4-dioxane stock solutions were fixed as 50 and 10 ppm for evaluation of photocatalytic decomposition. Before the experiment, the TiO_2 coated electrode was degassed in water in a vacuum chamber for 2 h. The distance between the TiO_2 coated mesh electrode and counter electrode was 1.0 cm. The electrodes were soaked into 1,4-dioxane stock solution (150 ml) and voltage (+0.4 and -0.4 V) was applied in the dark for 2 h. After evaluating the initial concentration (C_0), ultraviolet light (UV; 38 mW/cm^2 at TiO_2 coated mesh) was illuminated. Concentrations of organic compounds (1,4-dioxane and EGDF) were measured using gas chromatography. During this experiment, temperatures of the solution were within 20 ± 2°C. Photocatalysis by changing the applied voltage between +0.4 and -0.4 V every 5 min was also undertaken to investigate the voltage swing effect. The initial concentration of 1,4-dioxane stock solution was 10 ppm.

Decomposition was carried out with the automatic voltage switching circuit to investigate voltage swing effects in more detail. A schematic drawing displaying the settings for the decomposition experiment is presented in **Fig. 2-3**. A magnetic relay was connected to electrodes to change the direction of applied voltage rapidly. A PIC sequencer (TriState, Hokkaido, Japan) was used as a signal generator. The applied voltage was 0.4 V; the voltage direction was changed at regular time intervals (5 s, 30 s, and 300 s). Decomposition experiments without voltage swings were also carried out to obtain control samples. A 15 s deposited sample was used as the electrode for this experiment to clarify voltage effects. The stock solution concentration was 10 ppm. Other experimental conditions and the mode of pretreatment of TiO_2 stainless mesh before decomposition are the same as those for the destruction experiment described above.

2.5. Results and discussion

2.5.1. Decomposition rate dependence on applied voltage

Figure 2-4 depicts SEM micrographs of the TiO_2 coated mesh with deposition time of 30 s. A uniform coating was prepared using EPD. High magnification observation revealed that this coating is porous. The deposition weight of TiO_2 was 7.5 mg/ cm^2; the coating thickness was 24 μm after drying. **Figure 2-5** portrays the result of an attraction experiment by 5.0 ppm (C_0 value for 1,4-dioxane and EGDF) stock solution. During this experiment, TiO_2 particles were not detached from the stainless mesh, even under negative voltage. Between -2.0 and +2.0 V, the concentration of 1,4-dioxane decreased when negative voltage was applied to the TiO_2 coated mesh. Similar voltage-induced transport of 1,4-dioxane was reported also using electroosmosis [25]. In contrast, the concentration of EGDF decreased when positive voltage was applied to the TiO_2 coated mesh. These results imply that negative voltage is advantageous for 1,4-dioxane attraction, and vice versa for EGDF. A similar trend was obtained, but it was less remarkable using the 10 ppm stock solution. Moreover, it was difficult to obtain using the 50 ppm stock solution. This is probably attributable to the high concentration and resultant concentration change under applied voltage that was less than the detectable limit of this experiment.

Positive voltage is more effective for attracting EGDF to the TiO_2-coated electrode because EGDF has π-electrons in its C=O bonding. Although the reason why 1,4-dioxane preferably attracts on the electrode with negative voltage remains unclear; one plausible explanation is the transient OH group formation in 1,4-dioxane molecule [26, 27].

Gregory and McTigue measured the solvation potential in a 1,4-dioxane + water system and found that proton-dioxane solvation is favored with decreasing 1,4-dioxane concentration. Burrill and Johnson reported that, with a mass-analyzed threshold ionization spectrum, a 1,4-dioxane cation is produced using a smaller ionization potential than that used in a previous study. Detailed analysis of the origin of the voltage dependence of 1,4-dioxane in the current system remains as a subject for future work. The Schottky barrier exists between stainless steel and TiO_2. This voltage dependence is attributable mainly to the interaction between organic molecules and the stainless mesh surface.

Figures 2-6(a) and **2-6(b)** portray the concentration change of 1,4-dioxane and EGDF during UV illumination when the initial concentration was 50 ppm. The C_0 values for 1,4-dioxane were, respectively, 50.3 ppm (+0.4 V) and 48.2 ppm (-0.4 V). The initial concentration of EGDF (C_0) in **Fig. 2-6** was set as that of 1,4-dioxane in this experimental condition, as in a previous study [23]. Once the concentration of 1,4-dioxane decreases, that of EGDF increases. Although applied voltage effects on the photocatalysis of EGDF and 1,4-dioxane are discernible, they are very slight. A nonlinear relation was found between the reaction time and 1,4-dioxane concentration, however, a linear relation was obtained between reaction time and $\ln[(1,4\text{-dioxane})/(1,4\text{-dioxane})_0]$ (where $(1,4\text{-dioxane})_0$ is the initial concentration of 1,4-dioxane in water). From this result, this photocatalytic decomposition is inferred to be governed by diffusion of 1,4-dioxane [28].

The voltage effect became large (**Figs. 2-6(c)** and **2-6(d)**) when the solution concentration was 10 ppm. The C_0 values for 1,4-dioxane were, respectively, 9.5 ppm (+0.4 V) and 9.9 ppm (-0.4 V). The decomposition rate of 1,4-dioxane under -0.4 V was higher than that under +0.4 V. The EGDF was not detected in the case of +0.4 V. The

EGDF concentration increased rapidly when -0.4 V was applied to the TiO_2 coated electrode. Negative voltage was better for photocatalytic decomposition of 1,4-dioxane, and worse for that of EGDF. The decomposition rate of 1,4-dioxane, as obtained by assuming a first-order reaction (diffusion-limited reaction) on **Fig. 2-6**(c), was 2.2×10^{-4} s^{-1} ($R^2 = 0.98$) under -0.4 V, and 5.3×10^{-5} s^{-1} ($R^2 = 0.92$) under +0.4 V. This trend is consistent with the voltage dependence of attraction of 1,4-dioxane and FGDF. Because of the Schottky barrier, this result is attributable not to the improvement of charge separation in TiO_2, but to the enhancement of attraction. Results of the decomposition experiment revealed that applying voltage was more effective at 10 ppm, although both decompositions at 10–50 ppm are in a diffusion-limited condition. In the 10 ppm case, substances for decomposition are not so abundant near the TiO_2 surface as they are for the 50 ppm case. Therefore, the attraction effect by application of voltage can be said to be more remarkable at 10 ppm than at 50 ppm. Under a voltage swing condition, the concentration of 1,4-dioxane decreased rapidly and the amounts of EGDF were much less than those for -0.4 V (**Figs. 2-6(c)** and **2-6(d)**). This result implies that the voltage swing is effective for decomposition of both 1,4-dioxane and EGDF. The decomposition rate of 1,4-dioxane under -0.4 V was almost identical to that under voltage swing. A plausible explanation for this result is depicted in **Fig. 2-7**. Applying negative voltage induces a flux of 1,4-dioxane to the TiO_2 coated mesh. In the flux, some 1,4-dioxane molecules are decomposed to EGDF on the TiO_2 surface. However, some 1,4-dioxane molecules will be transported into the pore structure of the TiO_2 coating and condensed on the surface of the stainless steel mesh (**Fig. 2-7(a)**). Once voltage is switched to positive from this state, a reverse flux of 1,4-dioxane is generated. Then, 1,4-dioxane in the pore channel of the TiO_2 coating is transported to the TiO_2 coating surface and decomposed into EGDF.

Furthermore, the generated EGDF molecules move into the pore channel and increase its concentration (**Fig. 2-7(b)**). The voltage swing circulates water in the pore channel in the coating and increases the rate of photocatalysis of 1,4-dioxane in water. An important requirement for effectiveness of the voltage swing is a diffusion-limited reaction. However, we think this is merely one requirement. The reaction place and attraction site are proximate, but located in different sites in this system. This is also one reason why the voltage swing process was effective. Moreover, the effectiveness of the voltage swing process depends on a coating structure such as the pore size, porosity, and tortuosity of the pore channel. Assuming a tortuosity factor of 4 [29], the practical diffusion lengths of chemicals are calculable as around 100 μm (4 × 24 μm (coating thickness)). Nevertheless, both the actual degree of the electric field on the chemicals in the pore channel and interaction between chemicals and the TiO_2 pore channel surface remain unclear. This value has almost identical order of the typical diffusion distance of substances in water for 5 min (assumption: diffusion constant $D = 10^{-9}$ m^2/s, $(DT)^{1/2} \approx 500$ μm), which is the voltage swing interval. For that reason, the swing interval might also be an important process parameter for acceleration of photocatalysis by the voltage swing.

2.5.2. Effect of the voltage swing interval

For the swing interval change experiment, we used TiO_2-coated mesh with 15 s deposition time. The deposition weight was 2.69 mg/cm^2, based on the entire mesh area including holes. The layer thickness, as determined by direct observation using SEM, was 6.5 μm after drying. The relative density of the coating was calculated as ca. 52%, which is almost equal to that for a powder compacted by uniaxial pressing. The average pore size was calculated as 150 nm if we assume that perpendicular cylindrical pores form a hexagonal structure and that the distance between pores is 200 nm (particle diameter) in a 2D plane surface on the coating [30]. Assuming a typical tortuosity factor of four for a pressed powder compact [29], the average pore size was calculated as 75 nm. **Figure 2-4** shows that these values are of almost equal order.

The changes in 1,4-dioxane and EGDF concentration during UV illumination under applied voltage are presented in **Fig. 2-8**. The concentration of 1,4-dioxane decreased and that of EGDF increased with the decreasing voltage swing interval. This concentration order is reasonable because EGDF is formed by photocatalysis of 1,4-dioxane, as presented in **Fig. 2-2**. However, the interval changed the EGDF concentration to a greater degree than that of 1,4-dioxane. In the case of 1,4-dioxane, the highest decreasing rate was attained under constant voltage (-0.4 V). The voltage swing decreased the rate, although its degree is small. However, the EGDF concentrations attained at 5 s and 30 s intervals were higher than those attained under constant voltage (-0.4 V). We have repeated these experiments several times and confirmed the repeatability of these trends.

The concentration change of 1,4-dioxane under voltage swings suggests that concentration of 1,4-dioxane in the reverse flux through the TiO_2 coating surface is less than that of bulk solution. Plausible explanations for the gradual increase of the concentration of 1,4-dioxane with increasing voltage swing interval are the following. 1) Increasing concentration of 1,4-dioxane in the reverse flux attributable to the increased condensation of 1,4-dioxane in the pore channel of the TiO_2 coating by the increasing swing interval. 2) Decreasing flux of 1,4-dioxane to TiO_2 surface from bulk solution under negative voltage because of the large opposite flux of EGDF from pore channel, which is highly condensed by increasing the swing interval.

The respective molecule lengths of 1,4-dioxane and EGDF were calculated using chemical software (Chem 3D Ultra 9.0; Cambridgesoft Corp.) as 0.48 nm and 0.55 nm. However, the value of EGDF reflects hydrogen bonding in the molecule. Water is a good solvent for EGDF. Therefore, its structure will be stretched and thereby be elongated in water. Moreover, an EGDF molecule possesses two C=O bonds with high π-electron density. Consequently, it becomes a Lewis base [23] and attracts a certain number of water molecules by virtue of its dipole moment. However, a 1,4-dioxane molecule does not possess such bonds in its structure; the origin of its voltage dependence might be transient OH group formation. Therefore, it is expected that EGDF forms a larger hydrated molecule than 1,4-dioxane in water, and that EGDF exhibits a smaller diffusion constant in water than 1,4-dioxane. High EGDF concentrations under a small voltage swing interval are probably attributable to the difference of the diffusion constant. Under constant negative voltage, EGDF is generated by the flux of 1,4-dioxane from bulk solution to the TiO_2 coating surface. A certain amount of 1,4-dioxane molecules will also intrude into the TiO_2 coating layer and condense during this period. For short intervals such as 5 s or 30 s during positive voltage, condensed 1,4-dioxane molecules in the pore structure are supplied to the TiO_2 surface and decomposed into EGDF. When the diffusion constant of EGDF is small, the EGDF molecules generated on the coating surface cannot intrude to the pore structure of the TiO_2 coating layer under a short voltage swing interval. Therefore, the concentration of EGDF in the bulk solution becomes higher than the constant negative voltage. Once the interval is increased to 300 s, the EGDF transport (intrusion) into the pore structure is attained. The reaction place and attraction site will, ideally, be located in different sites in this system when the swing interval is 300 s. Efficient photocatalysis of 1,4-dioxane was attained with suppression of EGDF formation. **Figure 2-9** portrays the proposed mechanism with a short swing interval; **Fig. 2-10** is circulation model of EGDF under constant voltage. The concentration changes of 1,4-dioxane and EGDF in bulk solution include the net decomposition amount at the TiO_2 coating surface and the condensation amount in the coating's pore channel. Therefore, the apparent material balance between the decrease of 1,4-dioxane and increase of EGDF is expected to differ from that of the case of the voltage swing.

Assuming a tortuosity factor of 4 [29] and a diffusion distance of EGDF of around 26 μm (4 × 6.5 μm (coating thickness) at 300 s, the apparent order of the diffusion constant is calculable as 10^{-12} m^2/s (assuming that the diffusion distance = $(DT)^{1/2}$). This value is much smaller than the normal order (10^{-9} m^2/s) of the diffusion constant for chemical species in liquid. Although both the actual degree of electric field on EGDF in the pore channel and the interaction between EGDF and TiO_2 pore channel surfaces remain unclear, a plausible explanation for this discrepancy is the existence of opposite flow by 1,4-dioxane.

Results of this study demonstrate that the swing interval is also an important process parameter for acceleration of photocatalysis using the voltage swing method. A long interval was effective for EGDF decomposition, probably because of the small diffusion constant of EGDF molecules in water. Quantitative investigation of the relation between diffusion coefficients of 1,4-dioxane or EGDF in water and pore structure such as pore size and length of connected pores will be addressed in future studies. The diffusion distance depends not only on practical operation conditions such as the voltage swing interval, but also on the material structure: the coating thickness, pore size, pore amount, and tortuosity factor. For effective EGDF decomposition, proper material design and optimization of operation conditions are necessary.

2.6. Conclusion

The current chapter presented a demonstration showing that the photocatalytic decomposition rate of 1,4-dioxane depends on application of voltage under a thin concentration condition, which diffuses the limited reaction. In that reaction, 1,4-dioxane and ethylene glycol diformate (EGDF), a main intermediate of the photocatalysis of 1,4-dioxane, exhibited inverse voltage dependence. The voltage swing provides high-efficiency photocatalysis of 1,4-dioxane while suppressing EGDF formation. The 1,4-dioxane concentration decreased with the decrease of the voltage swing interval, but the change was small. In contrast, the EGDF concentration was changed remarkably by changing the interval. Moreover, the EGDF concentration increased with the decreasing interval. These results suggest that the diffusion constant of EGDF molecules in the pore structure differs from that of 1,4-dioxane, and that the response to the voltage swing interval depends on the chemical species. For effective water purification using this system, proper material design and optimization of operation conditions are necessary.

References

[1] Ishikawa, S.; Kuriyano, N.; Ikuta, H. *Hikarishokubai*, **15**, 224-225 (2004) in Japanese.

[2] Risk-Assessment Report Vol. 21 on: 1,4-Dioxane, CAS no. 123-91-1, EINECS no. 204-661-8. (European Chemicals Bureau, Joint Research Centre, European Community, 2004).

[3] Abe, A. *Sci. Total Environ.*, **227**, 41-47 (1999).

[4] Zenker, J.; Borden, R. C.; Barlaz, M. A. *J. Environ. Eng. Sci.*, **20**(5), 423-432 (2003).

[5] Simazaki, D.; Asami, M.; Nishimura, T.; Kunikane, S.; Aizawa, T.; Magara, Y. *Water Sci. Tech.; Water Supply*, **6(**2), 47-53 (2006).

[6] IARC, International Agency for Research on Cancer Monographs on the Evaluation of Carcinogenic Risk of Chemicals to Man, **71**, 589-602 (1999).

[7] Klecka, G. M.; Gonsior S. J. *J. Hazard Mater.*, **13**, 161-168 (1986).

[8] Gehringer, P.; Matschiner, H. *Water Sci. Tech.*, **37**, 195-201 (1998).

[9] Beckett, M. A.; Hua, I. *Environ. Sci. Tech.*, **34**, 3944-3953 (2000).

[10] Sarkar, P.; Nicholson, P. S. *J. Am. Ceram. Soc.*, **79(**8), 1987-2002 (1996).

[11] Corni, I.; Ryan, M. P.; Boccaccini, A. R. *J. Eur. Ceram. Soc.*, **28**, 1353-1367 (2009).

[12] Sunada, K.; Watanabe, T.; Hashimoto, K. *J. Photochem. Photobiol. A: Chem.*, **156**, 227-233 (2003).

[13] Matthews, D.; Kay, A.; Gratzel, M. *Aust. J. Chem.*, **47**, 1869-1877 (1994).

[14] Tabellion, J.; Clasen, R. *J. Mater. Sci.*, **39**, 803-811 (2004).

[15] Boccaccini, A.R.; Schindler, U.; Krüger, H.-G. *Mater. Lett.*, **51**, 225-230 (2001).

[16] Yum, J.-H.; Kim, S.-S.; Kim, D.-Y.; Sung, Y.-E. *J. Photochem. Photobiol. A: Chem.*,

73, 1-6 (2005).

[17] Yanagida, S.; Nakajima, A.; Kameshima, Y.; Okada, K.; Yoshida, N.; Watanabe, T. *Mater. Res. Bull.*, **40**, 1335-1344 (2005).

[18] Yanagida, S., Preparation of crack-free titania coating on metal mesh by electrophoretic deposition and photocatalytic decomposition of 1,4-dioxane in aqueous system, *Master's thesis* (2005).

[19] Maurino, V.; Calza, P.; Minero, C.; Pelizetti, E.; Vincenti, M. *Chemosphere*, **35**, 2675-2688 (1997).

[20] Hill, R. R.; Jeffs, G. E.; Roberts, D. R. *J. Photochem. Photobiol. A: Chem.*, **108**, 55-58 (1997).

[21] Nakajima, A.; Matsui, S.; Yanagida, S.; Kameshima, Y.; Okada, K. *Surf. Coatings Tech.*, **203**(9), 1133-1137 (2009).

[22] Coleman, H. M.;Vimonses, V.; Leslie, G.; Amal, R. *J. Hazardous Mater.*, **146**, 496-501 (2007).

[23] Nakajima, A.; Tanaka, M.; Kameshima, Y.; Okada, K. *J. of Photochem. Photobiol. A: Chem.*, **167**, 75-79 (2004).

[24] Nakajima, A.; Sasaki, H.; Kameshima, Y.; Okada, K.; Harada, H. *Ultrasonics Sonochemistry*, **14**, 197-200 (2007).

[25] Jain, A. K.; Srivastava, R. K. *J. Membrane Sci.*, **112**, 41-46 (1996)

[26] Gregory, R.E.; McTigue, P. T. *J. Electroanal. Chem.*, **387**, 65-70 (1995).

[27] Burril, A. B.; Johnson, P. M. *Chem. Phys. Lett.*, **350**, 473-478 (2001).

[28] Hashimoto, K.; Fujishima, A. (Eds.). *TiO_2 Photocatalysis; its Application to Self-cleaning, Anti-bacterial and Air Purifying Materials*, CMC Press, Tokyo, 1998, pp. 169-175, in Japanese.

[29] Nakajima, A.; Messing, G. L. *J. Am. Ceram. Soc.*, **81**, 1163-1172 (1998).

[30] Wang, Z-S.; Sasaki, T.; Muramatsu, M.; Ebina, Y.; Tanaka, T.; Wang, L.; Watanabe, M.; *Chem. Mater.*, **15**, 807-812 (2003).

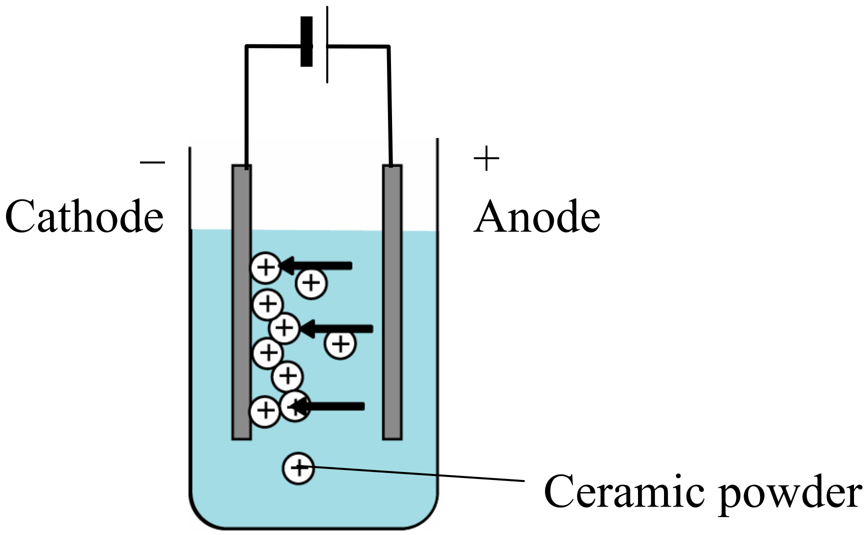

Figure 2-1. Schematic illustration of the EPD process.

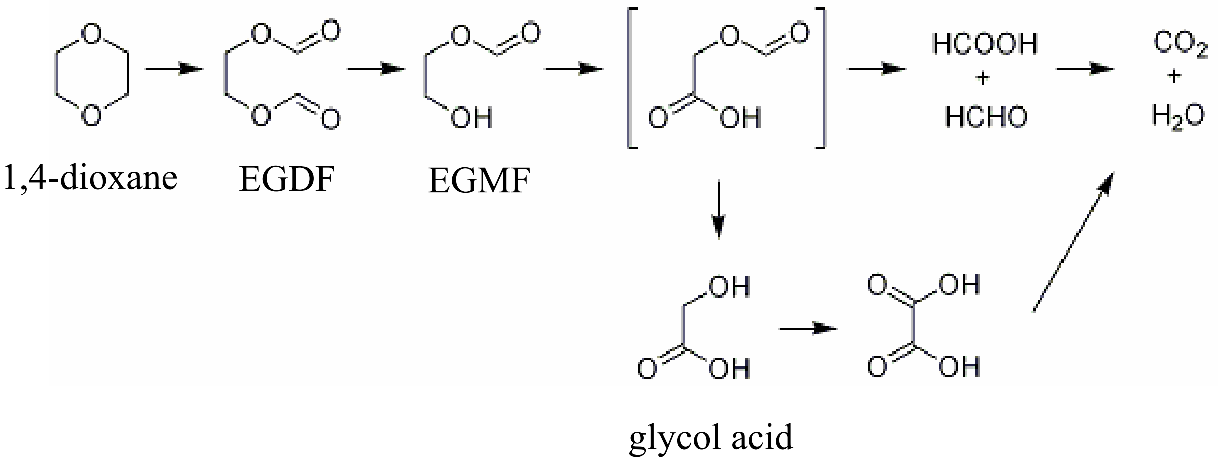

Figure 2-2. Photocatalytic decomposition pathway of 1,4-dioxane in water [19].

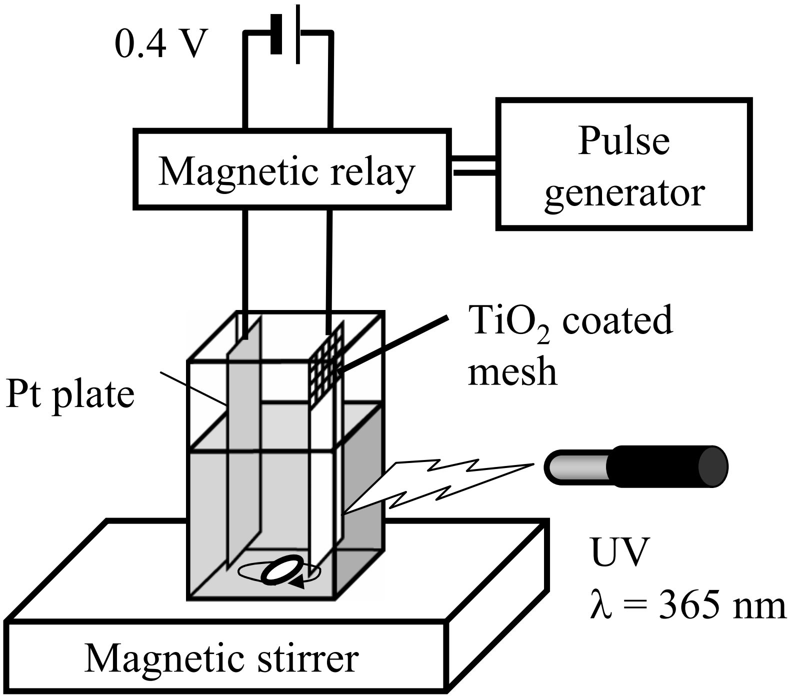

Figure 2-3. Schematic illustration of the setting for the decomposition experiment under voltage swing.

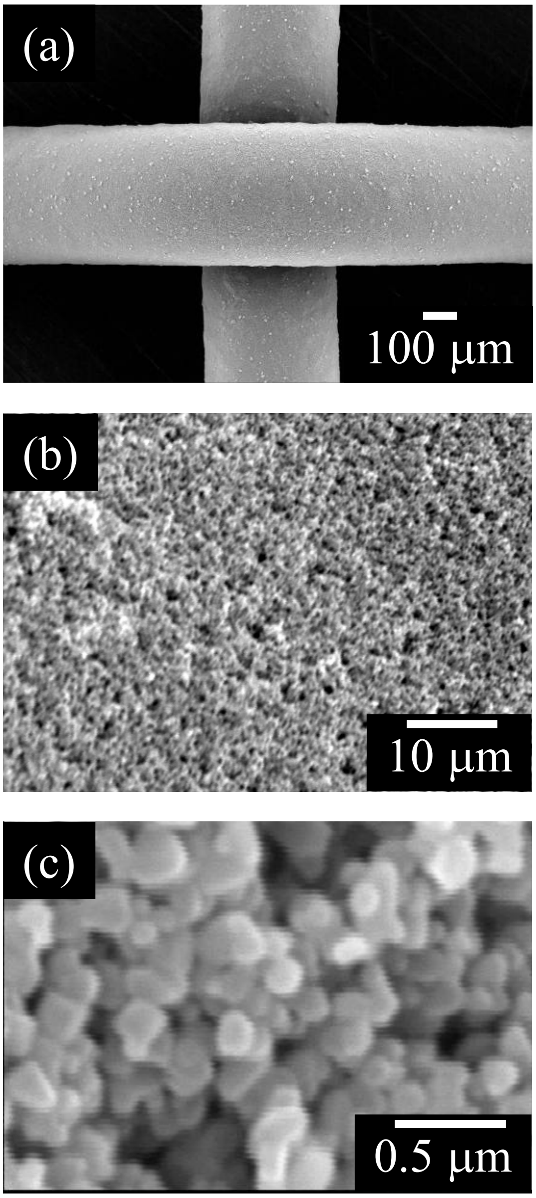

Figure 2-4. SEM micrographs of TiO_2-coated stainless mesh.

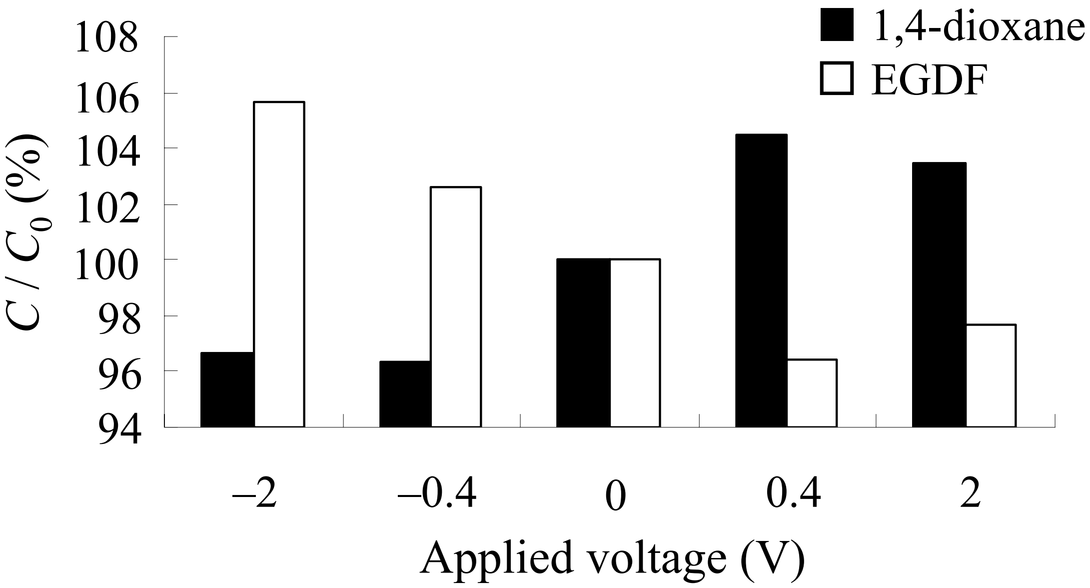

Figure 2-5. Concentration change of 5.0 ppm stock solution to which voltage was applied.

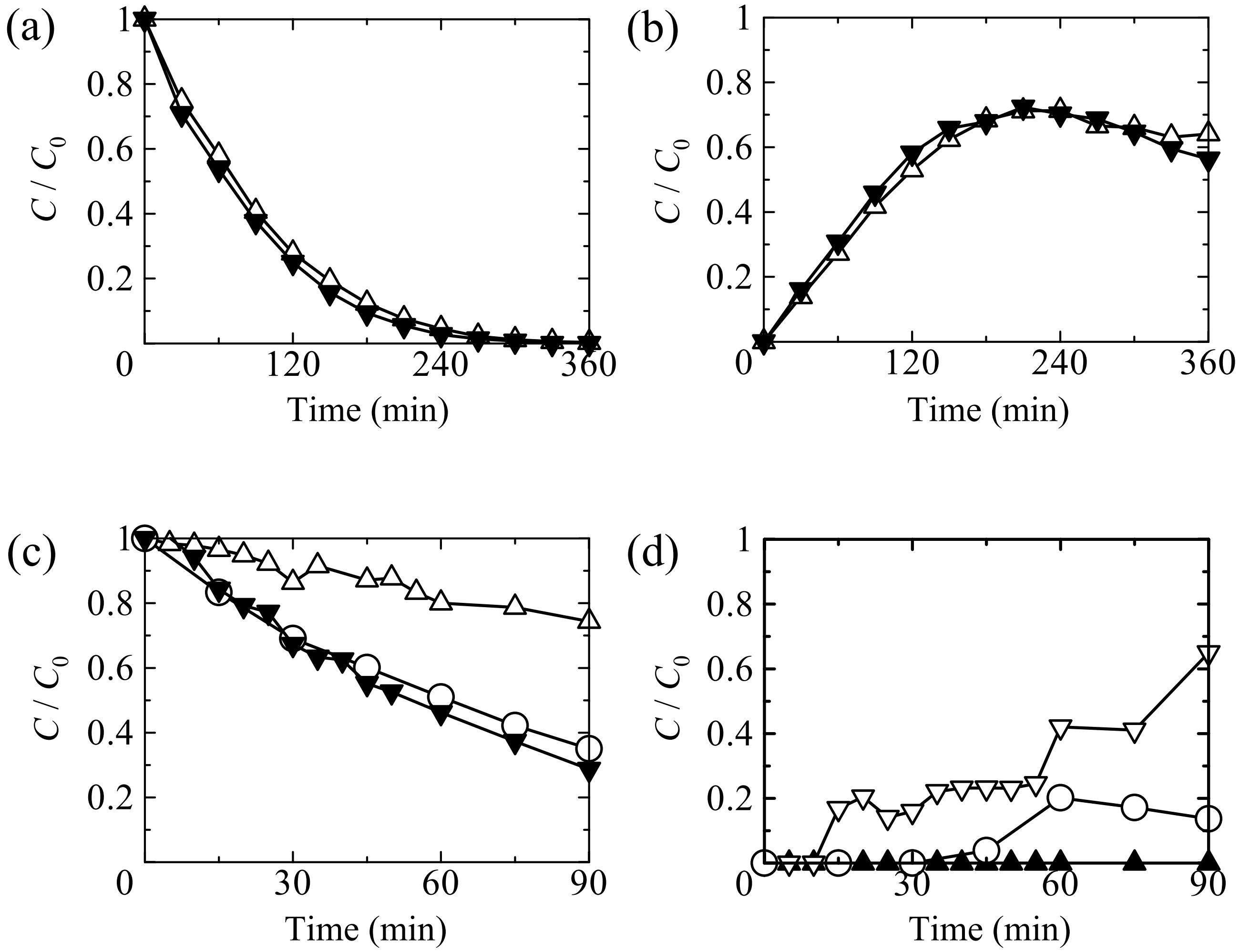

Figure 2-6. Concentration changes of 1,4-dioxane and FGDF during UV illumination under +0.4 V (△), -0.4 V (▼), and bias swing (○): (a) 1,4-dioxane in 50 ppm stock solution, (b) EGDF in 50 ppm stock solution, (c) 1,4-dioxane in 10 ppm stock solution, and (d) EGDF in 10 ppm stock solution.

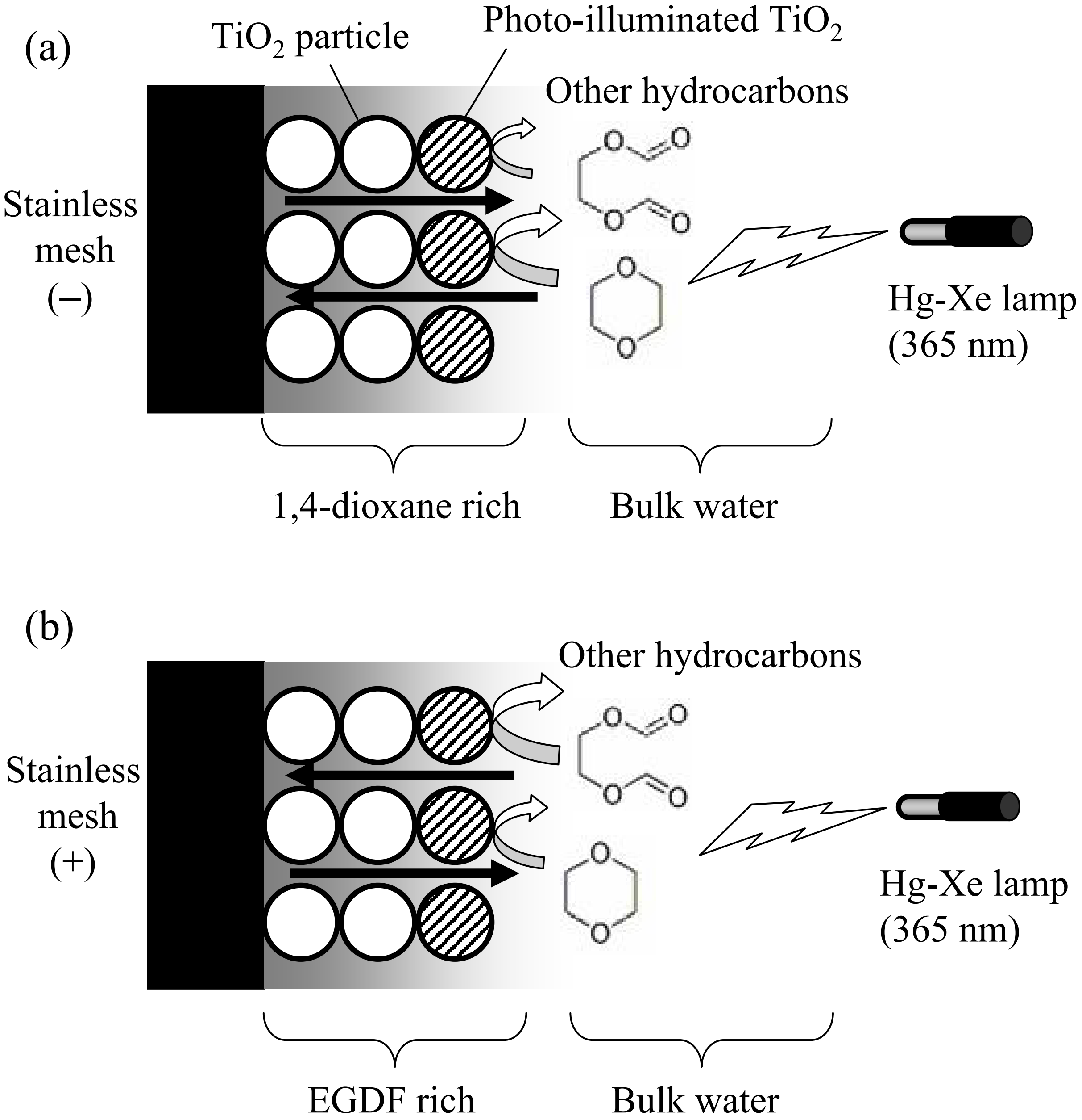

Figure 2-7. Schematic illustration of the proposed mechanism of the 5 min voltage swing effect: (a) -0.4 V; and (b) +0.4 V.

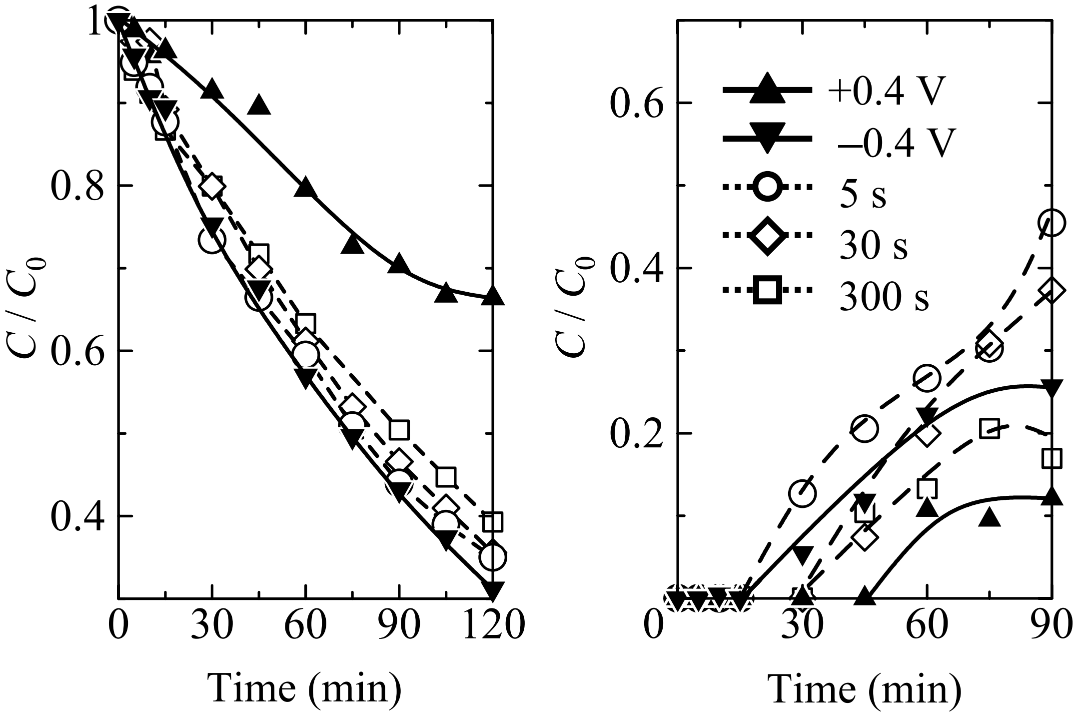

Figure 2-8. Concentration change during UV illumination (38 mW/cm^2) under constant and bipolar voltage: (a) 1,4-dioxane in a 10 ppm stock solution, and (b) EGDF in a 10 ppm stock solution.

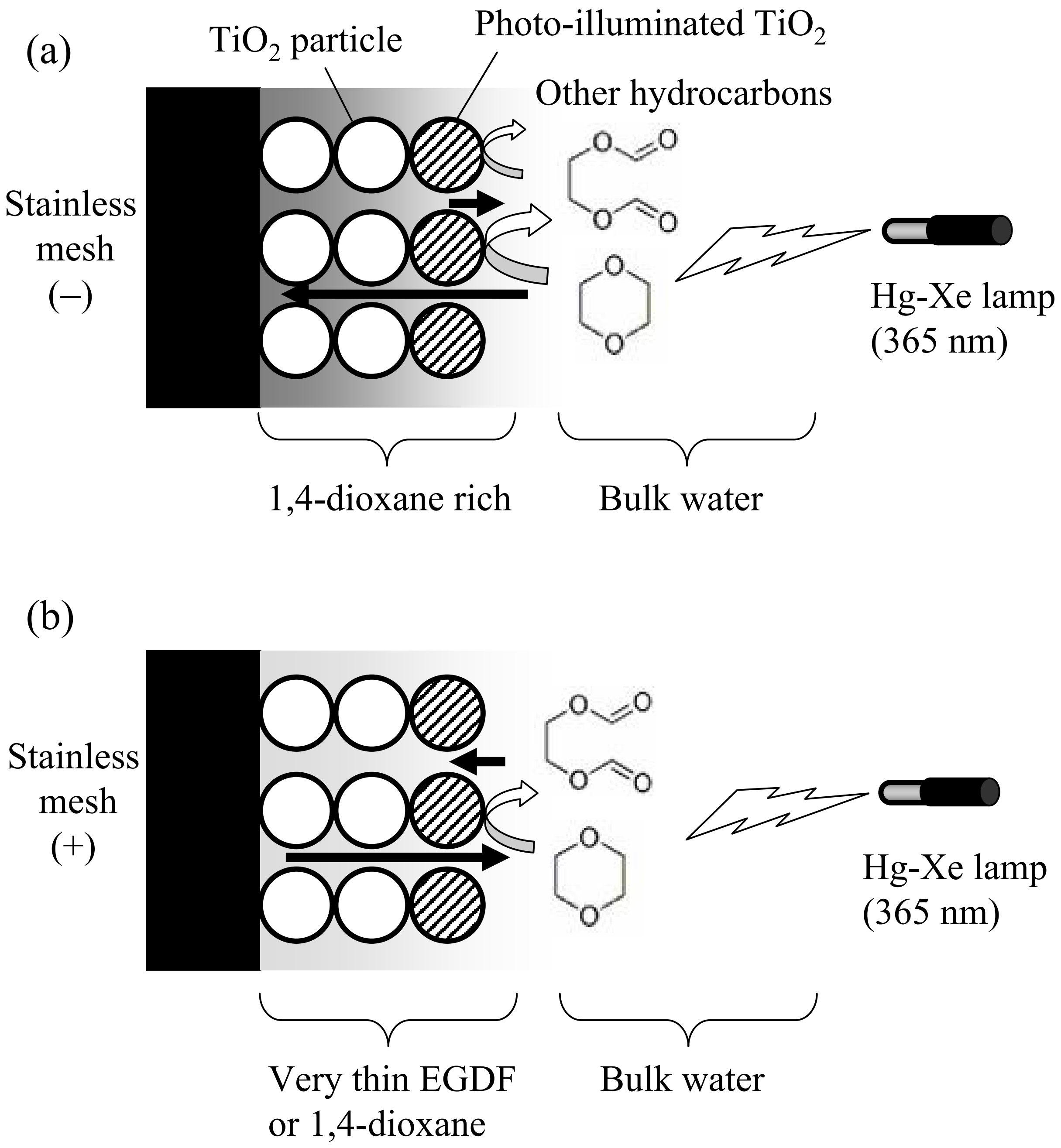

Figure 2-9. Schematic illustration of the difference of material transport under short voltage swing intervals such as 5 s and 30 s: (a) -0.4 V and (b) +0.4 V.

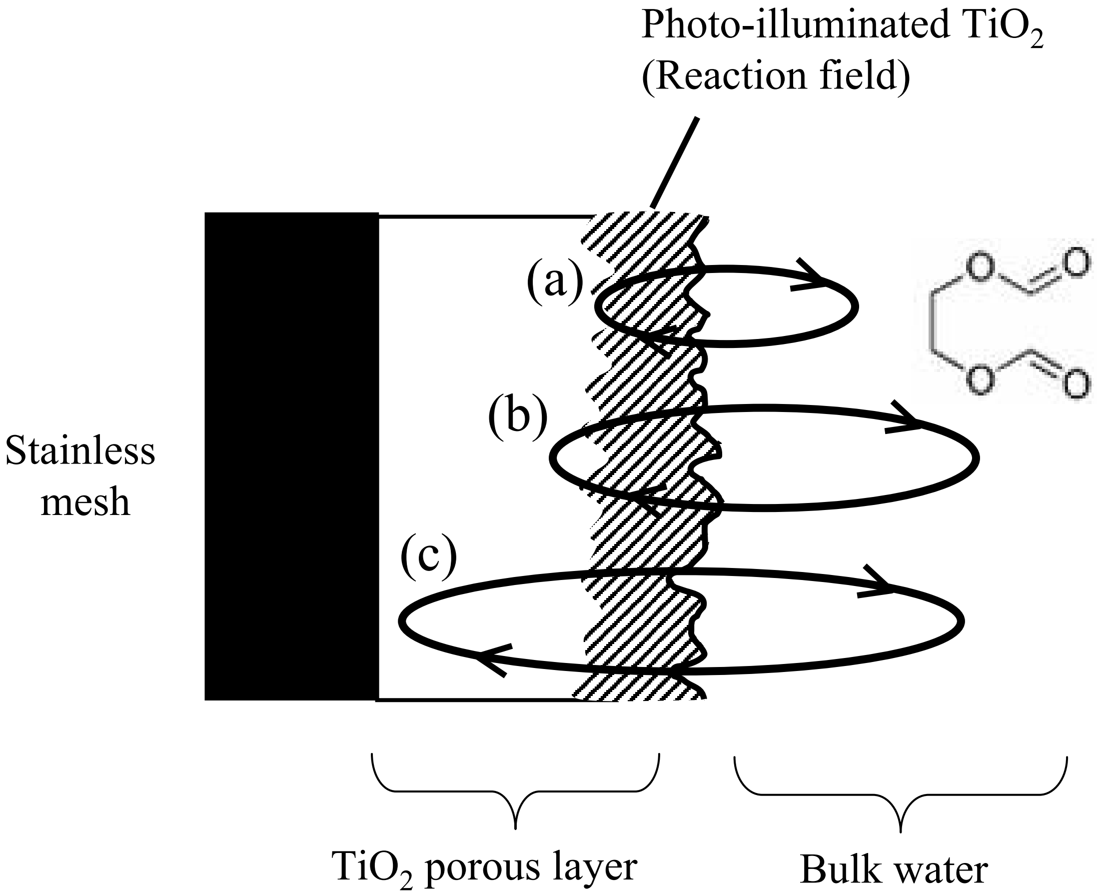

Figure 2-10. Schematic illustration of EGDF transport under different voltage swing intervals: (a) 5 s, (b) 30 s, and (c) 300 s.

CHAPTER 3

Preparation of Heteropolyacid-intercalated Layered Double Hydroxide

3.1. Introduction

3.1.1. Heteropolyacid

3.1.1.1. Composition and structure

Heteropolyacids (HPAs) are a series of inorganic clusters: they are polymeric oxoanions consisting of oxoanions of two or more kinds. Their general formula is presented as $[X_xM_mO_p]^{n-}$. (M = W, Mo, V, Nb, Cr, and Ta), where x is a so-called heteroatom. Polyanions consisting of one kind of oxoanion are called isopolyacids (IPAs). Their general formula is presented as $[M_mO_p]^{n-}$. Various HPAs and IPAs have been synthesized. Typical HPA structures are depicted in **Fig. 3-1**. Their properties depend on M, X, the counterion and the structure. They are soluble in water and organic solvent and are stable under an appropriate pH range. However, under high pH, hydrolysis occurs and they are decomposed to smaller species. Recently, supramolecular polyacids (3–5 nm) were synthesized as functional materials of different forms: rings, capcel tubes, and chains [1].

3.1.1.2. Catalytic property of HPAs

The HPAs and IPAs are known as acid catalysts. Especially, Keggin-type HPAs ($H_n[XM_{12}O_{40}]^n$, hereinafter abbreviated as XM_{12}) are well investigated and applied within the chemical industry because of their strong Brønsted acidity, oxidation power, and thermal stability. Okuhara et al. reported acid strength measured using ammonia TPD method [2].

$PW_{12} > SiW_{12} > PMo_{12} > SiW_{12}$

These HPAs are used as catalysts for epoxidation, hydration, asymmetric syntheses, oxidation, and polymerization [3, 4].

A notable characteristic of Keggin-type solid HPAs (Na salt, and hydrogen-form Keggin anions) is their absorption of large amounts of some polar molecules. Some alcohols, ketones, and amines are absorbed and diffused into this type of solid HPA [5]. Results of both IR and NMR studies indicated formation of onium ions such as $CH_3OH_2^+$ for methanol, and $C_2H_5OH_2^+$ and $(C_2H_5OH)_2H^+$ for ethanol in solid HPA [6]. These molecules coordinate with HPA anion and form a stoichiometric complex. They swell HPAs under high partial pressure [7]. Therefore, in some cases, catalytic reactions occur not only on the surface, but also inside of Keggin-type solid HPAs. The resultant so-called bulk-type reaction in the "pseudo-liquid phase HPA" differs from a surface reaction [8]. In that condition, the HPA provides a liquid-like reaction field. Currently, supported XM_{12} and insoluble HPA salt $Cs_{2.5}H_{0.5}PW_{12}O_{40}$ were investigated and used as solid acid catalysts in a liquid-solid heterogeneous reaction [9].

3.1.1.3. Photocatalytic property and photochromism

Keggin-type HPAs are also known as photocatalysts [10, 11]. Electrons are promoted from an orbital of oxygen to that of a metal atom (such as from O2p to W3d) when UV is illuminated to Keggin-type HPAs. This oxygen-to-metal charge transfer engenders electron charge separation. In the photocatalytic reaction, generated holes oxidize organic molecules [12]; then HPAs are reduced and the electron is delocalized by the slight energy (E_{th}). The reduced HPAs absorb visible light of restricted energy (E_{op}) because this absorption is attributable to its d-d transition or IV transition [13]. Evaluated E_{th} and

E_{op} values are shown in **Table 3-1**. Because of visible absorbance, reduced HPAs have a distinctive color called heteropolyblue.

A redox circle is depicted in **Fig. 3-2**. Reduced HPA is reoxidized by dioxigen and returns to the initial state [14, 15]. Generally, excited state Keggin-type tungstates and molybdates have sufficient oxidation potential for organic compound oxidation (PW_{12}, 3.7 V [11]; PMo_{12}, 2.8 V vs. NHE [16]). Some HPAs possess higher oxidation potential than TiO_2 (2.7 V vs. NHE [17]). However, the photocatalytic reaction of molybdates is very slow; reduced molybdates are only slightly reoxidized by O_2. Because of fast reoxidation, tungstates act as a more effective photocatalyst than molybdates [15]. Recently, HPA photocatalysts have come to be used for water purification. Papaconstantinou et al. investigated photodecomposition of organic compounds (including aromatic carbon) in aqueous media. During the photocatalytic degradation process, organic compounds are decomposed directly and indirectly through ·OH radicals [18].

3.1.2. Layered double hydroxide

Layered double hydroxides (LDH) are described as $M^{2+}_{1-x}M^{3+}_{x}(OH)_2A^{n-}_{x/n}\cdot mH_2O$; they comprise octahedral $M^{2+}(OH)_6$ brucite-like layers and changeable interlayer anion. **Figure 3-3** shows the two-dimensional layer structure of LDHs. The positive layer charge is controllable by changing the ratio of divalent and trivalent cations [19]. Ion-exchange method [20–22] and reconstruction method [23–25] are known as typical anion intercalation methods. Ion-exchange method is executed by merely soaking LDHs in an anion solution; reconstruction method involves heating LDHs at 500–600°C before soaking in an anion solution. The layered structure decomposes when LDHs are heated to

500–600°C. However, the layer structure is reconstructed by soaking it in water with a proper anion. The reconstruction process is used for large anion intercalation into LDH. Various LDH hybrids were prepared using these processes: organic molecules [26, 27], polymers, metal complexes [28] and oxometallate-LDH hybrid materials [28] have been reported.

3.1.3. HPA-LDH hybrid

Actually, HPAs have good solubility in water and are used as homogeneous catalysts in liquid phase reactions. However, immobilization is necessary for easy separation and catalyst recycling. To date, various polyacid and heteropolyacid anion intercalated LDHs have been prepared for this purpose [29]. Intercalation of anions into LDHs requires a proper balance of the charge amount and size. Hu et al. prepared a composite using W-based HPA and LDH with lacunary Keggin anion $[SiW_{11}O_{39}]^{8-}$ and Zn-Al (NO_3) LDH [30]. However, Keggin-type anions such as $[PW_{12}O_{40}]^{3-}$ and $[SiW_{12}O_{40}]^{4-}$ are difficult to intercalate into the LDH layer because of their extremely lower negative charge density and lower stability in high-pH water than those of lacunary Keggin-type anions. In water with high pH, Keggin-type anions are commonly decomposed into lacunary Keggin ions by hydration [31]. However, the intercalation-process-dependence of the stability of W-based Keggin-type anions is not well reported. In a previous study, the HPA-LDH composite was investigated as a thermal catalyst. Nevertheless, its photocatalytic activity has not been reported. For this study, we prepared LDHs of the Mg-Al(CO_3) system and Zn-Al(NO_3) system. The Mg-Al system is more basic and more easily dissolves in an acid solution. However, it has better reconstruction ability than Zn-Al [28]. Therefore, we prepared HPA-LDH composites using ion-exchange method on Zn-Al(NO_3) LDH and

Reconstruction method on Mg-Al(CO_3) LDH. A Keggin-type heteropolyacid $H_4SiW_{12}O_{40}$ (SiW_{12}) was used for this study. Then, the effects of intercalation process on the composite characteristics and stability of the Keggin structure were investigated. The HPA-LDH photocatalytic activity in 2-propanol gaseous decomposition was evaluated and discussed.

3.2. Experimental procedure

3.2.1. LDH synthesis

All starting chemicals were of reagent grade (Wako Pure Chemical Industries Ltd., Tokyo, Japan). In this study, LDHs of the Mg-Al(CO_3) system (Mg/Al=2, 4) and Zn-Al(NO_3) system (Zn/Al=2) were prepared as in previous studies [32, 33]. **Figure 3-4** shows the experimental procedure of Mg-Al(CO_3) LDH preparation. Solutions of $Mg(NO_3)_2{\cdot}6H_2O$ and $Al(NO_3)_3{\cdot}\ 9H_2O$ were mixed in the appropriate ratio and co-precipitated by adding mixed solutions of NaOH and $Na_2(CO_3)$. After mixing (24 h), centrifuging, washing in distilled water and ethanol, and drying, LDH powders of the Mg-Al(CO_3) system were obtained. Hereinafter, Mg/Al = 2 and Mg/Al = 4 systems are abbreviated respectively as Mg_2Al and Mg_4Al.

Figure 3-5 portrays experimental procedures of the Zn-Al(NO_3) LDH preparation. Solutions of $Zn(NO_3)_2{\cdot}\ 6H_2O$ and $Al(NO_3)_3{\cdot}\ 9H_2O$ were mixed in the appropriate ratio and co-precipitated by adding mixed solutions of NaOH at pH 9.5. In this process, distilled water was used after degassing by N_2 bubbling. After refluxing in N_2 at 90°C for 18 h, centrifuging, washing in distilled water, and drying, LDH powder of the Zn-Al(NO_3) system was obtained.

3.2.2. Ion-change method

Ion-exchange processing and reconstruction processing were carried out using ion changed water to avoid CO_3^{2-} effects. Interlayer NO_3^- in LDH powder of the Zn-Al(NO_3) system is exchanged with HPAs in a high-temperature aqueous solution [29, 34]. **Figure 3-6** shows a flow diagram of ion-change method. In this work, ethylene glycol (EG) was used as a swelling agent. An aqueous solution of EG (H_2O:EG=1:1) was used to support interlayer space expansion. Subsequently, $SiW_{12}O_{40}\cdot 26H_2O$ (0.20 g) was dissolved into EG solution (40 cm^3) and LDH (0.40 g) was added to the solution. The mixture was stirred at 80°C for 2 h, then centrifuged at 8000 rpm for 20 min after cooling and washing with water. White powder was obtained after drying at 80°C for 24 h. For comparison, the same procedure was carried out using water only, instead of the EG solution.

3.2.3. Reconstruction method

Figure 3-7 shows a flow diagram of the reconstruction method. The LDHs of Mg-Al(CO_3) system were calcined at 500°C for 12 h in air. Heat-decomposed LDHs were prepared. Then $SiW_{12}O_{40}\cdot 26H_2O$ (0.68 g) was dissolved into water (200 cm^3); the heat-decomposed LDHs (0.20 g) were added to the solution. After stirring for 24 h, LDH powders were separated from the solution by centrifugation (8000 rpm, 20 min) and washed with water. White powder was obtained after drying at 80°C for 24 h.

3.2.4. Characterization

Crystalline phases of the obtained powders were evaluated using X-ray diffraction (XRD, XRD-6100; Shimadzu Corp.). The specific surface area and pore structure were evaluated using N_2 adsorption and desorption isotherms at 77 K (Autosorb-1;

Quantachrome Instruments). The specific surface area was calculated using BET method and the pore volume was obtained from the maximum amount of adsorption at a relative pressure *(P/P_0)* of 0.999. The pore size distribution was calculated with desorption isotherms using BJH method. The average pore size was calculated from the specific surface area and pore volume. The chemical compositions of the LDHs were analyzed for Mg, Al, and W using ICP-OES (Teledyne – Leeman Labs, USA). The infrared spectra (FT-IR 8600PC; Shimadzu Corp.) of the samples were recorded using the KBr disk method.

Photocatalytic activity was evaluated according to the decomposition of gaseous 2-propanol (Wako Pure Chemical Industries Ltd.). The HPA-LDH composite prepared by ion change method with EG solution was used in this experiment. Before the experiment, the 100 mg powder sample was exposed to UV light (1 mW/cm^2, 365 nm) for 1 day to remove organic compounds adsorbed onto the surface. **Figure 3-8** presents settings for this measurement. A Pyrex glass vessel (500 ml in volume) with a quartz glass lid was used as a batch reactor. Sample powder was set in a Petri dish at the center of the vessel. Subsequently, the vessel was sealed and 2-propanol gas was injected into it. The injected gas amount was equivalent to that for 100 ppm concentration. The vessel was then stored in the dark. During this dark storage, the 2-propanol concentration decreased because of molecules' adsorption on the sample and the vessel surface. The concentration change was monitored using gas chromatography (GC-14A; Shimadzu Corp., Tokyo, Japan). That device was equipped with a flame ionization detector (FID) and a Sunpak-A column (Shimadzu Corp.). The carrier gas was nitrogen; the respective temperatures for the detector and injection port were 230°C and 200°C. The column temperature was 130°C. After adsorption, the equilibrium was confirmed, UV illumination was carried out using a

UV Illuminator (LA-410UV-1; Hayashi Watch Works, Japan) equipped with a Hg-Xe lamp (MX4010). This light source emits light with several peaks within 280–450 nm; the strongest peak is at 365 nm. The illumination intensity at the layer surface was 9 mW/cm^2 at 365 nm. Concentration of 2-propanol and acetone were evaluated every 30 min for 90 min.

3.3. Results and Discussion

3.3.1. Hybridization and HPA decomposition

3.3.1.1. Ion change method

Figure 3-9 portrays XRD patterns of $Zn_2Al(OH)_6(NO_3)\cdot 2H_2O$, the composites prepared in the EG solution, and that in water. In the EG solution, the ion-exchange ratio between NO_3^- and HPA was higher than that in water. The LDH layer thickness and the size of the Keggin anion are reported respectively as 0.48 nm and 0.98 nm. Basal spacing (d=1.48 nm, *003*) and *00l* harmonics (d=0.732 nm, *006*, 0.486 nm, *009*) after ion-exchange show good agreement with the sum of LDH layer thickness and the Keggin anion, implying that the ion-exchange process was attained. Furthermore, 1.48 nm spacing indicated that the gallery height was 0.98 nm. A salt-like impurity was detected as a broad peak at 1.16 nm. Many polyacid-LDH composites show such a characteristic impurity peak [28, 29].

In **Fig. 3-9,** the order of peak intensity by XRD on *00l* harmonics is, fundamentally, (009) > (006) > (003). This trend is common for both Keggin and lacunary Keggin ion intercalated LDHs such as $H_2W_{12}O_{40}$-Zn_2Al LDH [19] and $[SiW_{11}O_{40}]^{8-}$-Zn_2Al LDH [20]. Therefore, the (003) peak is weaker than the (006) and (009) peaks. The (003) peak might be detectable if we were to use high-power XRD or laminated samples.

Table 3-2 presents results of ICP analysis. The expected atomic ratio (Al:Zn:W), as calculated from the ion-exchange capacity, is 1:2:1.38 if the interlayer NO_3^- is replaced completely with $[SiW_{11}O_{39}]^{8-}$ in the $Zn_2Al(OH)_6NO_3$ system. Practical values obtained through ICP analyses were 1:1.4:0.52 for the composite using EG solution and 1:1.6:0.61 for the composite using water (**Table 3-2**), which implies that the ion-exchange capacities used for $[SiW_{11}O_{39}]^{8-}$ were 37% (EG solution) and 44% (water). The composite ion-exchange in water exhibited higher W contents. However, the presence of a salt-like impurity might affect the Zn:Al:W ratio. A part of the positive layer charge might be compensated by the OH^- anion and the remaining NO_3^- ion.

The IR spectra of the composites are depicted in **Fig. 3-10**. Characteristic HPA peaks were present in all composites. **Table 3-3** shows peak positions of IR spectra of the composite and K salt of HPAs. The composite peak positions differed from those on the $[SiW_{12}O_{40}]^{4-}$ ion; peak patterns resembled those of $[SiW_{11}O_{39}]^{8-}$ and its composite reported by Hu et al. The *d*-value and gallery height on $[SiW_{11}O_{39}]^{8-}$-Zn_2Al LDH were reported respectively as 1.452 nm and 0.98 nm. Based on these results, the interlayer HPA might be lacunary $[SiW_{11}O_{39}]^{8-}$ or a similar species. In solution, lacunary species possess higher charges than $[SiW_{12}O_{40}]^{4-}$ ion. Moreover, $[SiW_{12}O_{40}]^{4-}$ is stable only when pH is less than 6. After reflux treatment, the pH of the solution was around 8. For that reason, $[SiW_{12}O_{40}]^{4-}$ was decomposed into $[SiW_{11}O_{39}]^{8-}$; then, selective intercalation occurred during the ion-exchange reaction. The specific surface area, total pore volume, and average pore size of the obtained LDHs are presented in **Table 3-4**. The order of the specific surface area is $Zn_2Al(NO_3)\ 2H_2O$ < HPA-Zn_2Al LDH composite (ion-exchanged in water) < HPA-Zn_2Al LDH composite (ion-exchanged in EG solution). Intercalated HPA anion served as pillars and increased the gallery height, thereby increasing the specific surface area.

3.3.1.2. Reconstruction method

Figure 3-11 portrays XRD patterns of Mg-Al(CO_3) LDHs and Mg-Al composites prepared using the reconstruction method. The layer structure of Mg-Al(CO_3) LDHs was destroyed and their peaks were eliminated by heat treatment at 500°C. After reconstruction, new peaks appeared. Although the peaks were broader than those of ion-exchange composites in Zn-Al LDH, basal spacing (*d*=1.45 nm, *003*) and *00L* harmonics (*d*=0.735 nm, *006*, 0.486 nm, *009*) indicated that ion exchange was attained. A broad peak at 1.07 nm (2θ=8.3 deg) represents an impurity that is commonly observed in HPA-LDH composites.

Similarly to Zn-Al(NO_3) LDH, the IR spectra seem to show that $[SiW_{11}O_{39}]^{8-}$ was intercalated in this system. **Figure 3-10** shows the SiW_{12} and composite IR spectra. The peak position is presented in **Table 3-3**. The composites' peak positions differed from those of the $[SiW_{12}O_{40}]^{4-}$ anion. The peak patterns resembled those of $[SiW_{11}O_{39}]^{8-}$. **Table 3-5** presents results of ICP elemental analysis. The ideal molar ratio (Al:Mg:W) of the Mg_2Al LDH system would be 1:2:1.38 if reconstruction were attained completely with $[SiW_{11}O_{39}]^{8-}$. Regarding the Mg_4Al system, the ideal ratio is 1:4:1.38. Compared with the ICP results presented in **Table 3-6** (1:1.7:1.1 and 1:3.3:0.7), the ion-exchange capacity used for $[SiW_{11}O_{39}]^{8-}$ was 81% in the case of Mg_2Al-LDH, and 50% in the Mg_4Al-LDH system. The decrease of the Mg/Al ratio before and after ion exchange reflects leaching of LDH by HPA. The HPA-Mg_2Al composite contained a larger amount of W than the HPA-Mg_4Al composite. A larger layer charge is advantageous for HPA anion intercalation. The composite prepared using the reconstruction process exhibits a lower specific surface area than the original Mg-Al(CO_3) LDHs (**Table 3-6**). Rives et al. reported that a specific surface area increase was not observed in Zn-Al LDH-Keggin preparation [28]. Gardner et al. reported that Zn-based LDH intercalated with a Keggin-type HPA ($H_2W_{12}O_{40}$) is nonporous after outgassing at 70°C [25]. They attributed this result to the poor accessibility to the interlayer space for N_2 and organic substances when occupied by solvated Keggin anion. In the present study, the Mg_2Al composite contained a larger amount of $[SiW_{11}O_{39}]^{8-}$ than the Mg_4Al-LDH composite and the Zn_2Al-LDH composite, which is one reason for the nonporous structure of the Mg_2Al composite. Incomplete ion exchange would be a key factor for preparation of the porous structure. Deposition of salt-like impurities might also signal an important effect on the result of the specific surface area.

Characterization of the interlayer $[SiW_{11}O_{39}]^{8-}$ is carried out using XRD and IR spectra in this study. The gallery height of LDH is known to be equivalent to the interlayer polyacid size [14, 20, 21]. Other decomposed species of Keggin ion, e.g. $[SiW_9O_{34}]^{10-}$, are smaller than 1.0 nm. For that reason, d-spacing should decrease to less than 1.48 if these anions were intercalated. The ratio between Si and W is important information that is useful to identify the HPA structure. However, interlayer $[SiW_{11}O_{39}]^{8-}$ characterization by ICP analysis was almost impossible in this case because of the interference with Si contamination from the glass flask at LDH synthesis and existence of the salt-like impurity. At present, IR yields direct evidence of $[SiW_{11}O_{39}]^{8-}$ intercalation. Detailed characterization of intercalated ions using other spectroscopic analyses is now underway.

3.3.2. Photocatalytic activity of HPA-LDH

Papaconstantiou et al. investigated the 2-propanol decomposition pathway by HPA [18]. The initial step is 2-propanol decomposition to acetone. Consequently, acetone was oxidized at a very slow rate and was finally decomposed to CO_2 and H_2O. Some intermediates are expected to exist between acetone and CO_2, but they have not been identified. Different decomposition rates of 2-propanol and acetone were indicated by the low reaction rate of acetone with ·OH radical. **Figure 3-12** depicts the 2-propanol concentration change during UV illumination. The initial 2-propanol concentration (C_0) was 17.6 ppm after dark storage. First, 2-propanol concentration was increased and then decreased at a low reaction rate. Acetone was not detected using gas chromatography. The HPAs have good affinity with organic molecules [7]; therefore, the generated acetone and most of the 2-propanol was adsorbed by the sample. The decrease of 2-propanol concentration at the first step might be attributed to photo-induced desorption. The subsequent decrease is expected to be the result of photocatalytic decomposition.

Photocatalytic activity of the $[SiW_{11}O_{39}]^{8-}$-Zn_2Al LDH composite was shown to be very low in comparison to anatase TiO_2. Some possible causes are the intrinsically low quantum yield of HPA photoreaction [15] and the only slightly accessible interlayer gallery and UV screening effect by LDH. For HPA homogeneous reactions in aqueous solution, the excited state lifetime is on the order of nanoseconds. The quantum yield is 1–3% [15], as calculated from homogeneous reaction; however, in a heterogeneous reaction, this value must be lower. In addition, substance diffusion is restricted in the interlayer gallery.

The HPA photocatalysts have stronger oxidation power. However, the reaction efficiency was quite low in the heterogeneous reaction; the $[SiW_{11}O_{39}]^{8-}$-Zn_2Al LDH composite exhibited low photocatalytic activity. The HPA-LDH heterogeneous photocatalytic reaction is not preferable for practical gas purification. A different approach is necessary for the use of HPA as a photocatalyst.

3.4. Conclusion

For the investigations described in this chapter, we prepared W-based HPA-LDH composites; the effects of intercalation processes on the composite character and the stability of the Keggin structure were investigated. The HPA-LDH composites were prepared using ion-exchange method on Zn-Al(NO_3) LDH (Zn/Al=2) and reconstruction method on Mg-Al(CO_3) LDHs (Mg/Al=2, 4). Both IR and chemical analyses suggest that $[SiW_{12}O_{40}]^{4-}$ was hydrolyzed to $[SiW_{11}O_{39}]^{8-}$ during ion change when $H_4SiW_{12}O_{40}$ was used as a starting material for HPA. The photocatalytic activity of $[SiW_{11}O_{39}]^{8-}$-Zn_2Al LDH composite was quite low in gaseous 2-propanol decomposition. Because of the low accessibility and UV screening, the photocatalytic reaction in interlayer gallery might not improve effectively. Some other supported method or other catalyst design will be necessary to enable the use of solid HPA as a photocatalyst.

References

[1] Yamase, T. *Chem. Today*, **418**, 42-49 (2006) in Japanese.

[2] Okuhara, T.; Mizuno, N.; Misono, *M. Adv. Catal.*, **41**, 113-252 (1996).

[3] Kozhevnikov, I. V. *Chem. Rev.*, **98**(1), 171-198. (1998).

[4] Mitsutani, A. *Catalysis Today*, **73**(1-2), 57-63 (2002).

[5] Okuhara, T.; Kasai, A.; Hayakawa, N.; Misono, M.; Yoneda, Y. *Chem. Lett.*, 391 -394 (1981).

[6] Misono, M. *Catal. Rev. Sci. Eng.*, **29**(2-3), 269-321 (1987).

[7] Misono, M.; Mizuno, N.; Katamura, K.; Kasai, A.; Konishi, Y.; Sakata, K.; Okuhara, T.; Yoneda, Y. *Bull. Chem. Soc. Jpn.*, **55**(2), 400-406 (1982).

[8] Misono, M. *Mater. Chem. Phys.*, **17**(1-2), 103-120 (1987).

[9] Okuhara. T. *Chem. Rev*. **102**, 3641-3666 (2002).

[10] Yamase, T. *Catal. Surveys from Asia*, **7**(4), 203-217 (2003).

[11] Hiskia, A.; Mylonas, A.; Papaconstantinou, A. *Chem. Soc. Rev.*, **30**, 62-69 (2001).

[12] Hill, C. L.; Bouchard, D. A. *J. Am. Chem. Soc.*, **107**, 5148-5157 (1985).

[13] Yamase, T. *Chem. Rev.*, **98**, 307-325 (1998).

[14] Hiskia, A.; Papaconstantinou, E, *Inorg. Chem.*, **31**, 163-167 (1992).

[15] Borrás-Almenar, J. J.; Coronado, E.; Müller, A.; Pope, M. *Polyoxometalate Molecular Science*; Kluwer Academic Publishers: Dordrecht / Boston / London, 381-416 (2001).

[16] Barteau, K. P.; Lyons, J. E.; Song, I. K.; Barteau, M. A. *Topics in Catal.*, **41**(1-4), 55-62 (2006).

[17] Nosaka, Y.; Nosaka, A. *Nyumon hikarishokubai*; Tokyo Tosho Co., Ltd.: Tokyo

(2004) in Japanese.

[18] Mylonas, A.; Hisaka, A.; Androulaki, E.; Dimotikali, D.; Papaconstantiou, E. *Phys. Chem. Chem. Phys.*, **1**, 437-440 (1999).

[19] Khan, A. I.; O'Hare, D. *J. Mater. Chem.*, **12**, 3191-3198 (2002).

[20] Kikkawa, S.; Koizumi, M. *Mater. Res. Bull.*, **17**, 191-198 (1982).

[21] Kameda, T.; Yoshioka, T.; Mitsuhashi, T.; Uchida, M.; Okuwaki, A. *Water Research*, **37**, 1545-1550 (2003).

[22] Badreddine, M.; Legrouri, A.; Barroug, A.; Roy, A. D.; Besse, J. P. *Mater. Lett.*, **38**, 391-395 (1999).

[23] Carrado, K. A.; Kostapapas, A.; Suib, S. L. *Solid State Ionics*, **26**, 77-86 (1988).

[24] Reinholdt, M. X.; Kirkpatrick, R. J. *Chem. Mater.*, **18**, 2567-2576 (2006).

[25] Aisawa, S.; Takahashi, S.; Ogasawara, W.; Umetsu, Y.; Narita, E. *J. Solid State Chem.*, **162**, 52-62 (2001).

[26] Newman, SP; Jones, W. *New J. Chem.*, **22**(2), 105-115 (1998).

[27] Evans, D. G.; Xue D. *Chem. Commun.*, (5), 485-496 (2006).

[28] Rives, V; Ulibarri, M. A. *Coord. Chem. Rev.*, **181**, 61-120 (1999).

[29] Gardner, E.; Pinnavaia, T. J. *Applied Catalysis A*, **167**, 65–74 (1998).

[30] Hu, C.; He, Q.; Zhang, Y.; Wang, E.; Okuhara, T.; Misono, M. *Catalysis Today*, **30**, 141–146 (1996).

[31] Borrás-Almenar, J. J.; Coronado, E.; Müller, A.; Pope, M. *Polyoxometalate Molecular Science*; Kluwer Academic Publishers: Dordrecht / Boston / London, 41-43 (2003).

[32] Kameshima, Y.; Yoshizaki, H; Nakajima, A; Okada, K. *J. Colloid and Interface Sci.*, **298**(2), 624-628 (2006).

[33] Kwon. T; Pinnavaia, T. J. *Chem. Mater*., **1**, 381-383 (1989).

[34] Hu, C.; He, Q.; Zhang, Y.; Liu, Y.; Zhang, Y.; Wang, E. *Chem. Commun*., (2), 121-122 (1996).

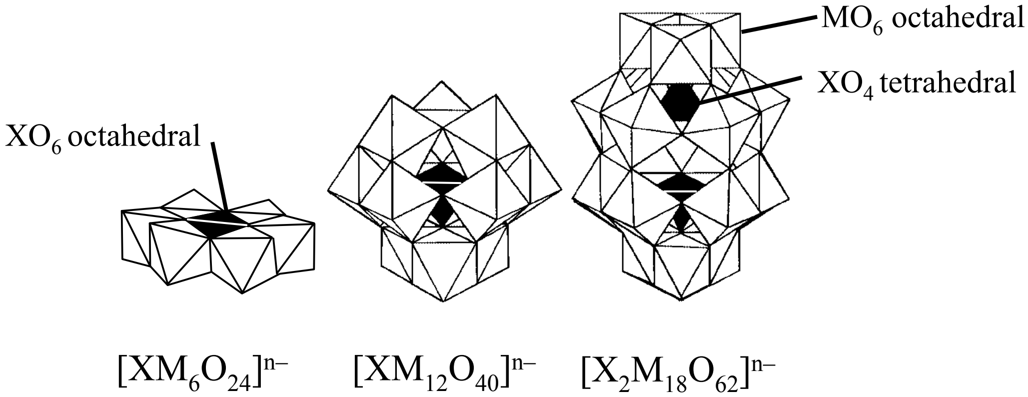

Figure 3-1. Structure of typical HPAs: (a) Anderson structure, X has octahedral coordination; (b) Keggin structure, X has tetrahedral coordination; (c) Dawson structure, X has tetrahedral coordination. Ref) Misono, M. *Chem. Commun.*, [13], 1141-1152 (2001).

Table 3-1 Electron delocalization parameters in one-electron heteropoly blues

Reduced polyanion	E_{th} (eV)	E_{op} (eV)
$W_6O_{19}^{3-}$	0.055	1.27
$W_5NbO_{19}^{4-}$	0.075	1.36
$H_2W_{12}O_{40}^{7-}$	0.035	1.04
$SiW_{12}O_{40}^{5-}$	0.035	1.0
$As_2W_{18}O_{62}^{7-}$	0.040	1.38
$AsH_2W_{18}O_{60}^{8-}$	0.040	1.18
$Mo_6O_{19}^{3-}$	0.155	1.125
α-$PMoO_{40}^{4-}$	0.035	1.07
α-$GeMo_{12}O_{40}^{5-}$	0.045	0.913
β-$SiMo_3W_9O_{40}^{5-}$	0.055	1.0
β-$W_{12}O_{40}^{6-}$	0.004	0.992
$W_{10}O_{32}^{5-}$	0.06	1.310

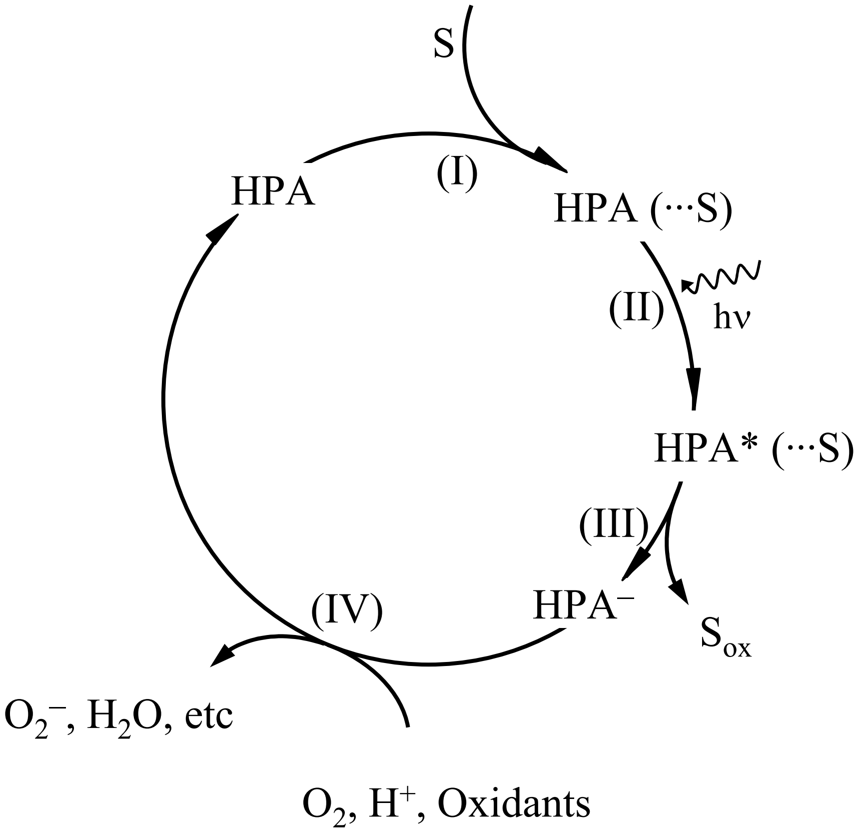

Figure 3-2. HPA photocatalytic reaction pathway: S, organic substance; (I) Preassociation with organic molecule or H_2O; (II) Excitation; (III) Photoredox reaction; (IV) Reoxidation, regeneration of catalyst [11].

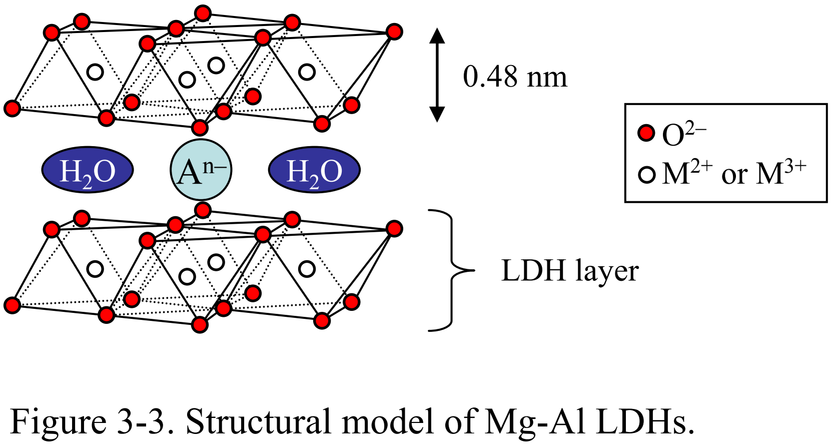

Figure 3-3. Structural model of Mg-Al LDHs.

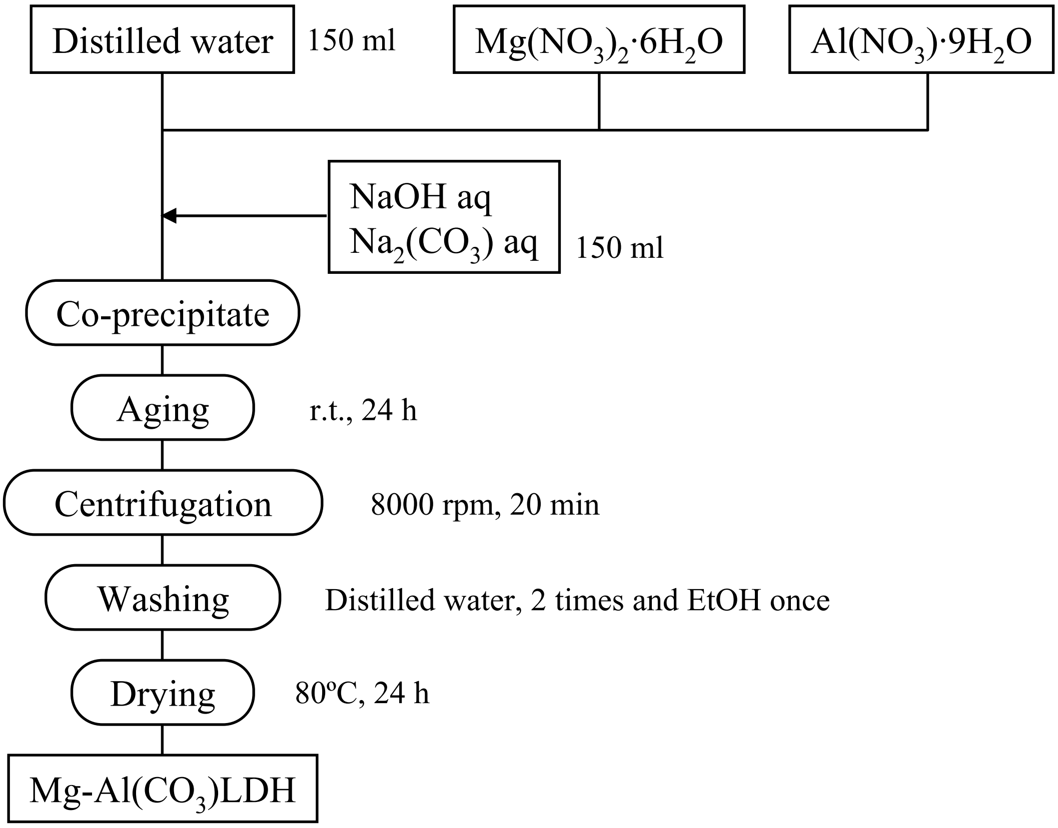

Figure 3-4. Experimental procedure of Mg-Al(CO_3) LDH preparation using co-precipitation method.

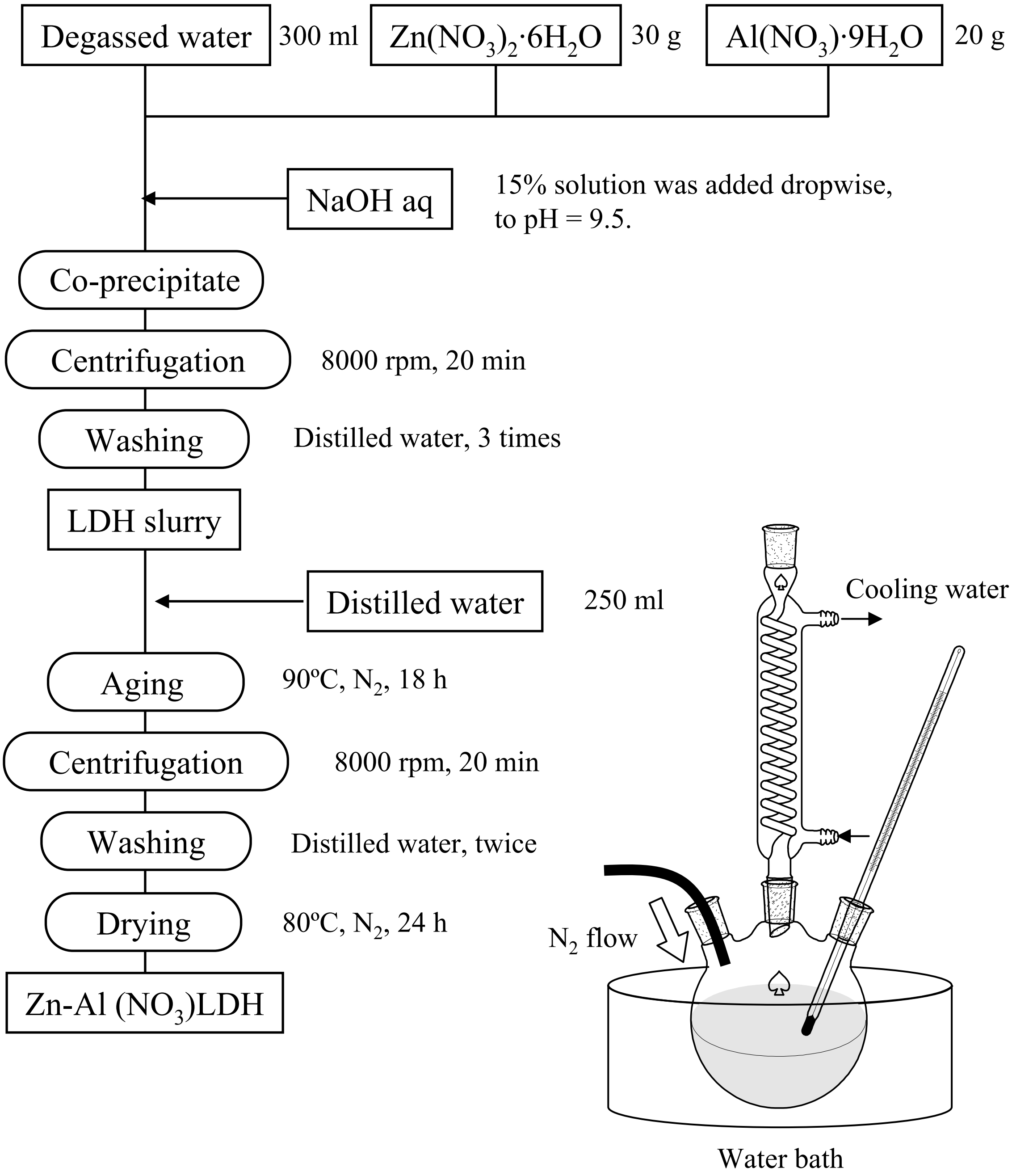

Figure 3-5. Experimental procedure of Zn-Al(NO_3) LDH preparation and schematic illustration of aging process.

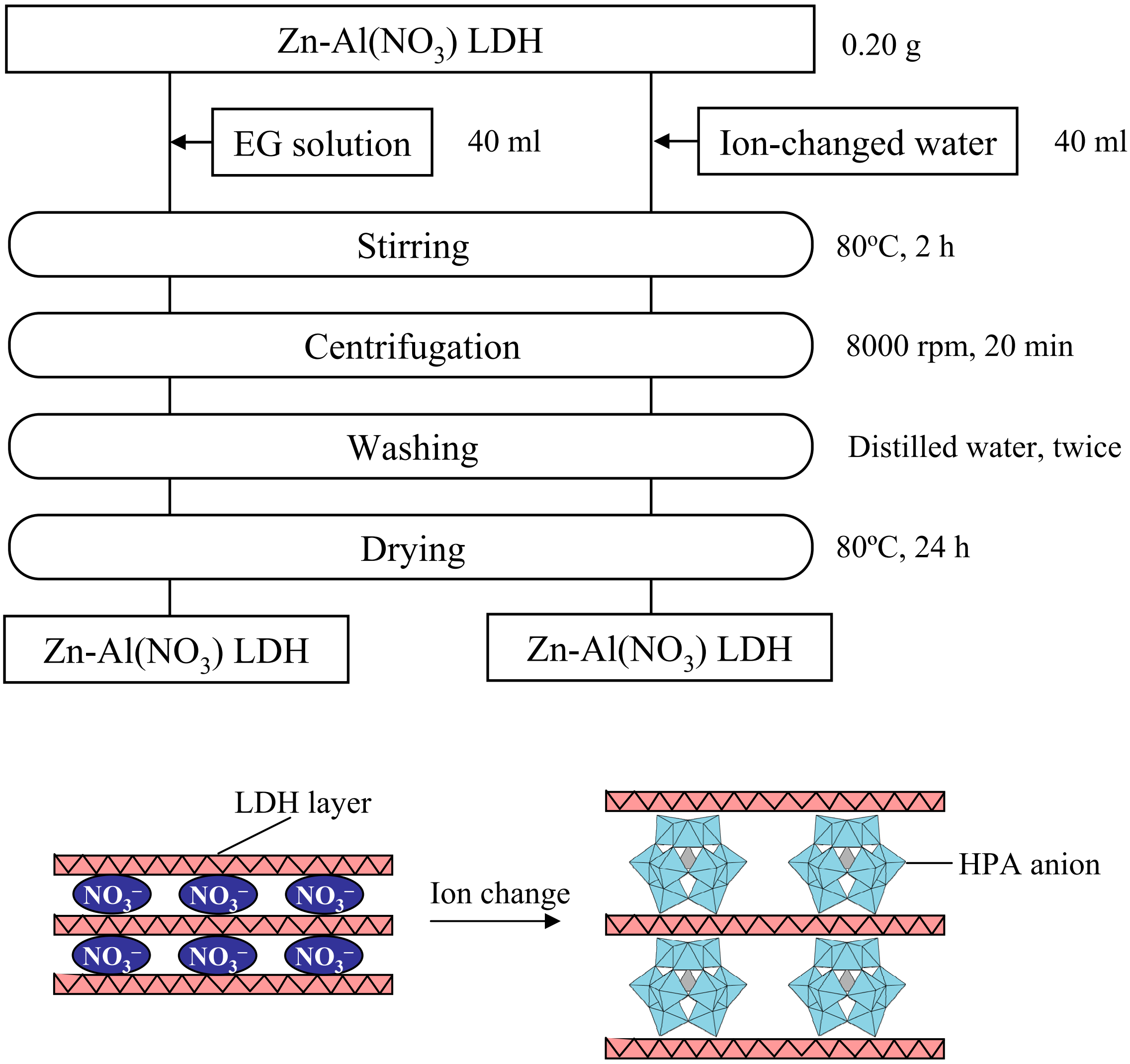

Figure 3-6. Experimental procedure of ion-change method.

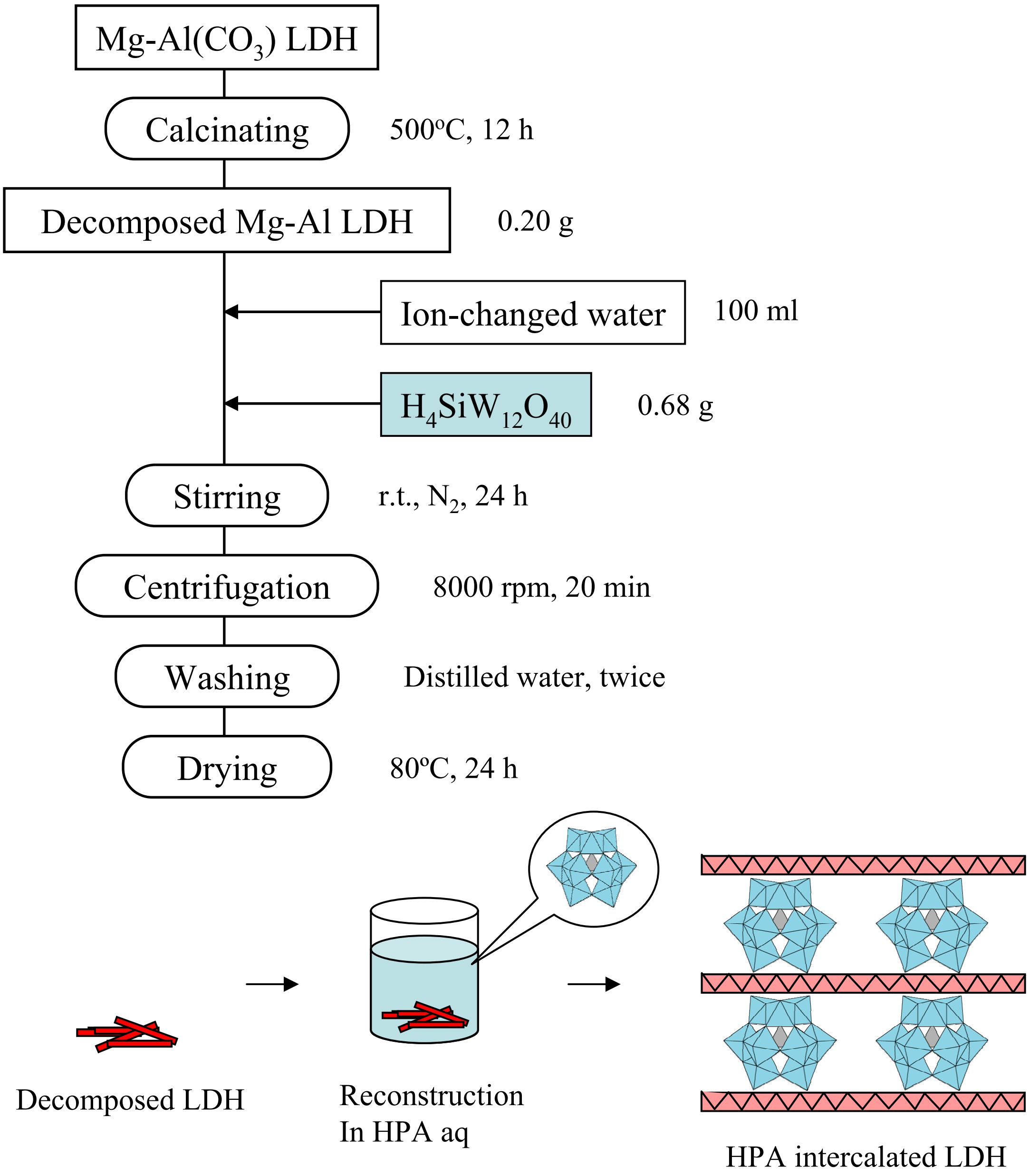

Figure 3-7. Experimental procedure of reconstruction method.

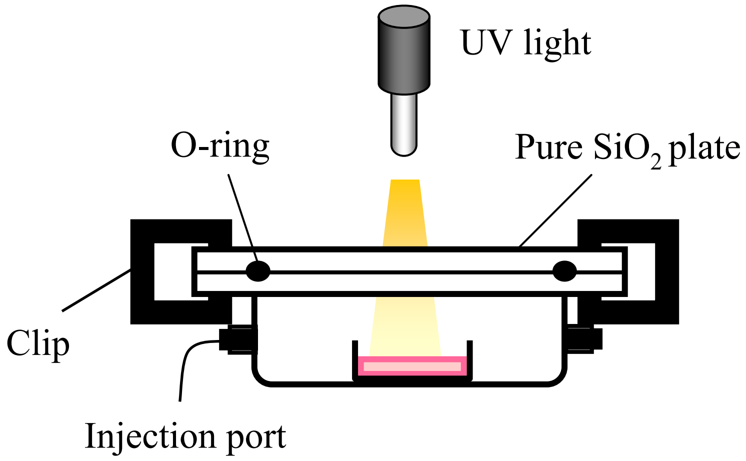

Figure 3-8. Schematic illustration of the setting for decomposition experiment.

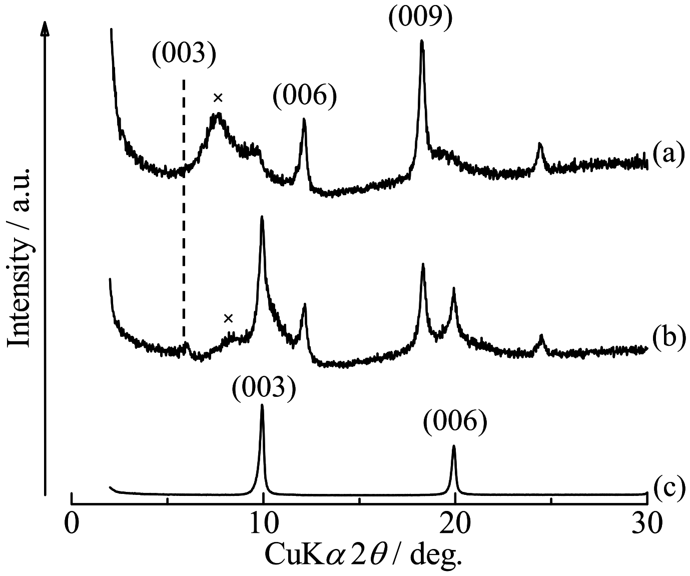

Figure 3-9. XRD patterns of composites prepared by ion-exchange: (a) After ion-change in EG solution; (b) after ion-exchange in water; (c) Zn-Al LDH before ion-change; x, a salt-like impurity [28].

Table 3-2. Chemical composition of Zn-Al LDH and composites

	Molar ratio		
sample	Al	Zn	W
$ZnAl_2$-NO_3LDH	1.0	2.1	—
After ion-exchange in EG solution	1.0	1.4	0.52
After ion-exchange in water	1.0	1.6	0.61

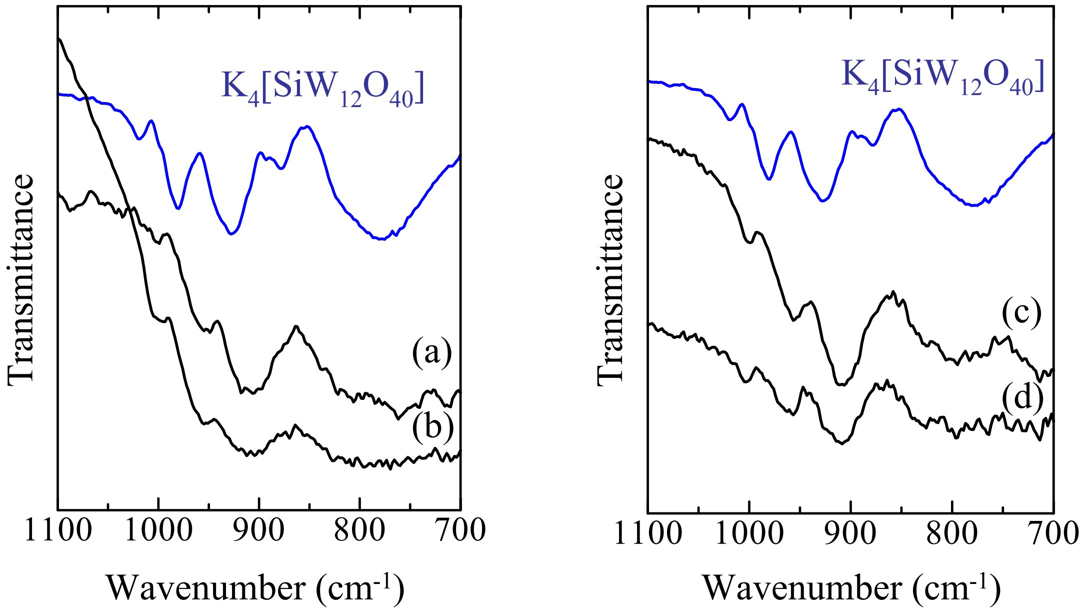

Figure 3-10. IR spectra of $K_4[SiW_{12}O_{40}]$ and LDH composites: (a) Zn-Al LDH composite by EG solution; (b) Zn-Al LDH composite by water; (c) Mg-Al LDH composite (Mg/Al = 2); (d) Mg-Al LDH composite (Mg/Al = 4).

Table 3-3. IR peak positions of composites and HPA (cm^{-1})

sample	Si-Oa	W=Od	W-Ob-W	W-Oc-W
Zn-Al LDH composite by EG solution	1000	952	908	
Zn-Al LDH composite by water	999	954	908	
Mg-Al LDH composite (Mg/Al=2)	1000	955	912	798
Mg-Al LDH composite (Mg/Al=4)	1000	954	908	
$ZnAl_2$-SiW_{11}*[1]	997	945	897	792, 728
SiW_{12}*[2]	930	982	885	792
SiW_{11}*[2]	1000	952	870	797, 725

*[1]Hu et al. [6] *[2]K salt

Table 3-4. Specific surface area, total pore volume and average pore size of LDHs

Sample	Specific surface area (m^2 / g)	Total pore volume (cm^3 / g)	Average pore size (nm)
$ZnAl_2LDH$	19	0.11	12
Zn-Al LDH composite by EG solution	57	0.12	4.3
Zn-Al LDH composite by water	43	0.11	5.2

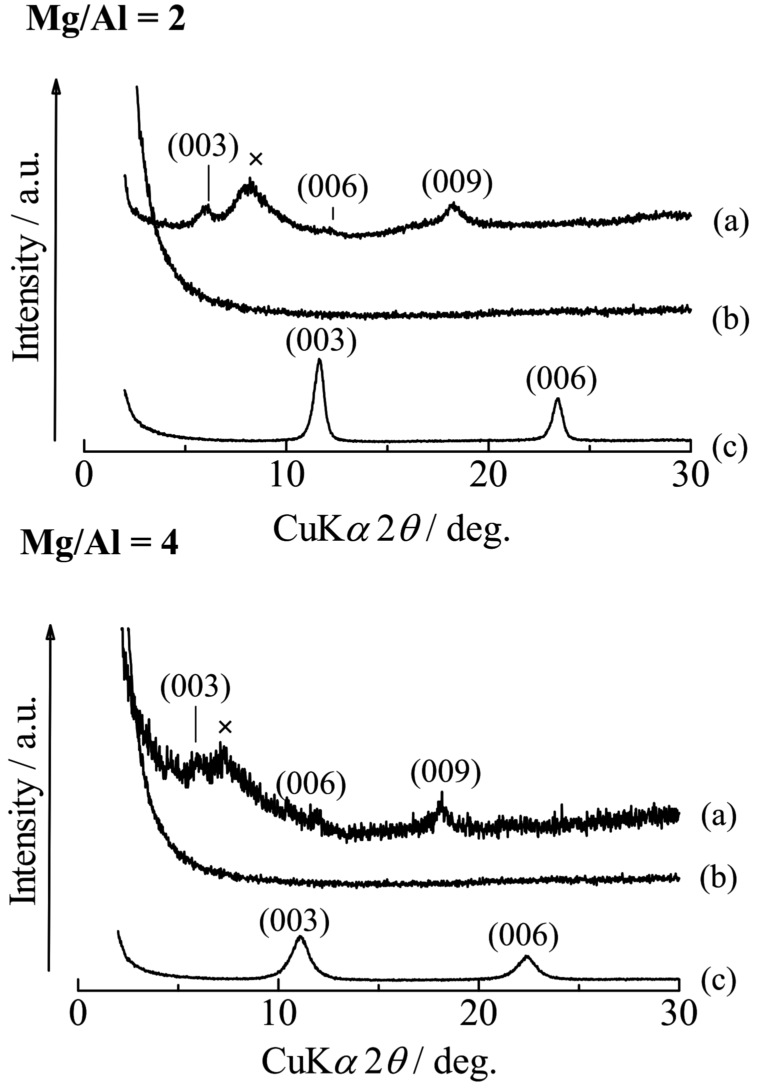

Figure 3-11. XRD patterns of composites prepared by reconstruction method: (a) Reconstructed LPA-LDH; (b) heat-decomposed LDH; (c) Mg-Al (CO_3) LDH before heat treatment.

Table 3-5. Chemical composition of Mg-Al LDH and composites

	Molar ratio		
Sample	Al	Mg	W
Mg_2Al-CO_3LDH	1.0	2.0	—
Mg-Al LDH composite (Mg/Al = 2)	1.0	1.7	1.12
Mg_4Al-CO_3LDH	1.0	4.0	—
Mg-Al LDH composite (Mg/Al = 4)	1.0	3.3	0.7

Table 3-6. Specific surface area, total pore volume and average pore size of LDHs

Sample	Specific surface area (m^2 / g)	Total pore volume (cm^3 / g)	Average pore size (nm)
Mg_2Al-CO_3LDH	130	1.1	17
Mg-Al LDH composite (Mg/Al = 2)	<1	0.02	—
Mg_4Al-CO_3LDH	130	0.32	4.9
Mg-Al LDH composite (Mg/Al = 4)	85	0.09	2.1

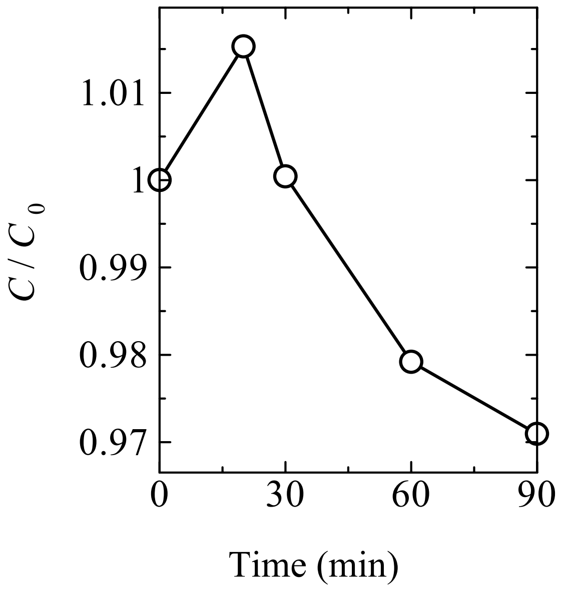

Figure 3-12. IPA concentration change during UV illumination (9 mW/cm^2) by HPA–Zn-Al composite.

CHAPTER 4

Preparation of Keggin-type Heteropolyacid and Isopolyacid-TiO_2 hybrid thin films

4.1. Introduction

4.1.1. Z-scheme

In plant photosynthesis, a high quantum yield photochemical reaction is achieved by antenna complexes, two photosynthetic reaction centers, and an electron transport chain (**Fig. 4-1**). Such systems include a two-step photoexcitation system and charge transfer, called a Z-scheme, which provides high charge-separation efficiency and a wide range of wavelength utilization. Therefore, many researchers have designed Z-schemes for high-performance photoreactions [1–3]. Keggin-type HPA and IPA ($H_n[XW_{12}O_{40}]$, hereinafter denoted as XW_{12})-TiO_2 hybrids were investigated as Z-scheme photocatalytic systems in aqueous media [4–6]. The reduction potential of PW_{12} (+0.218 V vs. NHE), SiW_{12} (+0.054 V vs. NHE), H_2W_{12} (${}^{-}$0.162 V vs. NHE) [7] is lower than the conduction band level of TiO_2 (${}^{-}$0.5 V vs. NHE) [8]. **Figure 4-2** portrays a schematic illustration of the photoexcitation and electron transportation of a XW_{12}-TiO_2 system; **Fig. 4-3** portrays an energy diagram. In this system, Keggin ions act as electron scavengers of TiO_2. Reduced XW_{12} (XW_{12}^{-}) absorbs visible light to form an excited state XW_{12}^{-} (XW_{12}^{-*}). Then it reduces organic compounds such as methyl viologen or methyl orange in water [5, 6]. However, to date, all examinations have been carried out in aqueous solutions. In this work, photocatalytic decomposition activities of Keggin-type HPA-TiO_2 and IPA-TiO_2 hybrids were investigated in gaseous phase under various illumination conditions. In this system, a high decomposition rate was expected because of the electron scavenger effect and adsorption of organic molecules by XW_{12}.

4.1.2. Layer-by-layer method

Layer-by-layer (LBL) method is a self-assembly process used for thin film fabrication. **Figure 4-4** presents a schematic illustration of LBL method [9, 10]. Strong electrostatic attraction causes alternating deposition of oppositely charged species on the substrate. Advantages of this method are: 1) easy processing of a nano-order composite, 2) easy control of the coating thickness by changing deposition times, and 3) various available combinations of building blocks. Multilayer films such as polyelectrolytes [11], inorganic colloid particles [12, 13], nanosheets [14], and biomolecules [15, 16] have been prepared using LBL method. New approaches using hydrogen bonding [16] or van der Waals interaction [17] have also been reported.

Polyacids have also been used as building blocks in LBL systems. Various polyacid-polyelectrolyte hybrids have been reported using small $[W_{10}O_{32}]^{4-}$ to large clusters such as $[Mo_{132}O_{372}(CH_3COO)_{30}(H_2O)_{72}]^{42-}$ [18]. Generally, deposition behavior depends deeply on polyacid ion charge and size [18–20]. Liu et al. noted that the presence of electrolyte in solution decreases the repulsion force between ions and increases the deposition amount [18]. They also reported that hybrid films are robust and permeable for small molecules.

4.1.3. Objective

The XW_{12} and TiO_2 systems are expected to exhibit high photocatalytic activity because of the Z-scheme reaction [5]. For this chapter, we prepared transparent $(XW_{12}/TiO_2)_n$ (X = P, Si, H_2) hybrid thin films using LBL method with TiO_2-sol and

Keggin ion solution. Reference thin films, $(TiO_2)_n$ and $(PW_{12})_n$ were also prepared using LBL method and UV illumination. Deposition behavior was investigated from spectroscopic studies and surface morphology observation for each thin film sample.

4.2. Experimental Procedure

4.2.1. Preparation of Keggin ion/TiO_2 hybrid thin films

4.2.1.1. $(PW_{12}/TiO_2)_n$ hybrid thin film

For XW_{12}/TiO_2 film preparation, a commercial TiO_2 aqueous suspension (STS-100; 20 wt% concentration; Ishihara Sangyo Kaisha Ltd., Mie, Japan) was used as the starting material. The suspension contains HNO_3 as a stabilizer to maintain a well-dispersed state of anatase nanoparticles. Transmission electron microscope (TEM) observations revealed that the suspension contains monodispersed anatase nanoparticles with dimensions of 5–7 nm. This suspension was diluted with aqueous solutions of reagent-grade HNO_3; then, 0.004–0.4 g dm^{-3} (2, 5, 10, 20, 50 mg dm^{-3}, 0.1, 0.2, 0.4 g dm^{-3}) suspensions were prepared. Actually, PW_{12} requires low pH (< 2) to prevent its hydrolysis [21]. The TiO_2 particles have sufficient positive charge for maintaining a well-dispersed state and for layer-by-layer coating using Coulombic attraction with PW_{12} molecules. For those reasons, the pH values of these TiO_2 suspensions were adjusted to 1.5 using HNO_3. Actually, 12 tungsto(VI)phosphoric acid n-hydrate ($H_3PW_{12}O_{40}$ (PW_{12}); Wako Pure Chemical Industries Ltd., Tokyo, Japan) was used with no purification. This chemical was dissolved into diluted HNO_3 solution; the PW_{12} aqueous solution (0.9 mM, calculated as M = 3399, $PW_{12}O_{40}\cdot 29H_2O$, pH value was adjusted to 1.5) was prepared.

Figure 4-5 portrays the experimental procedure used for preparation of $(XW_{12}/TiO_2)_n$ films. Pure quartz (SiO_2) glass plates (30 mm×60 mm×1 mm; Tosoh Corp., Tokyo Japan) and Si (100) wafers (40 mm×60 mm×0.5 mm; Aki Corp., Miyagi, Japan) were used as substrates. After normal cleaning procedures substrates were soaked in a bath of 1:1 methanol/HCl and then conc. H_2SO_4 for 30 min each [22, 23]. Substrates were soaked in distilled water and ultrasonicated for 10 min. First, these substrates were immersed into PW_{12} solution for 20 min. The substrates' surface is positively charged in an acid solution. Then the first layer of PW_{12} molecules was adsorbed onto the surface of substrates by Coulombic potential. After immersion, the substrates were rinsed twice using diluted HNO_3 (pH=1.5) solution to remove excess PW_{12}. Subsequently, the substrates were dried at 60°C in an oven under air atmosphere for 15 min. Second, PW_{12} coated substrates were immersed into a TiO_2 suspension for 20 min. Then they were rinsed twice with diluted HNO_3. The substrates were dried in the same conditions as those for PW_{12} coating. The PW_{12}-TiO_2 hybrid thin films were prepared by alternate immersion and washing processes. Hereinafter, the PW_{12}-TiO_2 hybrid thin film with *n* times bilayer deposition is designated as a $(PW_{12}/TiO_2)_n$ hybrid film.

4.2.1.2. $(SiW_{12}/TiO_2)_n$ hybrid thin film

The TiO_2 suspensions (0.2, 0.4, 0.6 g dm^{-3}) used for this study were prepared by dilution of TiO_2 sol and adjusted pH = 1.5 using diluted HNO_3. In addition, 12 tungsto(VI) silicic acid 26 hydrate ($H_4SiW_{12}O_{40}$ (SiW_{12}), Wako Pure Chemical Industries Ltd., Tokyo, Japan) was used with no purification. This chemical was dissolved into diluted HNO_3 solution; the SiW_{12} aqueous solution 0.9–3.6 mM (0.9, 1.8, 2.7, 3.6 mM) were prepared and adjusted pH = 1.5. First, substrates were immersed into the SiW_{12} solution for 20 min. They were then rinsed twice with diluted HNO_3 (pH = 1.5). The samples were dried at 60°C in an oven under air atmosphere. Second, the sample was immersed in TiO_2 suspension for 20 min and rinsed twice with diluted HNO_3 (pH = 1.5). The samples were dried at 60°C under air atmosphere. Then $(SiW_{12}/TiO_2)_n$ thin films were obtained by repeating these procedures.

4.2.1.3. (H_2W_{12}/TiO_2) hybrid thin film

The TiO_2 suspensions (0.2, 0.4, 0.6 g dm^{-3}) were prepared by dilution of TiO_2 sol and adjusted to pH = 1.5 using diluted HNO_3. For this experiment, Ammonium metatungstate n-hydrate ($(NH_4)_6[H_2W_{12}O_{40}]$, Wako Pure Chemical Industries Ltd., Tokyo, Japan) was used with no purification. This chemical was dissolved into diluted HNO_3 solution; the H_2W_{12} aqueous solution 0.9–3.6 mM (0.9, 1.8, 2.7, 3.6 mM, calculated as F.W. = 2956.45) were prepared and adjusted to pH = 1.5. First, substrates were immersed into the H_2W_{12} solution for 20 min. They were then rinsed twice with diluted HNO_3 (pH = 1.5). The samples were dried at 60°C in an oven under air atmosphere. Second, the sample was immersed in TiO_2 suspension for 20 min and rinsed twice with diluted HNO_3 (pH = 1.5). The samples were dried at 60°C under air atmosphere. Then $(H_2W_{12}/TiO_2)_n$ thin films were obtained by repeating these procedures.

4.2.2. Preparation of reference films

4.2.2.1. $(TiO_2)_n$ film

Control samples were prepared according to a process used in a study by Sasaki et al. [23]. The TiO_2 suspension (0.2 g dm^{-3}) was prepared using an identical procedure for $(PW_{12}/TiO_2)_n$ hybrid films. Polysodium 4-styrene sulfonate (PSS, average Mw ca. 70,000, 30 wt% aqueous solution; Aldrich Corp.) was used for preparation of control TiO_2 films (**Fig. 4-6(a)**). A PSS (7 g dm^{-3}) solution was prepared by dissolving a certain mass of PSS in a HNO_3 solution whose pH was 1.5. The experimental procedure is portrayed in **Fig.**

4-7. First, substrates were immersed into the PSS solution for 20 min. They were then rinsed twice with diluted HNO_3 (pH = 1.5). The samples were dried at 60°C in an oven under air atmosphere. Second, the sample was immersed in TiO_2 suspension for 20 min and rinsed twice with diluted HNO_3 (pH = 1.5). The samples were dried at 60°C under air atmosphere. Then $(PSS/TiO_2)_n$ thin films were obtained by repeating these procedures. After deposition, the samples were illuminated for 6 h using UV light from a Hg-Xe lamp to decompose the interlayer PSS. The illumination intensity at the sample surface was 66 mW/cm^2 at λ = 365 nm. Thereby, $(TiO_2)_n$ samples were obtained.

4.2.2.2. Preparation of $(PW_{12})_n$ film

For preparation of the control PW_{12} thin films, poly(diallyldimethylammonium chloride) (PDDA, typical Mw 100,000–200,000, 20 wt% aqueous solution; Aldrich Chemical Co. Inc.) was used as a counter polymer (**Fig. 4-6(b)**). A PDDA (20 g dm^{-3}) solution was prepared by dissolving a certain mass of PDDA in a HNO_3 solution of pH 1.5. The experimental procedure is portrayed in **Fig. 4-8**. First, substrates were immersed into the PW_{12} solution for 20 min. They were then rinsed twice with diluted HNO_3 (pH = 1.5). The samples were dried at 60°C in an oven under an air atmosphere. Then the sample was immersed in PDDA solution for 20 min and rinsed twice with diluted HNO_3 (pH = 1.5). The samples were dried at 60°C under an air atmosphere. Subsequently, $(PDDA/PW_{12})_n$ thin films were obtained by repeating these procedures. After deposition, UV light was illuminated onto the samples using a Hg-Xe lamp for 16 h to decompose the interlayer PSS. The illumination intensity at the sample surface was 66 mW/cm^2 at λ = 365 nm. Finally, $(PW_{12})_n$ samples were obtained.

4.2.3. Characterization

Using a UV-VIS-NIR scanning spectrophotometer (V-630; Jasco Inc., Tokyo, Japan), UV-vis absorption spectra were evaluated. The infrared spectra of the thin films on Si substrate were recorded using a Fourier transform infrared spectrophotometer (FT-IR, 8600PC; Shimadzu Corp., Kyoto, Japan). Transmission mode was used with an incidence angle of 75° (Brewster's angle). Reflectance spectra were measured using another UV-VIS-NIR scanning spectrophotometer (UV-2400; Shimadzu Corp., Kyoto, Japan) with an integrating sphere. The surface chemical composition was measured using X-ray photoelectron spectroscopy (XPS, 5500MC; Perkin-Elmer Phi Co., U.S.A.) with a Mg Kα X-ray line (46.950 eV). The takeoff angle was 45°. The binding energy scales were referenced to 284.5 eV, as determined according to locations of peaks on the C1s spectra of hydrocarbon (CH_x) for correcting the deviation. The respective microstructures of the hybrid thin films were observed using a scanning electron microscope (SEM: S4200; Hitachi Ltd., Tokyo Japan). Their layer thicknesses were estimated using a surface profiler (Dektak3; Ulvac Technologies Inc., Kanagawa, Japan) with a diamond-tipped stylus (r = 12.5 μm). Its vertical resolution was 0.5 nm. The scan length was 5000 μm; data points were 2000. The prepared films' respective morphologies were evaluated using the noncontact-mode of an atomic force microscope (AFM, JSPM 5200; JEOL, Tokyo, Japan). A Pt-Ti coated Si cantilever (force constant: 0.95 N/m) was used for this measurement.

4.3. Results and Discussion

4.3.1. $(XW_{12}/TiO_2)_n$ films

Figure 4-9 presents a schematic illustration of the layer-by-layer method. In an acid solution, the Coulomb force adsorbed negatively charged XW_{12} anion and positively charged TiO_2 particles. The PW_{12}/TiO_2 bilayer was thickened through alternate immersion. **Figure 4-10(a)** shows the TiO_2 suspension concentration dependence of the absorbance of the $(PW_{12}/TiO_2)_n$ hybrid film at $\lambda = 248$ nm. The absorbance increased with increasing TiO_2 suspension concentration up to 0.1 g dm^{-3} and then saturated. Based on this result, we determined the concentration of TiO_2 suspension for film processing to 0.2 g/L. Subsequent experiments were carried out using this TiO_2 suspension. The absorption change was not remarkable in comparison to the withdrawal rate (1–10 mm/s) and the immersion time when it was longer than 20 min. **Figure 4-10(b)** shows the dependence of UV-vis absorption spectra on the layer number of the $(PW_{12}/TiO_2)_n$ hybrid films. Both PW_{12} and TiO_2 possess absorption bands in UV region. Therefore, absorbance was increased with both depositions.

In preparation of $(SiW_{12}/TiO_2)_n$ film, UV absorbance increment was smaller than that of the $(PW_{12}/TiO_2)_n$ film. **Table 4-1** presents the UV absorbance per bilayer at $\lambda = 248$ nm under various concentration conditions. The deposition amount depended on both SiW_{12} and TiO_2 concentrations within a wide range; higher concentration was necessary for saturation than in the PW_{12} case. Based on this result, we determined that the concentrations of SiW_{12} and TiO_2 were 3.6 mM and 0.4 g dm^{-3}. Subsequent experiments were carried out using these solution and suspension. From results of a previous study, Fournier reported that electrostatic phenomena of XM_{12}s in aqueous solution are affected by the polyanion charge. The SiW_{12} anion (4-) exhibits stronger repelling anion–anion interaction than PW_{12} anion (3-) does. For that reason, highly dispersed SiW_{12} loading is difficult [24]. Strong repulsion force is expected to require a highly concentrated solution for saturation. **Figure 4-11** portrays the dependence of UV-vis absorption spectra on the layer number of the (SiW_{12}/TiO_2) hybrid films. The UV absorbance was increased by both SiW_{12} and TiO_2 deposition because SiW_{12} possesses an absorption band in the UV region, as does PW_{12}.

In addition, $(H_2W_{12}/TiO_2)_n$ films were prepared using LBL method. **Figure 4-12(a)** portrays the absorbance change of $(H_2W_{12}/TiO_2)_n$ hybrid films at λ = 248 nm when the H_2W_{12} ammonium salt concentration was changed. No marked change in the amount of deposition was observed from 0.9 mM to 2.7 mM. Moreover, when the TiO_2 concentration was increased from 0.2 g, the deposition amount was not changed. Based on these results, we determined the concentrations of H_2W_{12} ammonium salt and TiO_2 as 0.9 mM and 0.2 g dm^{-3}. Subsequent experiments were carried out using this condition. In $(H_2W_{12}/TiO_2)_n$ film preparation, the deposition amount saturated at low concentration (0.9 mM) despite the high anion charge (-6). The strong repulsion force was shielded by coexistent NH_4 ions in the polyanion solution [18]. **Figure 4-12(b)** depicts the dependence of UV-vis absorption spectra on the layer number of the $(PW_{12}/TiO_2)_n$ hybrid films. Both H_2W_{12} and TiO_2 possess absorption bands in the UV region. Therefore, absorbance was increased with both depositions.

The spectra for $(XW_{12}/TiO_2)_6$ hybrid films imply that transmittance in the visible area (λ = 400–780 nm) was higher than 83% for $(PW_{12}/TiO_2)_6$, 84% for $(SiW_{12}/TiO_2)_6$, 86% for $(H_2W_{12}/TiO_2)_6$. An optical micrograph of the hybrid thin films is portrayed in **Fig. 4-13.** All had high transparency. Average absorbance increments at saturated conditions are portrayed in **Table 4-2**. The deposition amount decreased with increasing anion charge. Both the charge balance between XW_{12} anion and TiO_2 surface and increasing of the anion-anion repulsion force are expected to affect the deposition amount. **Figure 4-14** depicts the reflectance spectra of the $(XW_{12}/TiO_2)_6$ hybrid films and reference $(TiO_2)_6$

films. Reflectance at λ = 248 nm was 0.228 for $(PW_{12}/TiO_2)_6$, 0.209 for $(SiW_{12}/TiO_2)_6$, and 0.238 for $(H_2W_{12}/TiO_2)_6$. Using absorbance and reflectance spectra, the TiO_2 packing density is calculable. Based on Sasaki's method [23, 25], the real absorbance is represented as

$$T = 1 - R - A,$$

where T is the transmittance, R is the reflectance, and A is the damping ratio attributable to actual absorbance. For the $(PW_{12}/TiO_2)_6$ hybrid film, the apparent absorbance was 0.774 (= 0.129 × 6). This value is converted to T = 0.168. Based on reflectance spectra portrayed in **Fig. 4-5**, R is obtainable as 0.228 at λ = 248 nm. Therefore, the value of A is calculated as 0.604 (= 1 - 0.168 - 0.228). Assuming no multiple refraction at the interface and no intensity loss through internal defects, the actual incident beam into the sample is presented as (1-R). Consequently, the actual transmittance (T / (1 - R) = 0.168 / 0.772) is calculated as 0.218. This value is convertible to an absorbance value as 0.662 (= -log 0.218). The average absorbance per TiO_2 layer was 0.055 (= 0.662 / 12) because six bilayers exist on both sides of substrate glass plate. For other thin films, the average absorbance per TiO_2 layer is calculable using reflectance and transmittance: 0.052 for the $(SiW_{12}/TiO_2)_6$ film, and 0.046 for $(H_2W_{12}/TiO_2)_n$. The TiO_2 suspension exhibits a Lambert-Beer relation [25]. Consequently, the molar extinction coefficient (ε) was obtainable from experimental data as 3.90×10^3 mol^{-1} dm^3 cm^{-1} at λ = 248 nm. Assuming the same ε on a TiO_2 particle in the thin film layer and 6 nm particle layer thickness (=TiO_2 particle diameter), the TiO_2 amount per unit layer can be estimated roughly from the Lambert-Beer equation ($A = \varepsilon b c$) as

$$0.055 = 3.90 \times 10^3 \times 6.0 \times 10^{-7} \times c$$

In that equation, c = 24 mol/dm^{-3}; it can be converted to 1.1×10^{-6} g cm^{-2}. Using the same method, 1.1 × 10^{-6} g cm^{-2} for $(SiW_{12}/TiO_2)_6$ and 0.94 × 10^{-6} g cm^{-2} for $(H_2W_{12}/TiO_2)_6$ are calculated.

The TiO_2 amount is calculable using the following equation if TiO_2 particles are packed by the closest packing in a 2D plane [25].

$$m = \frac{4}{3}\pi r^3 \rho / S_{UC}$$

$$S_{UC} = d^2 \sin 120^\circ$$

In those equations, d and r respectively represent the particle diameter and radius; ρ is the density of TiO_2 (for anatase, 3.89 g/cm^{-3}). In addition, S_{UC} is the unit cell area of the closest packing in 2D plane (**Fig. 4-15**). The m value is calculated as 1.41 × 10^{-6} g cm^{-2} when r = 3 nm. Comparing the estimated value between experimental data and theoretical particle packing, the film's packing density is estimated as 78% of the closest particle packing for $(PW_{12}/TiO_2)_6$ and $(SiW_{12}/TiO_2)_6$, and 66% for $(H_2W_{12}/TiO_2)_6$.

Figure 4-16 portrays IR spectra of the n = 15 bilayer hybrid films on a Si substrate and starting materials (PW_{12}, SiW_{12}, and H_2W_{12} ammonium salt) spectra measured using KBr method. Keggin-type polyanions exhibit characteristic absorbance of 700–1200 cm^{-1} [26]. If PW_{12} is hydrolyzed and a Keggin structure is decomposed, a P-O stretching peak (1080 cm^{-1}) and S-O stretching peak (930 cm^{-1}) are expected to split into two peaks [27]. The single 1080 cm^{-1} peak in the $(PW_{12}/TiO_2)_{15}$ film and 930 cm^{-1} peak in the $(SiW_{12}/TiO_2)_{15}$ film spectra indicate that the Keggin structure is retained in the film. In the $(H_2W_{12}/TiO_2)_{15}$ film IR spectra, W-O stretching and W-O-W bending peaks were observed, which indicated that H_2W_{12} deposition occurred and that the Keggin structure was maintained.

Our XPS measurements revealed differences of surface atomic ratios between

W(4d)/Ti(2d) on the $(XW_{12}/TiO_2)_2$+XW_{12} film and the $(XW_{12}/TiO_2)_3$ hybrid film. **Figure 4-17** shows the W/Ti mol ratio evaluated from XPS results. The surface chemical composition is evidence of alternative deposition. We can calculate the bulk W/Ti ratio in the film by assuming the following conditions: (1) the TiO_2 nanoparticle and XW_{12} anion are a 6 nm sphere (ρ_{TiO2}=3.89 g cm^{-3}) and 1 nm sphere (ρ_{PW12} = 9.12 g cm^{-3}, ρ_{SiW12} = 9.11 g cm^{-3}, and ρ_{H2W12} = 9.03 g cm^{-3}), as calculated from $\rho_{XW12} = (M_{XW12}/N_A)/[(4/3)\pi r^3]$, where N_A is Avogadro's constant); (2) the PW_{12} top layer has a two-dimensional closed packing hexagonal structure; (3) the second layer is filled completely with TiO_2; (4) electrons were emitted from the constant depth z; and (5) composition depends on the surface coverage ratio of TiO_2 and XW_{12}. Considering the size difference between TiO_2 and XW_{12}, this assumption is reasonable. Based on the assumptions described above, the surface coverage is represented as follows.

$$f_{XW12} = \frac{\pi r^2}{S_{UC}}$$

In those equations, f represents the surface coverage of XW_{12} and TiO_2 and r is the XW_{12} radius. Therefore,

$$W/Ti = \frac{f_{XW12} \times z \times \frac{\rho_{XW12}}{M_{XW12}} \times 12}{f_{TiO2} \times z \times \frac{\rho_{TiO2}}{M_{TiO2}}}.$$

The surface W/Ti ratio is calculated as 0.77 when PW_{12} is the top layer. This value is larger than the XRD result (0.31). On the other hand, the bulk composition using 2D closest packing model is 0.50 for PW_{12}/TiO_2 film. These calculation results indicate that the PW_{12} packing ratio is smaller than the closest packing. For other XW_{12}/TiO_2 films, the same consideration is possible. However, the depth-attributed XPS measurement is unclear. Characterization of the surface chemical composition and construction of appropriated calculation model are underway.

4.3.2. Reference films

Reference films were also prepared using LBL method. **Figure 4-18(a)** shows the dependence of UV-vis absorption spectra on the layer number of the $(PSS/TiO_2)_n$ hybrid films. Average increments of a TiO_2 layer and a PSS layer at λ = 228 nm were, respectively, 0.133 and 0.024. The packing density was estimated as 78% of the closest 2D packing density using absorbance and reflectance value at f = 248 nm (A = 0.808, R = 16.2% for 6-bilayer film). These values agree with those presented in a previous work [25]. **Figure 4-18(b)** presents the UV-vis absorption spectra of the $(PSS/TiO_2)_6$ hybrid film before and after UV illumination. The PSS layers were decomposed by the TiO_2 photocatalyst; the absorbance in the wavelength range of less than 300 nm decreased. This absorbance change was saturated after 2 h illumination. For this study, we therefore adopt this illumination time (2 h) for processing of the control $(TiO_2)_6$ film. **Figure 4-19(a)** portrays the dependence of UV-vis absorption spectra on the layer number of the $(PW_{12}/PDDA)_n$ hybrid films. Actually, PDDA only absorbed near 200 nm UV in this range, so the λ = 260 nm peak was attributed to PW_{12} absorption. **Figure 4-19(b)** shows UV-vis absorption spectra before and after UV illumination. After illumination, absorbance by PDDA (mainly λ < 250 nm) disappeared, probably because of PDDA decomposition by PW_{12} photocatalyst. The $(PW_{12})_6$ reference film was obtained. The slight increase of PW_{12} peaks is attributable to the difference of the supporting material [27]. **Figure 4-20** presents an optical micrograph of reference thin films on SiO_2 substrates. The $(TiO_2)_6$ film and $(PW_{12})_6$ film had transparency as high as that of $(XW_{12}/TiO_2)_6$ films.

Figure 4-21 portrays IR spectra of the n = 5 (PSS/TiO_2)$_n$ and (PW_{12}/PDDA)$_n$ thin films on a Si substrate before and after UV illumination. For (PSS/TiO_2)$_5$ thin film (**Fig. 4-21(a)**), C-H bendings attributable to aromatic ring (1127, 1008 cm^{-1}) and vibrations of R–SO_3^- peak (1036 cm^{-1}) were observed. They disappeared after illumination, and a SO_4^{2-} vibration peak appeared (1126, 1045 cm^{-1}) (**Fig. 4-21(b)**) [25], which indicated PSS polymer decomposition by UV-illumination. For (PW_{12}/PDDA)$_5$ thin film, a characteristic PW_{12} peak remained after assembly (**Fig. 4-21(c)**), which indicates that the Keggin structure was maintained after film preparation. After UV illumination, the C-N stretching (1106 cm^{-1}) peak was decreased and new peaks (1043, 955 cm^{-1}) appeared (**Fig. 4-21(d)**). These peaks can not be assigned. However, they might be assignable to PDDA decomposition species or a partly decomposed Keggin structure.

4.3.3. Surface morphology

The respective surface morphologies of the (PW_{12}/TiO_2)$_n$ and reference films were observed using Fe-SEM measurement. **Figure 4-22** shows SEM micrographs of the n = 2, 6 (PW_{12}/TiO_2) bilayer thin film surface. The substrate was covered with particles and many small cracks were observed on the coatings. No difference was observed from SEM images when the top surface was changed from TiO_2 to PW_{12}. **Figure 4-23** shows the reference thin film (n = 6) surface, with its many small cracks.

Figure 4-24 portrays the height profile of the (PW_{12}/TiO_2)$_2$ hybrid film. Each coating of this film was produced by displacing the coating position around 3 mm from the former coating. A curved baseline was attributed to the swelling of substrate. Two step structures were visible at distances of 700 μm and 3700 μm. Step heights at these positions are 6.5 nm and 6.9 nm; these values are almost equivalent to the sum of a TiO_2

particle (6 nm) and PW_{12} diameter (1.12 nm) [28]. This result clarifies that TiO_2 adsorption is likely to take place in a single layer. Some sharp peaks in the profile might be particles adsorbed onto the first layer. However, the radius of the diamond-tipped stylus (12.5 μm) is too large to measure gaps separating particles. Particle packing can not be discussed on the basis of these data. **Figure 4-25** presents the microstructures of $(XW_{12}/TiO_2)_1$, the first bilayers on the Si substrate. The Si surface was covered with TiO_2 particles even after washing. Most of the TiO_2 layer was of about 6–7 nm thickness. For all $(XW_{12}/TiO_2)_1$, single-particle adsorption was observed; they have smooth surfaces (Ra < 2 nm).

4.4 Conclusion

Using LBL method, Keggin-type polyacid and titania hybrid transparent thin films were prepared for this study. Both IR and UV-vis absorbance spectra indicated that alternative deposition occurred and that the XW_{12} Keggin structure was maintained after coating. The TiO_2 deposition amount decreased concomitantly with increased polyanion charge. The repulsion force between polyanions and the surface charge balance with TiO_2 affect these phenomena. Titania particles and PW_{12} reference thin films were also prepared using LBL method.

References

[1] Sayama, K.; Mukasa, K.; Abe, R.; Arakawa, H. *Chem. Commun*., (23), 2416-2417 (2001).

[2] Kato, H.; Hori, M.; Konta, R.; Shimodaira, Y.; Kubo, A. *Chem. Lett*., **33**, 1348-1349 (2001).

[3] Tada, H.; Mitsui, T.; Kiyonaga, T.; Akita, T.; Tanaka, K. *Nature Mater*., **5**, 782-786 (2006).

[4] Park, H.; Choi, W. *J. Phys. Chem. B*, **107**, 3885-3890 (2003).

[5] Yoon, M.; Chang, J. A.; Kim, Y.; Choi, J. R.; Kim, K.; Lee, S. J. *J. Phys. Chem. B,* **105**, 2539-2545 (2001).

[6] Tachikawa, T.; Tojo, S.; Fujitsuka, M.; Majima, T. *Chem. Eur. J.* **12**, 3124-3131 (2006).

[7] Weinstock, I. A. *Chem. Rev*., **98**, 113-170 (1998).

[8] Nosaka, Y.; Nosaka, A., *Nyuumonhikarishokubai*; Tokyo Tosho Co., Ltd.: Tokyo (2004) in Japanese.

[9] Iler, R. K. *J. Colloid Interface Sci*., **21**, 569-594 (1966).

[10] Decher, G. *Science,* **277**, 1232-1237 (1997).

[11] Bertrand, P.; Jonas, A.; Laschewsky, A.; Legras, R. *Macromol. Rapid Commun.* **21**, 319-348 (2000).

[12] Kotov, N. A.; Dékány, I.; Fendler, J. H. *J. Phys. Chem*, **99**, 13065-13069 (1995).

[13] Schmitt, J.; Decher, G.; Dressick, W. J.; Brandow, S. L.; Geer, R. E.; Shashidhar, R.; Calvert, J. M. *Adv. Mater*., **9(**1), 61-65 (1997).

[14] Sasaki, T. *J. Ceram. Soc. Jpn*., **115**(1), 9-16 (2007).

[15] Keller, S. W; Kim, H.-N.; Mallouk, T. K. *J. Am. Chem. Soc*., **116**, 8817-8818 (1994).

[16] Quinn, J. F.; Johnston, A. P. R.; Such, G. K.; Zelikin, A. N.; Caruso, F. *Chem. Soc. Rev*., **36**, 717-718 (2007).

[17] Sato, M.; Sano, M. *Langmuir,* **21**, 11490-11494 (2005).

[18] Borrás-Almenar, J. J.; Coronado, E.; Müller, A.; Pope, M. *Polyoxometalate Molecular Science*; Kluwer Academic Publishers: Dordrecht / Boston / London, 441-466 (2003).

[19] Liu, S.; Kurth, D. G.; Bredenkötter, B.; Volkmer, D., *J. Am. Chem. Soc*., **124**, 12279-12287 (2002).

[20] Wang, B.; Vyas, R. N.; Shaik, S. *Langmuir*, **23**, 11120-11126 (2007).

[21] Kepert, D. L.; Kyle, J. H. *J.C.S. Dalton*, 1781-1784 (1978).

[22] Wang, Z.-S.; Li, F.-Y.; Huang, C.-H.; Wang, L.; Wei, M.; Jin, L.-P.; Li, N.-Q. *J. Phys. Chem. B*, **104**, 9676-9682 (2000).

[23] Sasaki, T.; Ebina, Y.; Tanaka, T.; Harada, M.; Watanabe, M. *Chem. Mater*., **13**, 4661-4667 (2001).

[24] Fournier, M.; Thouvenot, R.; Rocchiccioli-Deltcheff, C. *J. Chem. Soc. Faraday Trans*., **87**(2), 349-356 (1991).

[25] Wang, Z-S.; Sasaki, T.; Muramatsu, M.; Ebina, Y.; Tanaka, T.; Wang. L.; Watanabe, M. *Chem. Mater*., **15**, 807-812 (2003).

[26] Rocchiccioli-Deltcheff, C.; Thouvenot, R.; Frank, R. *Spectrochim. Acta A*, **32**A, 587-597 (1976) in French.

[27] Edward, J.; Thiel, C. Y.; Benac, B.; Knifton, J. F. *Catal. Lett*., **51**(1-2), 77-83 (1998).

[28] Kurucseav, T.; Sargesoan, M.; West, B. O. *J. Phys. Chem*., **61**(11), 1567-1569 (1957).

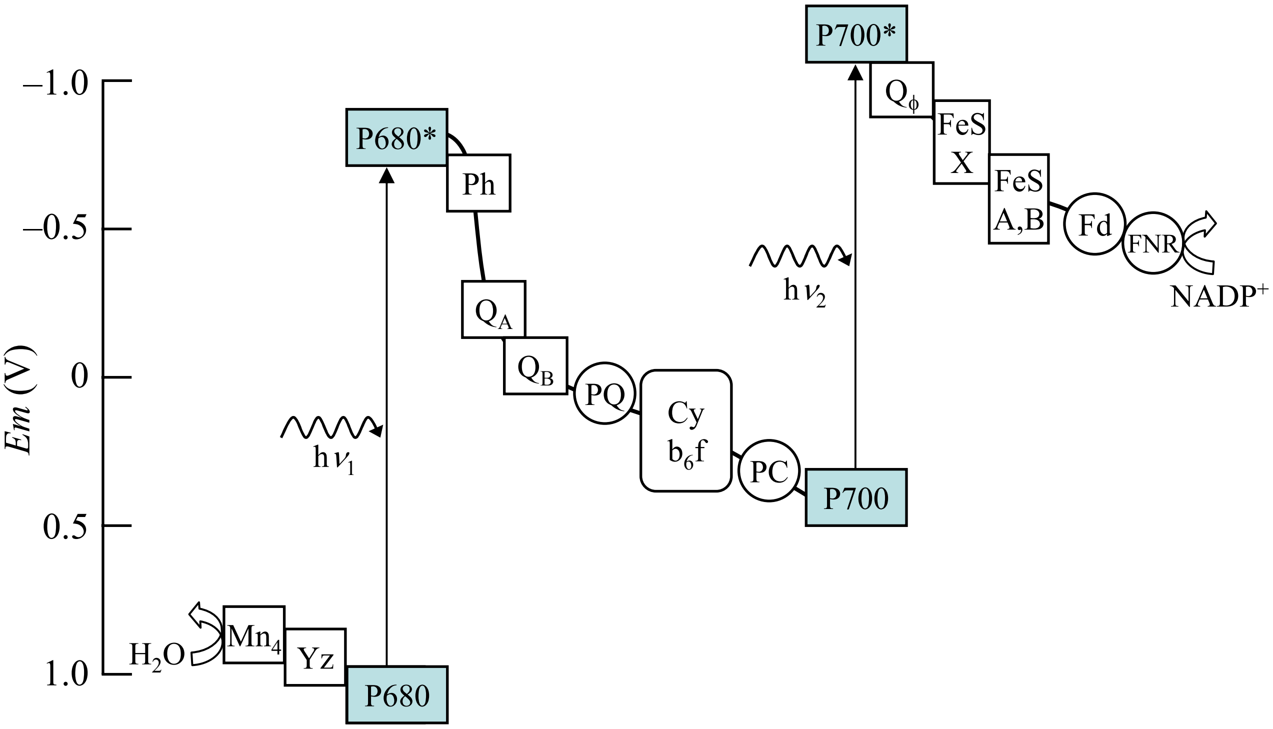

Figure 4-1. Energy diagram of plant photosynthesis: Mn4, Mn cluster; Yz, tyrosine residue; PQ, plastquinone; QX, quinone derivative; Ph, pheophytin; Cy b6f, cytochrome b6f complex; PC, plastcyanine; Fd, ferredoxin; FNR, ferredoxin-NADP$^+$ reductase.

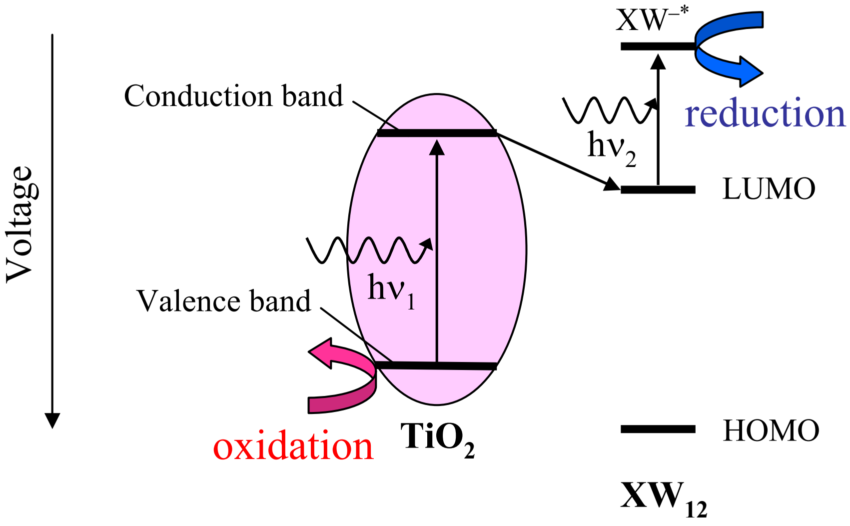

Figure 4-2. Energy diagram of TiO_2 and Keggin type HPA and IPA.

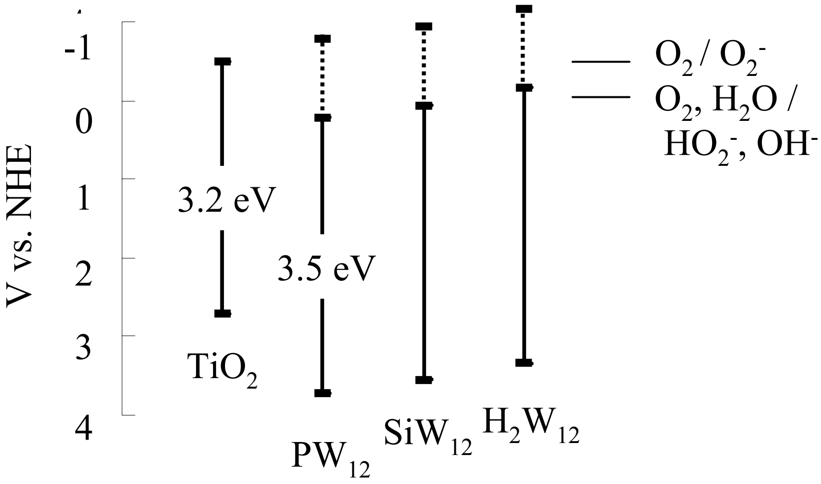

Figure 4-3. Energy diagram of TiO_2 and Keggin type HPA and IPA.

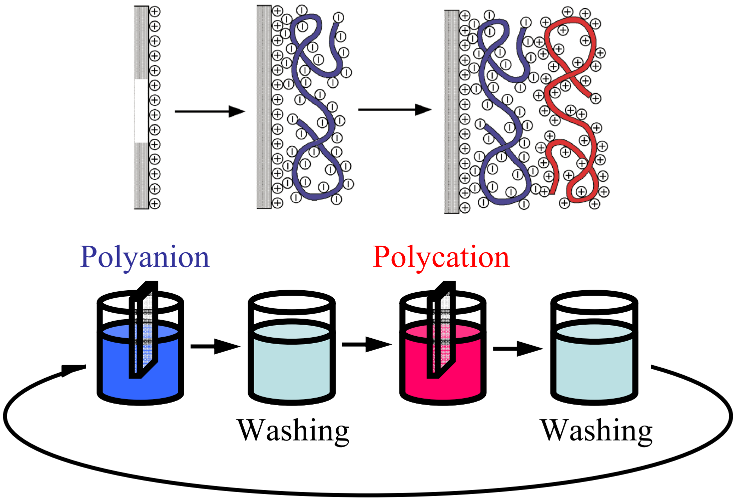

Figure 4-4. Schematic illustration of LBL method [10].

Figure 4-5. Experimental procedure of $(XW_{12}/TiO_2)_n$ thin film preparation using LBL method.

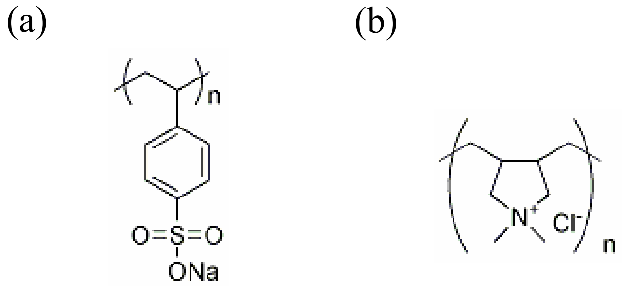

Figure 4-6. Polyelectrolyte structures used for reference film preparation: (a) PSS, (b) PDDA.

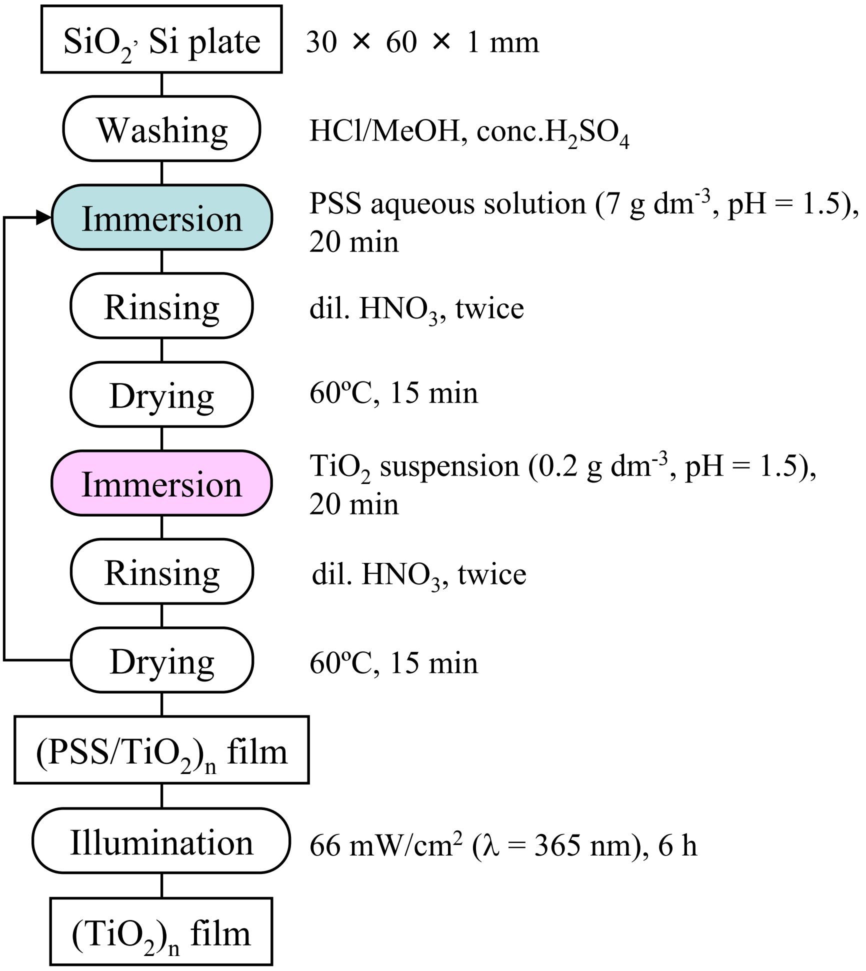

Figure 4-7. Experimental procedure of $(TiO_2)_n$ thin film preparation using LBL method.

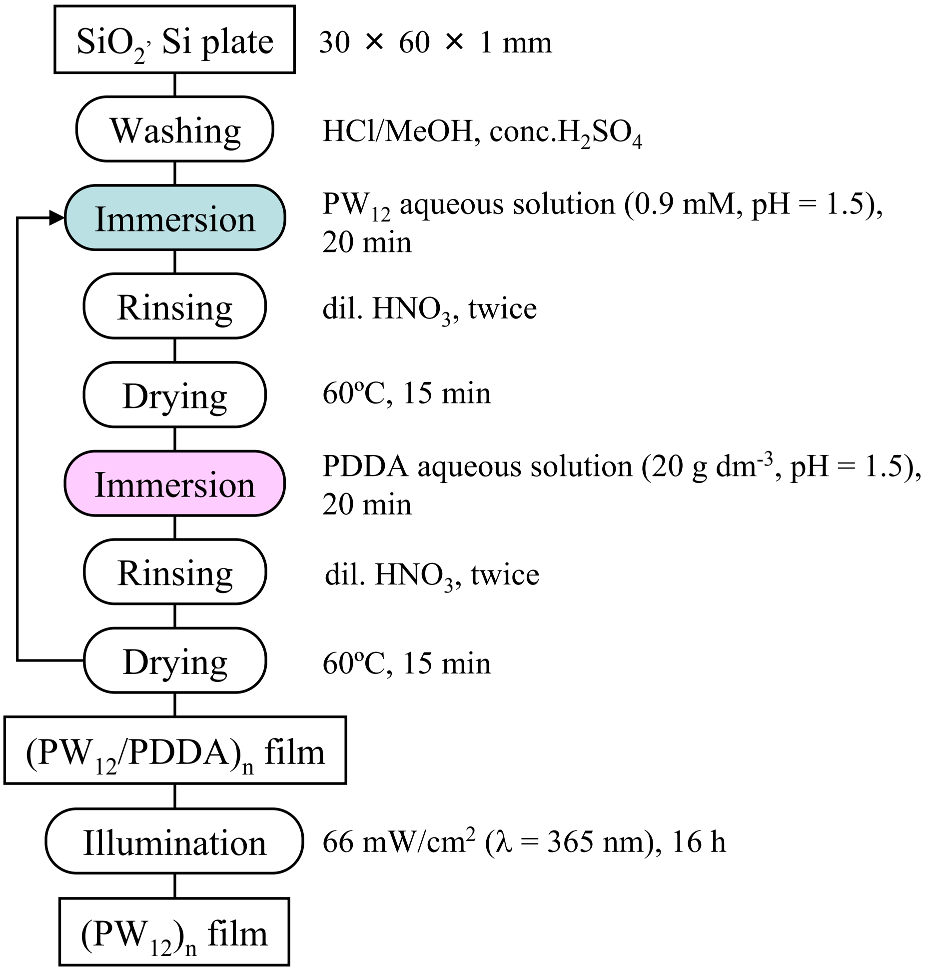

Figure 4-8. Experimental procedure of (PW$_{12}$)$_n$ reference thin film preparation using LBL method.

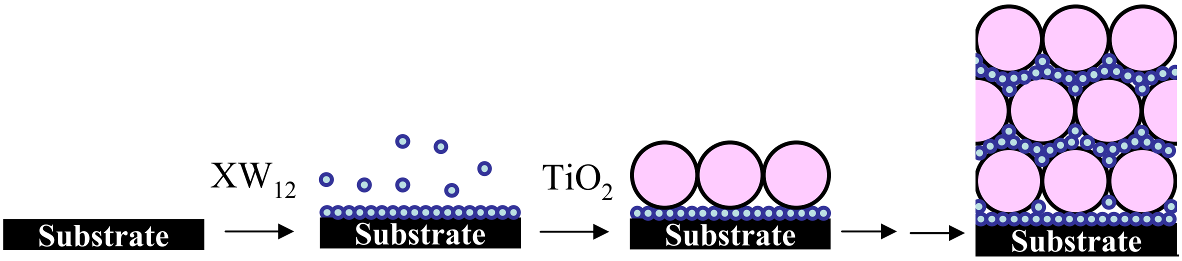

Figure 4-9. Schematic illustration of self-assembly XW_{12}/TiO_2 film preparation.

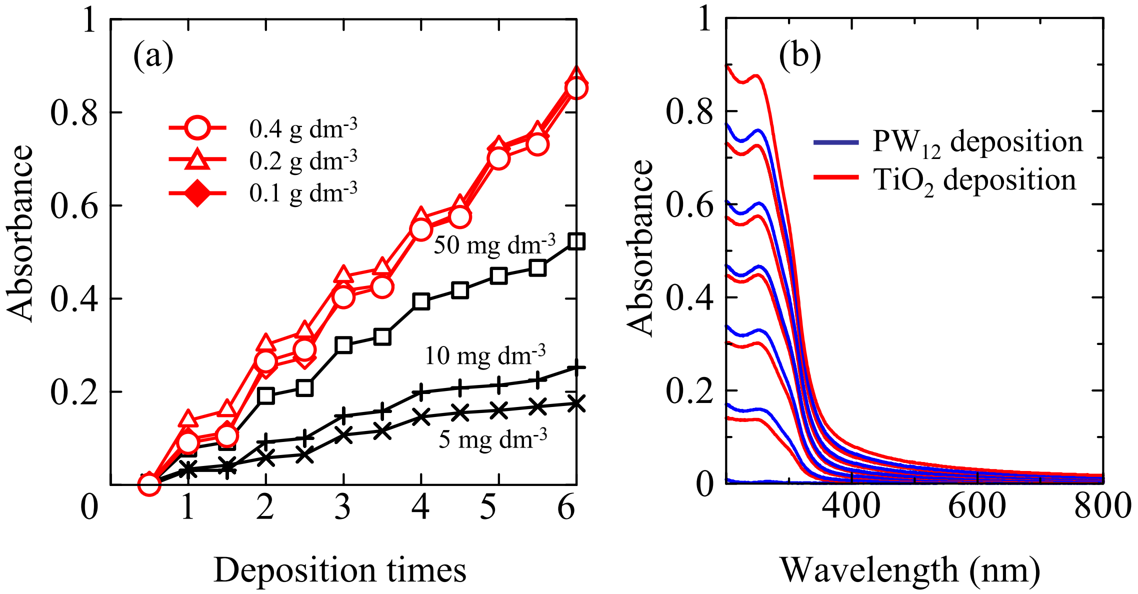

Figure 4-10. UV-vis absorbance spectra change of the $(PW_{12}/TiO_2)_n$ self-assembly layer. (a) UV absorbance change at l = 248 nm when TiO_2 suspension concentration was changed. (b) Layer growth with deposition times. Particle concentration is 0.2 g dm^{-3}; the deposition time is 20 min.

Table 4-1. Absorbance change of the $(SiW_{12}/TiO_2)_n$ thin films

SiW_{12} concentration (mM)	Absorbance per bilayer (248 nm)		
	0.2 g dm^{-3} TiO_2	0.4 g dm^{-3} TiO_2	0.8 g dm^{-3} TiO_2
0.9	0.084	0.107	peeling
1.8	0.123	0.124	0.128
2.7	0.124	0.135	0.136
3.6	—	0.138	—

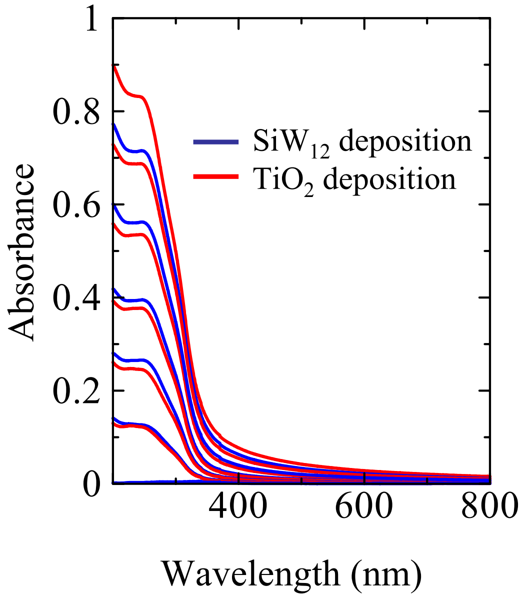

Figure 4-11. UV–vis absorbance spectra change of the $(SiW_{12}/TiO_2)_n$ self-assembly layer. The TiO_2 particle concentration is 0.2 g dm^{-3}; and the deposition time is 20 min.

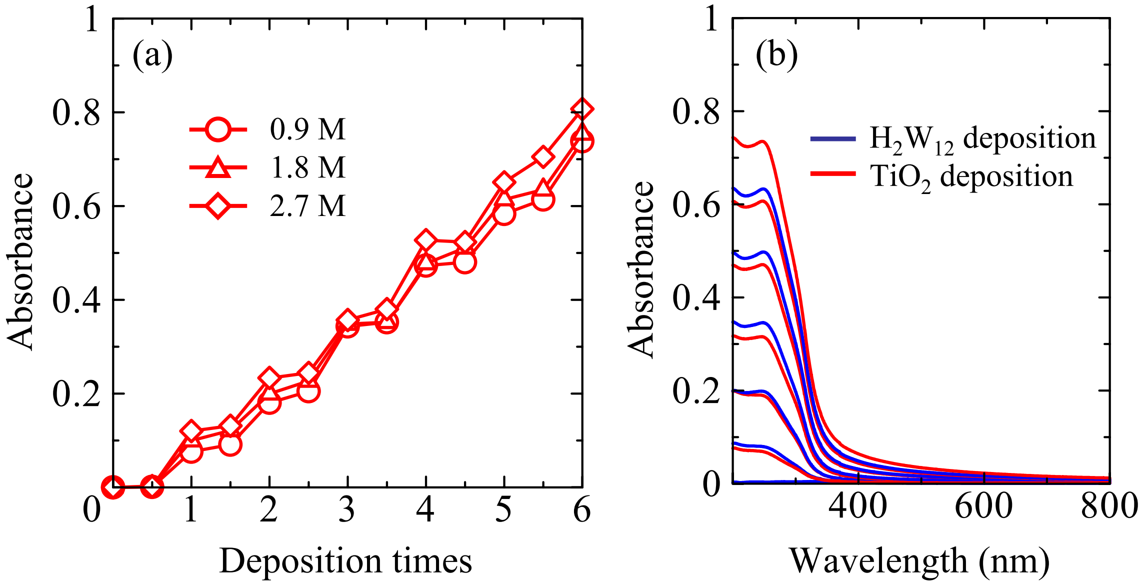

Figure 4-12. UV–vis absorbance spectra change of the $(H_2W_{12}/TiO_2)_n$ self-assembly layer. (a) UV absorbance change at l = 248 nm when H_2W_{12} ammonium salt concentration was changed. (b) Layer growth with deposition times. The TiO_2 particle concentration is 0.2 g dm^{-3}; the deposition time is 20 min.

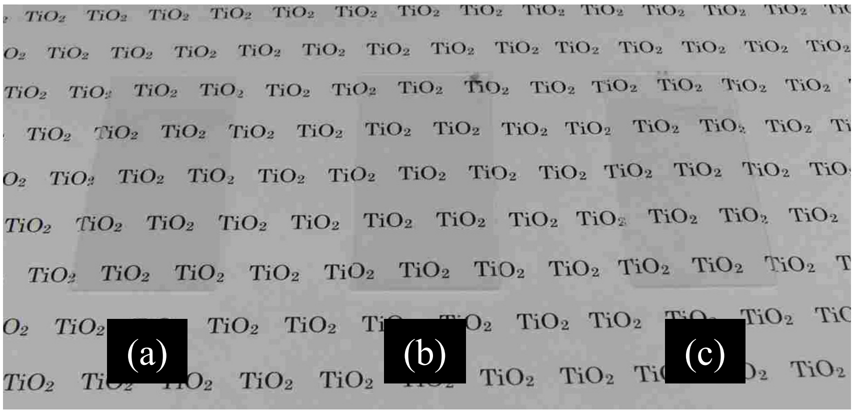

Figure 4-13. An Optical micrograph of hybrid $(XW_{12}/TiO_2)_6$ hybrid thin films on SiO_2 substrates. (a) $(PW_{12}/TiO_2)_6$, (b) $(SiW_{12}/TiO_2)_6$, (c) $(H_2W_{12}/TiO_2)_6$.

Table 4-2. Thin film absorbance change at 248 nm

	Anion charge	Absorbance per XW_{12} deposition	Absorbance per TiO_2 deposition	Absorbance per bilayer deposition
PW_{12}/TiO_2	3–	0.026	0.129	0.155
SiW_{12}/TiO_2	4–	0.017	0.121	0.138
H_2W_{12}/TiO_2	6–	0.016	0.111	0.127

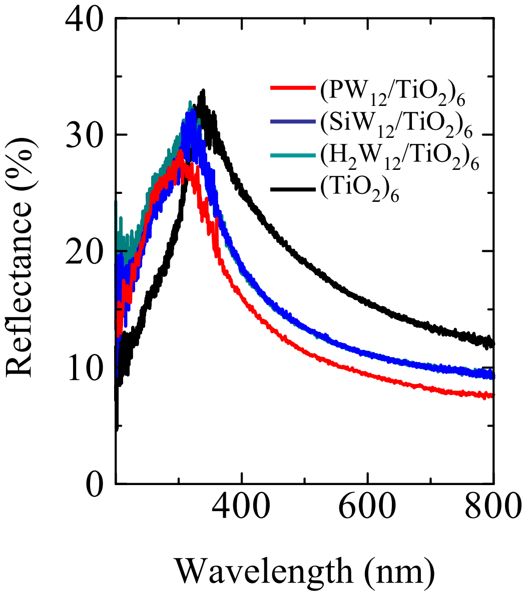

Figure 4-14. UV-vis reflectance spectra of hybrid thin films and reference $(TiO_2)_6$ film.

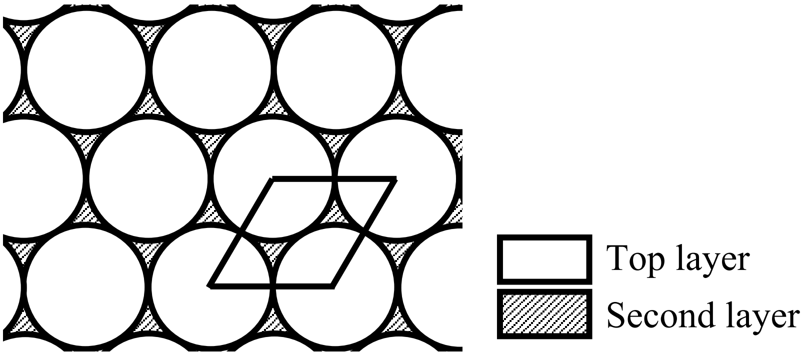

Figure 4-15. Schematic illustration of the closest 2D packing.

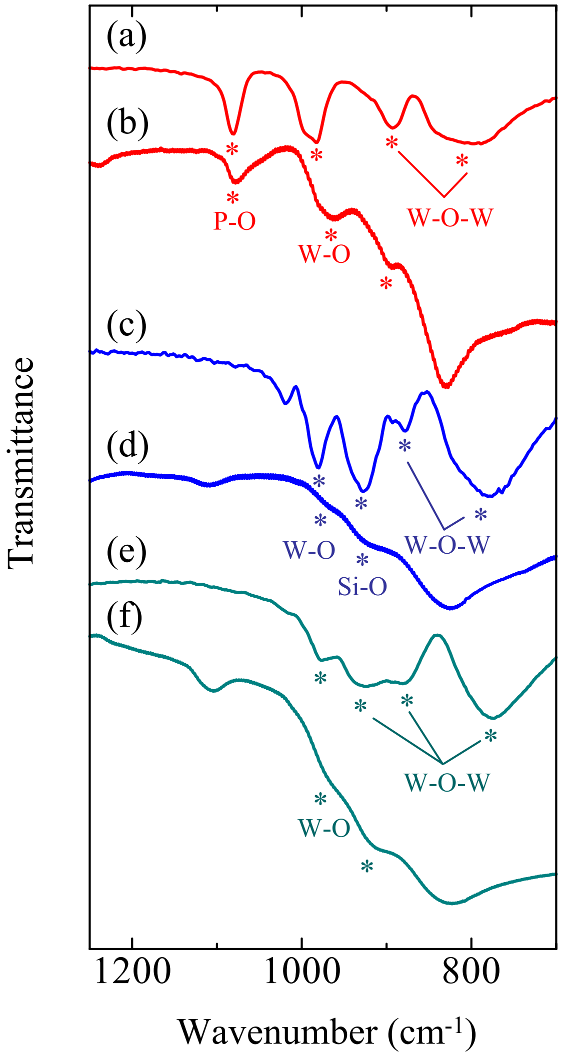

Figure 4-16. FT-IR spectra of starting material and 15-bilayer hybrid thin films. Asterisks present characteristic Keggin ion peaks:

(a) PW_{12}(KBr method), (b) $(PW_{12}/TiO_2)_{15}$, (c) SiW_{12} (KBr method), (d) $(SiW_{12}/TiO_2)_{15}$, (e) HW_{12} ammonium salt (KBr method), and $(H_2W_{12}/TiO_2)_{15}$.

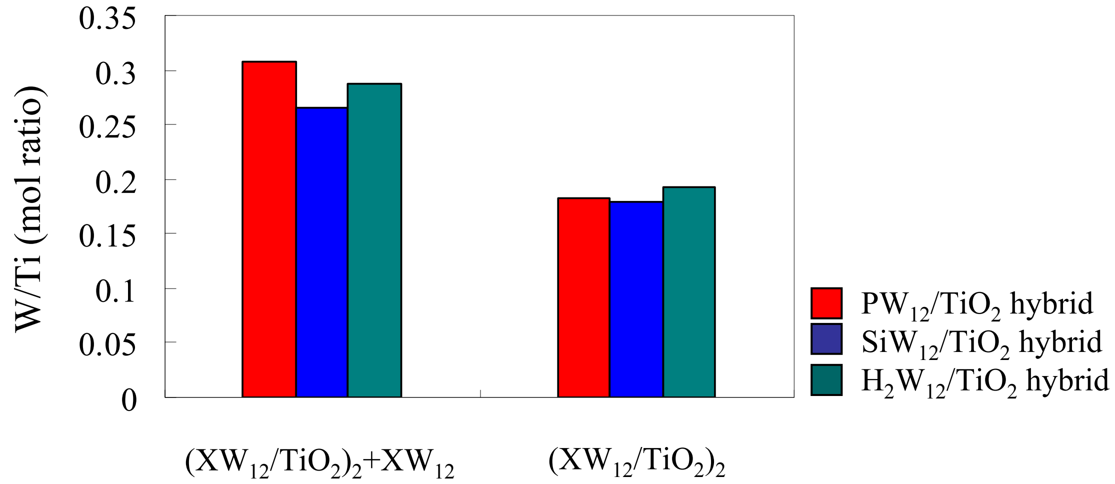

Figure 4-17. Surface chemical composition evaluated by XPS result.

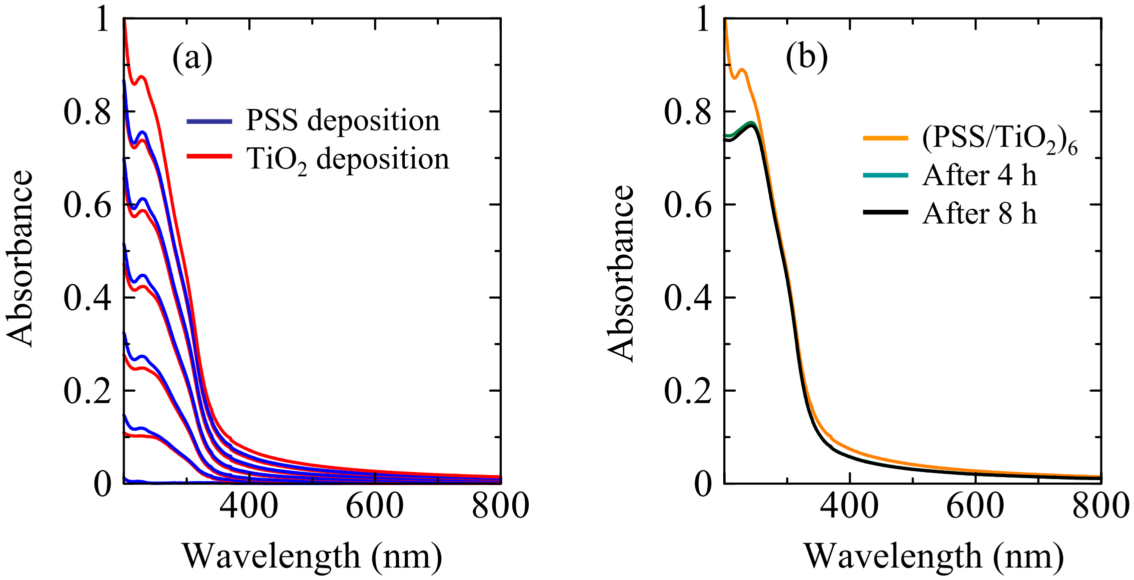

Figure 4-18. UV-vis absorbance spectra change of the $(PSS/TiO_2)_n$ self-assembly layer. (a) UV-vis absorbance growth with deposition times. (b) UV-vis absorbance change before and after illumination.

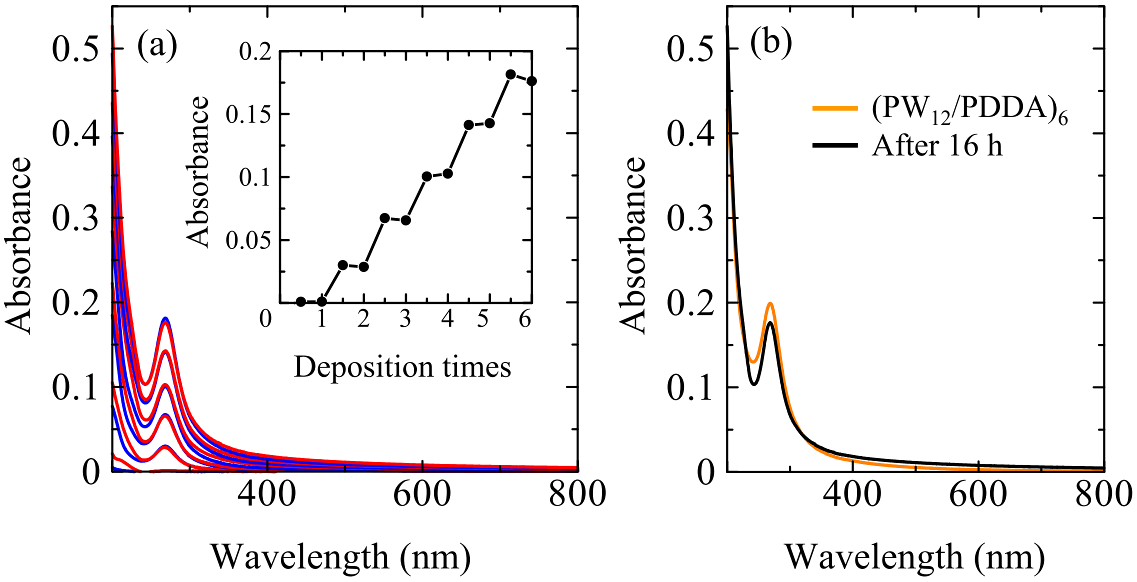

Figure 4-19. UV-vis absorbance spectra change of the $(PW_{12}/PDDA)_n$ self-assembly layer. (a) UV-vis absorbance growth with deposition times, (b) UV-vis absorbance change before and after illumination.

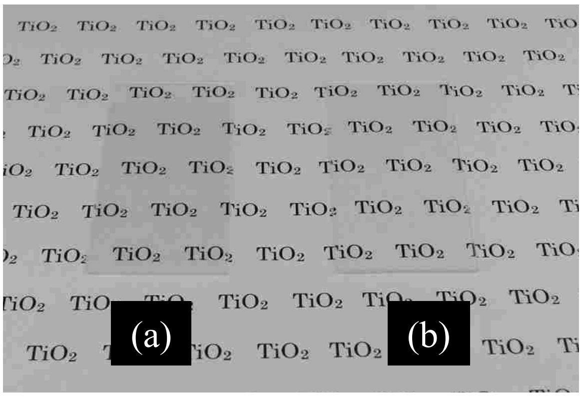

Figure 4-20. Optical micrograph of reference thin films. (a) $(TiO_2)_6$, (b) $(PW_{12})_6$.

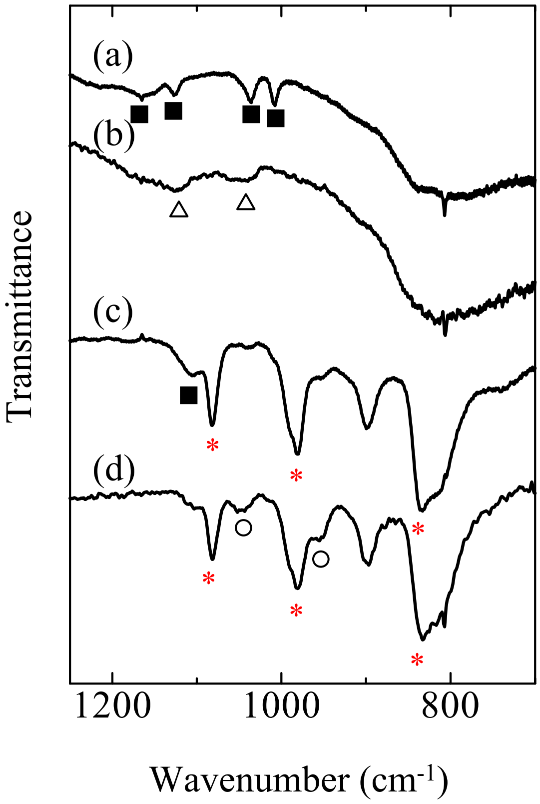

Figure 4-21. IR spectra of the n = 5 $(PSS/TiO_2)_n$ and $(PW_{12}/PDDA)_n$ thin films on a Si substrate before and after UV illumination. (a) $(PSS/TiO_2)_5$, (b) $(TiO_2)_5$ prepared from $(PSS/TiO_2)_5$ using UV illumination, (c) $(PW_{12}/PDDA)_5$, (d) $(PW_{12})_5$ prepared from $(PW_{12}/PDDA)_5$ using illumination. IR peaks were assigned the following: ■, organic polymers; △, SO_4^{2-}; *, PW_{12}; ○, unknown product or decomposed PW_{12}.

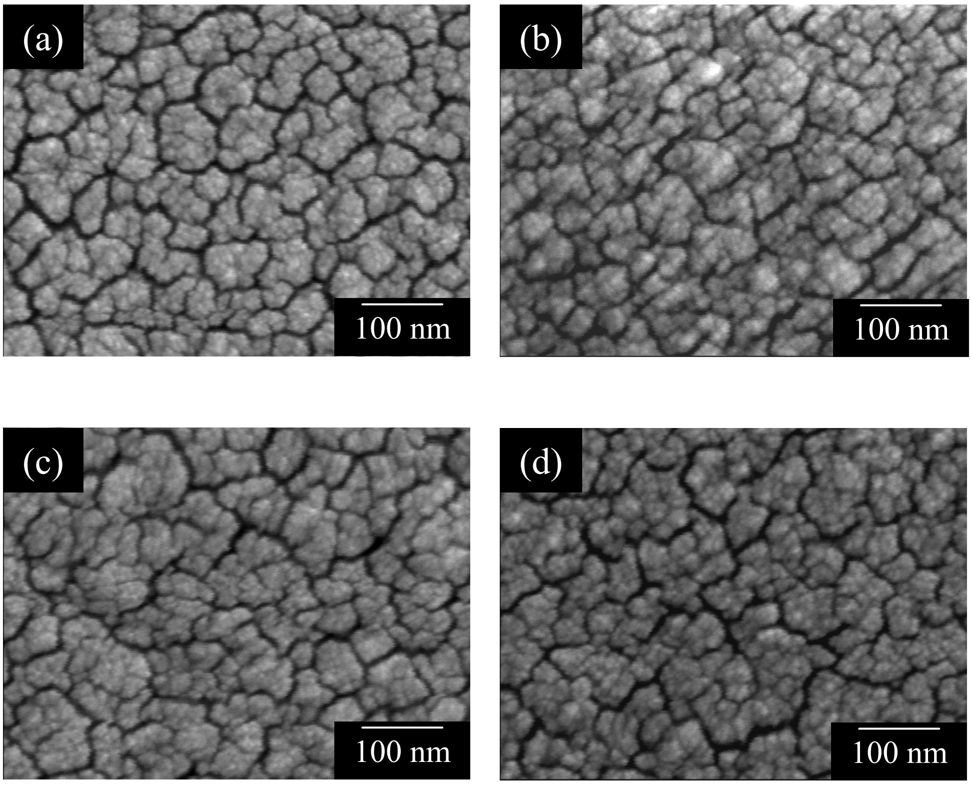

Figure 4-22. SEM images of the *n* = 2, 6 (PW_{12}/TiO_2) thin film surface on Si plate. (a) *n* = 2 sample, top layer; TiO_2, (b) *n* = 2 sample, top layer; PW_{12}, (c) *n* = 6 sample, top layer; TiO_2, (b) *n* = 6 sample, top layer; PW_{12}.

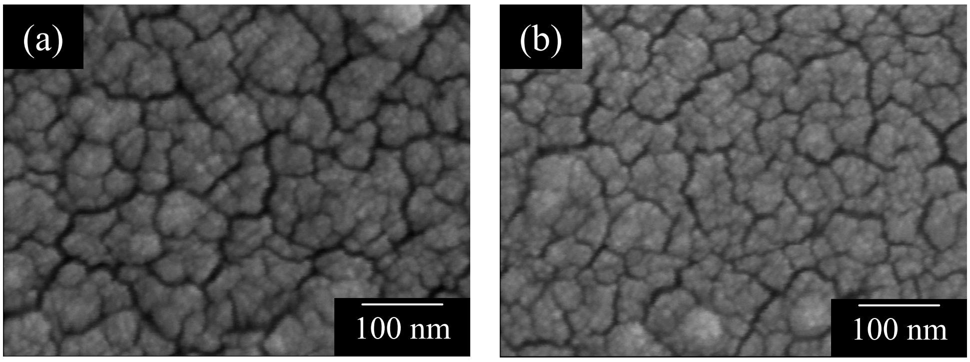

Figure 4-23. SEM images for *n* = 6 organic polymer and TiO_2 hybrid LBL films on Si plate. (a) *n* = 6 sample, top layer; TiO_2, (b) *n* = 6 sample, top layer; PDDA.

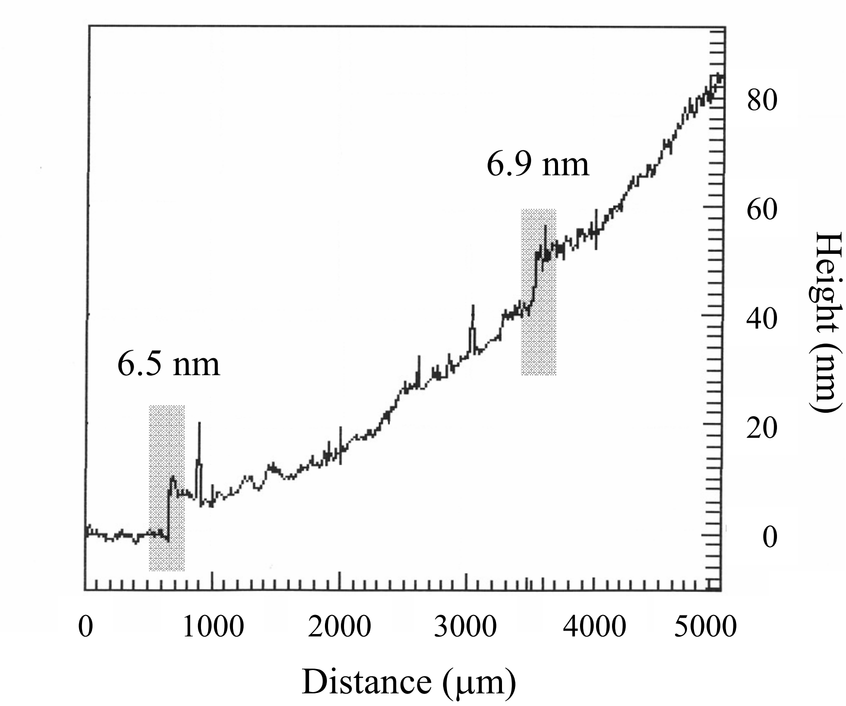

Figure 4-24. 2D-height profile of the $(PW_{12}/TiO_2)_2$ hybrid film.

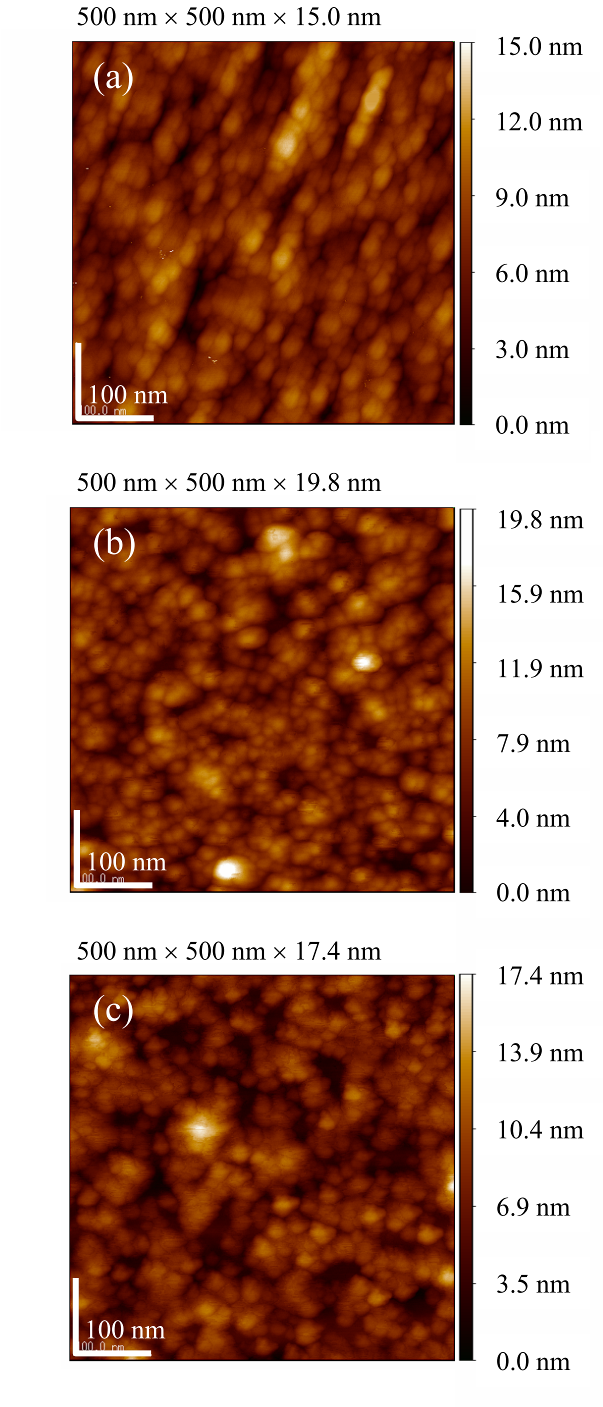

Figure 4-25. AFM image of $(XW_{12}/TiO_2)_1$ films on the Si substrate: (a) $(PW_{12}/TiO_2)_{1,}$ (b) $(SiW_{12}/TiO_2)_1$, (c) $(H_2W_{12}/TiO_2)_1$.

CHAPTER 5

Photocatalytic Activity of Keggin-type Polyacid and TiO_2 Hybrid thin Films

5.1. Introduction

5.1.1. Reoxidation of reduced Keggin-type polyacid

In the XW_{12}-TiO_2 hybrid system, XW_{12} anion is expected to act as a reduction site. The redox cycle of polyacids was introduced comprehensively in **Chapter 3**. Herein, we specifically address the reoxidation process of the reduced polyacids because the electron consumption rate of XW_{12} probably affects the overall photocatalytic performance of XW_{12}-TiO_2 hybrids.

In a homogeneous reaction, O_2 is considered an electron acceptor for a reduced XW_{12} anion if the system includes no other electron acceptor [1, 2]. Papaconstantinou and Akid et al. investigated the reoxidation rate of the one-electron-reduced Keggin ion ($[XW_{12}O_{40}]^{(n+1)-}$) using microsecond flash photolysis [3, 4] in an aqueous solution containing Keggin ion, 2-propanol, and O_2 at pH = 1. The reaction was of first-order in $[(XW_{12}O_{40})^{(n+1)-}]$, $[H^+]$, and $[O_2]$. The first-order dependence of the rate on $[H^+]$ suggested that HO_2, rather than $O_2^-\cdot$, was involved in the rate-controlling step. Those results suggest the following reaction:

$$[XW_{12}O_{40}]^{(n+1)-} + O_2 + H^+ \rightarrow [XW_{12}O_{40}]^{n-} + HO_2\cdot$$

The reaction rate was presented as

$$\frac{-d[(XW_{12}O_{40})^{(n+1)-}]}{dt} = k[(XW_{12}O_{40})^{(n+1)-}][H^+][O_2]\,.$$

The XW_{12} anion reduction potentials (E) and termolecular rate constants (k) for the reduction of O_2 measured at constant O_2 and H^+ concentrations are presented in **Table 5-1**.

The reaction rate of $[XW_{12}O_{40}]^{(n+1)-}$ with O_2 depends on the kind of XW_{12}, especially for PW_{12}; the reoxidation is endothermic and its reaction rate is less than that of SiW_{12} or H_2W_{12}.

5.1.2. Objective

In Chapter 4, we described preparation of Keggin-type HPA and IPA / TiO_2 hybrid thin films using LBL method. These polyacids have identical structure; however, they have different acid strengths, redox levels, and relativities with O_2 [5] (**Fig. 5-1**). These properties must affect the hybrid films' oxidation and reduction rate. Consequently, the total decomposition performance depends on hybridized Keggin-type polyacids. In this chapter, we describe the photocatalytic activities of the hybrid thin films and reference thin films. Wavelength dependence of the photocatalytic activities were investigated for discussing reactions and electron transportation in the hybrid films.

5.2. Experimental procedure

5.2.1. Preparation of 2-propanol standard gas

Photocatalytic activity was evaluated according to the decomposition of gaseous 2-propanol. Reagent grade 2-propanol (purity: 99.5%; Wako Pure Chemical Industries Ltd., Tokyo, Japan) was used. For preparation of 2-propanol standard gas, 2 ml liquid 2-propanol was injected into a 1 L glass bottle filled with ambient air. The bottle was sealed tightly; then kept in dark under constant temperature (20°C) for 24 h. Then a liquid-vapor equilibrium condition was obtained and 2-propanol concentration in the bottle was evaluated using the following equation:

$$C = \frac{P_{2-propanol}(T)}{P_{atm} + P_{2-propanol}(T)},$$

where C is the concentration of 2-propanol, P_{atm} is atmospheric pressure, and $P_{\text{2-propanol}}(T)$ is the saturated vapor pressure of 2-propanol.

5.2.2. Estimation of photocatalytic activity for the $(XW_{12}/TiO_2)_n$ films

The $(XW_{12}/TiO_2)_n$ films and the $(TiO_2)_n$ reference films (n = 2 or 6) on a glass substrate were used in this experiment. The experimental procedure is presented in Fig. 5-**1**. Before experiments, eight sample films were exposed to strong UV light (224 mW/cm^2, 365 nm) to remove organic compounds that had adsorbed onto the surface. A Pyrex glass vessel (500 mL volume) with a quartz glass lid was used as a batch reactor (**Fig. 5-2**). A sample film was set at the center of the vessel; then the atmosphere in the reactor was replaced by gas flow (1.0 L/min, 10 min) with air at 20°C and 80% relative humidity. Subsequently, the vessel was sealed; then 2-propanol gas was injected into it. The injected gas amount was equivalent to that for 50 ppm concentration. The vessel was then stored in the dark. During this dark storage, the 2-propanol concentration decreased because of the molecules' adsorption onto the sample and the vessel surface. The concentration change was monitored using a gas chromatograph (GC-14A; Shimadzu Corp., Tokyo, Japan) equipped with a flame ionization detector (FID), a methanizer, and a Sunpak-A column (Shimadzu Corp.). The carrier gas was nitrogen; the respective temperatures for the detector and injection port were 230 and 200°C. The initial column temperature was 50°C, which was maintained for 2.5 min. The temperature was increased 20°C /min to 130°C to peak separation. A related temperature diagram is presented in Fig. 5-**3**. After adsorption, the equilibrium was confirmed. Then UV illumination was carried out using a UV illuminator (LA-410UV-1; Hayashi Watch Works. Japan) equipped with a Hg-Xe lamp (MX4010). This light source includes several peaks in the 280–450 nm range, with the strongest peak at 365 nm (**Fig. 5-4**). The illumination intensity at the sample surface was 1 mW/cm^2 at 365 nm. The 2-propanol, acetone, and CO_2 concentrations were evaluated every 30 min for 4 h.

Two colored glass filters, UV-33 (absorbed UV < 330 nm, Asahi Glass Co. Ltd., Japan) and UV-D33S (absorbed visible light > 400 nm, Asahi Glass) were used to limit the light illumination wavelength range. In both the UV-limited and vis-limited cases, the illumination intensity was 1 mW/cm^2 at 365 nm. Other experimental conditions were identical to those of the all-light illumination cases.

5.2.3. Estimation of photocatalytic activities for the $(PW_{12}/TiO_2)_n$ and reference films

Top surface effects on photocatalytic activity were investigated using $(PW_{12}/TiO_2)_n$ films, $(PW_{12}/TiO_2)_n$+PW_{12} films (top was covered with a PW_{12} layer), $(TiO_2)_n$ films, and $(PW_{12})_n$ films (n = 2 or 6) on a glass substrate. The sample films were exposed to strong UV light (224 mW/cm^2, 365 nm) before experiments and then put in a Pyrex glass vessel (500 mL volume) with a quartz glass lid. Subsequently, the vessel was sealed, and 2-propanol gas was injected into it. The atmosphere in the glass reactor was not replaced in these experiments. The injected gas amount was equivalent to that for 50 ppm concentration. The vessel was then stored in the dark. The concentration change was monitored using gas chromatography. After adsorption, the equilibrium was confirmed, and UV illumination was carried out. The illumination intensity at the sample surface was 1 mW/cm^2 at 365 nm. The 2-propanol, acetone, and CO_2 concentrations were evaluated every 30 min during 4 h. Two colored glass filters, UV-33 and UV-D33S, were used to limit the range of wavelengths of the light illumination. In both the UV-limited and vis-limited cases, the illumination intensity was 1 mW/cm^2 at 365 nm. Other experimental conditions were identical to those of the all-light illumination cases.

5.3. Results and discussion

5.3.1. Photocatalytic activities of the $(XW_{12}/TiO_2)_n$ and $(TiO_2)_n$ films

5.3.1.1. Photocatalytic activities under UV-vis illumination

Both TiO_2 and XW_{12} can decompose 2-propanol through photocatalytic reaction. The decomposition pathway of this reaction has been studied extensively [6–8]. Molecules of gaseous 2-propanol are initially decomposed into acetone and are ultimately decomposed to H_2O and CO_2. The decomposition rate of acetone by TiO_2 photocatalyst is much lower than that of 2-propanol because of displacement of water vapor from the TiO_2 surface [9] and the reaction rate difference against the ·OH radical [10].

Figure 5-5 presents averages, for three experiments, of the 2-propanol initial concentration (C_0) after dark storage (2.5 h). Blank tests revealed that most of the 2-propanol that disappeared during dark storage was adsorbed onto the glass cell. However, the $(XW_{12}/TiO_2)_2$ hybrid films tend to show lower C_0 than $(TiO_2)_2$ film (photodecomposed $(PSS/TiO_2)_2$ film). Results show that the adsorption capability was increased by hybridization with XW_{12}. Comparing the two-bilayer and six-bilayer results, six-bilayer films exhibited lower adsorption capabilities than two-bilayer films did, despite their greater thickness. Actually, the 2-propanol adsorption amount is expected to be affected by the surface area, surface water layer, and hydration water of XW_{12} [11]. Under the experimental condition (20°C, r.h. 80%), the 2-propanol adsorption amount was not increased with layer thickness.

Figure 5-6 and **Figure 5-7** respectively portray the concentration changes of 2-propanol and acetone during all-light illumination for $(XW_{12}/TiO_2)_n$ hybrid films and $(TiO_2)_n$ films (n = 2, 6). No color filter was used along with the Hg-Xe lamp. Therefore, incident light contained both UV and visible light. In those figures, C_0 represents the initial concentration after 2.5 h of dark storage in the case of 2-propanol. For acetone, $C/C_0 = 1$ was defined as the initial concentration of 2-propanol. In two-bilayer samples, the $(H_2W_{12}/TiO_2)_2$ film and $(PW_{12}/TiO_2)_2$ film exhibited a higher initial decomposition rate (17 and 14 ppm/h) than $(TiO_2)_2$ film (11 ppm/h). These values were calculated using 2-propanol concentration change during the first 30 min. The $(H_2W_{12}/TiO_2)_2$ film shows a high decomposition rate despite the smaller deposition amount of TiO_2 than other hybrid thin films (**Table 4-2**). Decomposition rates were increased from those of two-bilayer films in all samples when n = 6 samples were used (**Fig. 5-7(a)**). **Figure 5-8** presents a summary of the initial decomposition rate of 2-propanol for n = 2 and 6 samples. Six-bilayer samples exhibited 2.5–3.4 times higher rates than those of the two-bilayer samples. Results show that not only sample surface but also the bulk part participated in the decomposition for both hybrids and TiO_2 references.

Those results revealed that $(H_2W_{12}/TiO_2)_n$ films are effective for decomposition of 2-propanol. However for acetone decomposition, we must note that the reproducibility of acetone concentration during decomposition was lower than that of the 2-propanol. An almost equal rate was obtained for 2-propanol decomposition, when the decomposition experiment was carried out repeatedly. However, for acetone, the rate depended on time. For acetone decomposition, H_2W_{12} sample does not always show the highest decomposition rate. Acetone generation, adsorption and the decomposition rate can affect the apparent acetone concentration. Furthermore, acetone decomposition is a multistep reaction: intermediates are undetectable by GC. For that reason, the acetone decomposition is difficult to discuss using concentration data alone. Direct decomposition experiments of acetone are necessary to reveal the acetone decomposition performance. Those studies are now underway.

5.3.1.2. Visible light effect on decomposition

Figures 5-9 and **5-10** respectively depict the 2-propanol and acetone concentration change during UV illumination without $\lambda > 400$ nm visible light. Under such a condition, 2nd step photoexcitation ($[XW_{12}O_{40}]^{(n+1)-}$ photoexcitation by visible light) only slightly occurred; the Z-scheme does not work. The electrons trapped in the XW_{12} LUMO level reduce O_2 **(Fig. 5-11)**. For the two-bilayer samples, the decomposition rate was slightly decreased from that of all-light illumination case. However, the six-bilayer sample shows a different tendency. **Figure 5-12** portrays the initial 2-propanol decomposition rates without visible light illumination. These rates were normalized by each sample's decomposition rate under all-light illumination. The $(PW_{12}/TiO_2)_6$ films exhibited a 0.43 times higher deposition rate compared to that of the all-light illuminated case: the photocatalytic activity of the $(PW_{12}/TiO_2)_6$ sample was increased by visible light illumination. In contrast, other hybrid films and the $(TiO_2)_6$ film maintained almost identical performance to that before cutting $\lambda > 400$ nm visible light.

In the gaseous phase, O_2 is considered an electron acceptor; plausible reductions are the following.

$O_2 + e^- \rightarrow O_2^- \cdot$ (-0.284 V vs. NHE)

$O_2 + H^+ + e^- \rightarrow HO_2\cdot$ (-0.046 V vs. NHE)

As presented in **Table 5-1**, reduced PW_{12} has a low reaction constant (k of ca. 10^2 $M^{-2}s^{-1}$)

for O_2 reduction because of its high reduction potential (+0.218 V vs. NHE). However, under both UV and visible light, reduced PW_{12} was expected to be excited by visible light and obtained strong reduction power. Using the laser flashing method for the PW_{12}-TiO_2 system, Tachikawa et al. demonstrated that PW_{12} reoxidation occurs rapidly when irradiated with visible light [12]. In their study, reduced PW_{12} was excited by visible light and quickly reduced the methyl viologen in water. In our experiments, acceleration of O_2 reduction is expected to increase the total performance of decomposition.

Both SiW_{12} and H_2W_{12} possess high reaction constants for O_2(10^4–10^6 $M^{-2}s^{-1}$) without visible light. Actually, for the $(SiW_{12}/TiO_2)_6$ and $(H_2W_{12}/TiO_2)_6$ sample, 2-propanol decomposition rates were unchanged by visible light illumination. These data indicate that SiW_{12} and H_2W_{12} possesses sufficient O_2 reduction rates without visible light illumination; $[XW_{12}O_{40}]^{(n+1)}$ reoxidation processes were not rate-controlling steps in this experimental condition.

5.3.1.3. Short UV (< 330 nm) light effects on decomposition

Figures 5-13 and **5-14** depict 2-propanol concentration changes that occur during UV-vis illumination without $\lambda < 330$ nm short UV light. For all samples, the decomposition rate was lower than that of the all-light illumination case. Nonreduced XW_{12} is excited by light of wavelengths less than 350 nm; therefore, XW_{12} is only slightly excited without a short UV illumination condition. **Figure 5-15** portrays the initial 2-propanol decomposition rates when short UV (< 330 nm) was cut. These rates were normalized by each sample's decomposition rate under all-light illumination. Reference $(TiO_2)_2$ and $(PW_{12}/TiO_2)_2$ films show 0.14–0.13 times higher decomposition rates than in the UV-vis case. However $(SiW_{12}/TiO_2)_2$ and $(H_2W_{12}/TiO_2)_2$ show 0.10–0.11

times larger decomposition rates. For the six-bilayer sample, $(SiW_{12}/TiO_2)_6$ and $(H_2W_{12}/TiO_2)_6$ showed that large activities were lower. According to **Table 4-2** (**Chapter 4**), the hybrid thin films have different packing densities and different amounts of XW_{12}. Therefore, it is difficult to discuss differences of activity between hybrid thin films. A plausible explanation is that the acceptor level change by nonreduced XW_{12} excitation if a large decrease in activity of $(SiW_{12}/TiO_2)_6$ and (H_2W_{12}/TiO_2) results from the presence of polyacids. Holes are generated in the HOMO level of XW_{12}; subsequently, the acceptor level changes from LUMO to HOMO when XW_{12} is excited by UV light of a short wavelength. The hole in HOMO level has strong oxidation power. Therefore, photoexcited XW_{12} acts as a stronger electron acceptor than ground state XW_{12} [13]. The ground state SiW_{12} and H_2W_{12} LUMOs possess lower reduction potential than PW_{12}, so they are expected to be difficult to accept electrons from TiO_2 conduction band without short UV excitation: electron transfer from TiO_2 to XW_{12} can accelerate from short UV illumination.

Figure 5-16 presents a redox and electron transportation model in the XW_{12}-TiO_2 system. All reactions portrayed in the figure can occur. However, the contribution of each reaction to 2-propanol decomposition depends on the XW_{12} energy level and quantum efficiency of photoexcitation. For the PW_{12}-TiO_2 system, ground-state PW_{12} has higher quantum efficiency and reduction potential than other XW_{12} (**Table 5-1**). Consequently, visible light illumination is effective and reduction **1** is expected to be an important step. However, for SiW_{12}-TiO_2 and H_2W_{12}-TiO_2 systems, ground state SiW_{12} and H_2W_{12} have sufficient reduction potential for O_2 reduction. Therefore, they maintain high decomposition rates without visible light illumination: reduction **2** is expected to be the main reaction.

5.3.2. Photocatalytic activity of the (PW_{12} /TiO_2)$_n$ films

Top surfaces of hybrid films affect the decomposition performance if XW_{12} truly acts as a reduction site and adsorbent. In this section, we discussed XW_{12} effects in detail using (PW_{12}/TiO_2)$_n$ and reference films. **Figure 5-17** portrays the change of concentrations of 2-propanol and acetone during all-light illumination for the (PW_{12}/TiO_2)$_2$ hybrid film, the (PW_{12}/TiO_2)$_2$ + PW_{12} film (PW_{12} was the top layer), the (TiO_2)$_2$ film (photodecomposed (PSS/TiO_2)$_2$ film), and the (PW_{12})$_2$ film (photodecomposed (PW_{12}/PDDA)$_2$. In these experiments, the initial concentration was 26–28 ppm initially of illumination. Comparing the 2-propanol decomposition rate, the hybrid thin films exhibited higher photocatalytic activities. The (PW_{12})$_2$ thin film exhibited extremely low photocatalytic activity. The sum of the decomposition amount by (PW_{12})$_2$ and (TiO_2)$_2$ films was less than that by the (PW_{12}/TiO_2)$_2$ hybrid thin film, which indicated that some interaction existing between PW_{12} and TiO_2 hasten 2-propanol decomposition. The initial 2-propanol decomposition rate of (PW_{12}/TiO_2)$_2$+PW_{12} was almost equal to that of (PW_{12}/TiO_2)$_2$, despite different TiO_2 surface coverage. Photocatalytic decomposition activity on the gaseous compound that adsorbs on the surface of TiO_2 usually depends on the TiO_2 surface area [14]. Surface chemical compositions of hybrid films (**Fig. 4-17**, **Chapter 4**) indicate that the XW_{12} anion in LBL films does not have the closest packing structure. Consequently, a part of the TiO_2 surface is expected to be exposed even when the top layer is PW_{12}. That is one reason for the high decomposition activity of the (PW_{12}/TiO_2)+PW_{12} sample; both reduction and oxidation sites exist on the surface. **Figure 5-17 (a)**, (PW_{12}/TiO_2)$_2$+PW_{12} shows that the high decomposition rate was maintained even after 60 min from the start of illumination; on the other hand, $(PW_{12}/TiO_2)_2$ exhibited a lower decomposition rate than the initial state. The top PW_{12} layer was effective for 2-propanol adsorption. After 30 h decomposition, the increment of CO_2 concentration (ΔCO_2) was about 150 ppm. The injected 2-propanol amount in the vessel corresponded to 50 ppm. Consequently, nearly three times the amount of CO_2 was expected to have been generated. Therefore, 2-propanol was expected to have been decomposed completely.

Decomposition experiments were carried out with $n = 6$ samples to investigate the decomposition rate dependence on the layer thickness. **Figure 5-18** portrays the concentration change of 2-propanol and acetone during all-light illumination. The activity of the TiO_2 control sample increased with increasing layer thickness, which is expected to reflect the increasing number of photogenerated holes and resultant radical species. On the other hand, the $(PW_{12}/TiO_2)_6$+PW_{12} film exhibited almost identical 2-propanol decomposition rate as that of the $n = 2$ sample. These results conflict with those presented in the preceding section (**Fig. 5-8**). One reason is humidity in the air. Water vapor in the atmosphere engenders a stark change in the decomposition performance [15] because of active ·OH radical and other radical generation depending on the water amount present on the TiO_2 surface. These experiments were carried out without humidity control. For that reason, the decomposition rate did not agree with the results described in section 5.3.1.

For the $(PW_{12})_6$ film, the 2-propanol concentration decreased gradually with time. However, the acetone concentration was almost identical to that of $(PW_{12})_2$, which suggests that the $(PW_{12})_6$ thin film absorbed 2-propanol, acetone, and the intermediate in the interlayer. **Figure 5-18(b)** portrays the concentration change of acetone during UV illumination of $n = 6$ samples. Increasing layer thickness increased the acetone decomposition rate of the hybrid films. Especially, the $(PW_{12}/TiO_2)_6$+PW_{12} sample exhibited a high acetone decomposition rate: all acetone was decomposed in 6 h. This trend differs from that of 2-propanol decomposition under this condition. It was observed when decomposition experiments were carried out repeatedly. The acetone decomposition rate depends on the layer thickness. This result indicates that the bottom or inner part of the $n = 6$ sample is also related to acetone decomposition. The whole sample contributes to the acetone decomposition. However, in the case of 2-propanol decomposition, only the material near the surface contributes. Results suggest that the relation between the organic molecule diffusion rate into the layer and the photocatalytic decomposition rate affects the decomposition rate dependence on the layer thickness. Further investigation of the interlayer reaction is necessary to elucidate this difference. The photocatalytic reaction in this film is not simple; it is related to the charge transfer between PW_{12} and TiO_2. Moreover, the top layer is expected to affect molecular adsorption, release behavior, and the balance between reduction and oxidation.

Figure 5-19 portrays the 2-propanol concentration change during UV illumination without $\lambda > 400$ nm visible light. Six-bilayer hybrid films and $(TiO_2)_6$ were used for this experiment. For hybrid films, 2-propanol decomposition and acetone generation were stopped after 1 h of illumination. On the other hand, the TiO_2 film maintained the same performance after cutting $\lambda > 400$ nm visible light. The results show the same trend as that of **Figs. 5-10** and **5-12**. Visible light photoexcitation hastens the 2-propanol decomposition for $(PW_{12}/TiO_2)_6$ and (PW_{12}/TiO_2)+PW_{12}. When the top layer was PW_{12}, the hybrid sample exhibited lower photocatalytic activity than $(PW_{12}/TiO_2)_6$, whose top layer was TiO_2. The surface PW_{12} is not an effective reduction site without visible light. Consequently, the large TiO_2 surface area presents advantages for total decomposition performance. **Figures 5–20** depict the 2-propanol decomposition when the short wavelength UV (<330 nm) was cut. For all samples, decomposition rates were decreased. The hybrid film showed higher decomposition rate than $(PW_{12}/TiO_2)_6$ when the top layer was PW_{12}. Under visible light illumination, PW_{12} is expected to be an effective reduction site. For that reason, the $(PW_{12}/TiO_2)_6$+PW_{12} sample top surface, which was covered by PW_{12} showed a high decomposition rate.

5.4. Conclusion

In this chapter, photocatalytic activities of the $(XW_{12}/TiO_2)_n$ thin films were evaluated using 2-propanol decomposition. The two-bilayer $(H_2W_{12}/TiO_2)_2$ and $(PW_{12}/TiO_2)_2$ films (ca. 15 nm) exhibited higher decomposition rates than that of the control $(TiO_2)_2$ film. Photocatalytic performance of the hybrid thin films was related to the Keggin-type polyacid redox property. Results of decomposition experiments under limited wavelengths indicate that the O_2 reduction rate on XW_{12} is important for overall decomposition performance. A Z-scheme reaction is expected to occur in $(PW_{12}/TiO_2)_n$ films. However, the $(SiW_{12}/TiO_2)_n$ and $(H_2W_{12}/TiO_2)_n$ films' decomposition rates did not change when visible light was cut. The photocatalytic decomposition activity also depends on the number of bilayer coatings, the top coating, and organic compounds for decomposition.

References

[1] Hill, C. L.; Prosser-McCartha, C. M. *Cood. Chem. Rev.*, **143**, 407-455 (1995).

[2] Okuhara, T.; Mizuno, N.; Misono, M. *Adv.Catal.*, **41**, 113-252 (1996).

[3] Papaconstantinou, E.; Dimotikali, D.; Politou, A. *Inorg. Chem. Acta*, **43**, 155-158 (1980).

[4] Akid, R.; Darwent, J. R. *J. Chem. Soc. Dalton Trans.*, 395-339 (1985).

[5] I. A. Weinstock, *Chem. Rev.*, **98**, 113-170 (1998).

[6] Harvey, P. R.; Rudham, R.; Ward, S. *J. Chem. Soc. Faraday Trans. 1*, **79**(6), 1381-1390 (1983).

[7] Ohko, Y.; Hashimoto, K.; Fujishima, A. *J. Phys. Chem. A*, **101**(43), 8057-8062 (1997).

[8] Mylonas, A.; Hiskia, A.; Androulaki, E.; Dimotikali, D.; Papaconstantinou, E. *Phys. Chem. Chem. Phys.*, **1**, 437-440 (1999).

[9] Lanson, S. A.; Widegren, J. A.; Falconer, J. L. *J. Catal.*, **157**(2), 611-625 (1995).

[10] Anbar, M.; Neta, P. *Int. J. Appl. Radiat. Isotopes*, **18**(7), 493-523 (1967).

[11] Mizuno, N.; Misono, M. *Chem. Rev.*, **98**, 119-217 (1998).

[12] Tachikawa, T.; Tojo, S.; Fujitsuka, M.; Majima, T. *Chem. Eur. J.*, **12**, 3124-3131, (2006).

[13] Borrás-Almenar, J. J.; Coronado, E.; Müller, A.; Pope, M. *Polyoxometalate Molecular Science*; Kluwer Academic Publishers: Dordrecht / Boston / London, 381-416 (2001).

[14] Nosaka, Y; Nosaka, A. Nyumon Hikari Shokubai; Tokyo Tosho Co., Ltd.: Tokyo (2004) in Japanese.

[15] Takeuchi, M.; Deguchi, J.; Anpo, N. 26th Hikarigakakawaru shokubaikagaku Symposium 18–22 in Proceedings (2007) in Japanese.

[16] http://www.htkgp.co.jp/hwatch/tokuhin/luminar/LA-410UV.html, Hayashi Watch Works Co. Ltd. HP (accessed November 2008).

Table 5-1. Polyanion reduction potentials (E), change of Gibbs free energy for electron transfer from reduced polyanion to O_2 (ΔG), relatively quantum yields for photochemical formation of reduced polyanions (F_{rel}), and rate constants for electron transfer from reduced polyanion to O_2 (k) [5]

Polyanion_{ox}	Polyanion_{red}	E (V vs NHE)	ΔG^{*} (kcal mol^{-1})	F_{rel} [POM_{red}]	k^{**} ($M^{-2}s^{-1}$)
$[PW_{12}O_{40}]^{3-}$	$[PW_{12}O_{40}]^{4-}$	+0.218	+2.26	1.00	7.5×10^2
$[SiW_{12}O_{40}]^{4-}$	$[SiW_{12}O_{40}]^{5-}$	+0.054	-1.52	0.70	6.5×10^4
$[Fe^{III}W_{12}O_{40}]^{5-}$	$[Fe^{III}W_{12}O_{40}]^{7-***}$	-0.619^{***}	-6.66	0.09	2.8×10^6
$[H_2W_{12}O_{40}]^{6-}$	$[H_2W_{12}O_{40}]^{7-}$	-0.162	-6.50	0.13	1.7×10^6

[*] Calculated using E (O_2/HO_2) = +0.12 V vs NHE at pH = 0.

[**] Calculated from reported value using $[O_2] = 2 \times 10^{-4}$ M and $[H]^+ = 0.1$ M.

[***] The doubly reduced anion was formed.

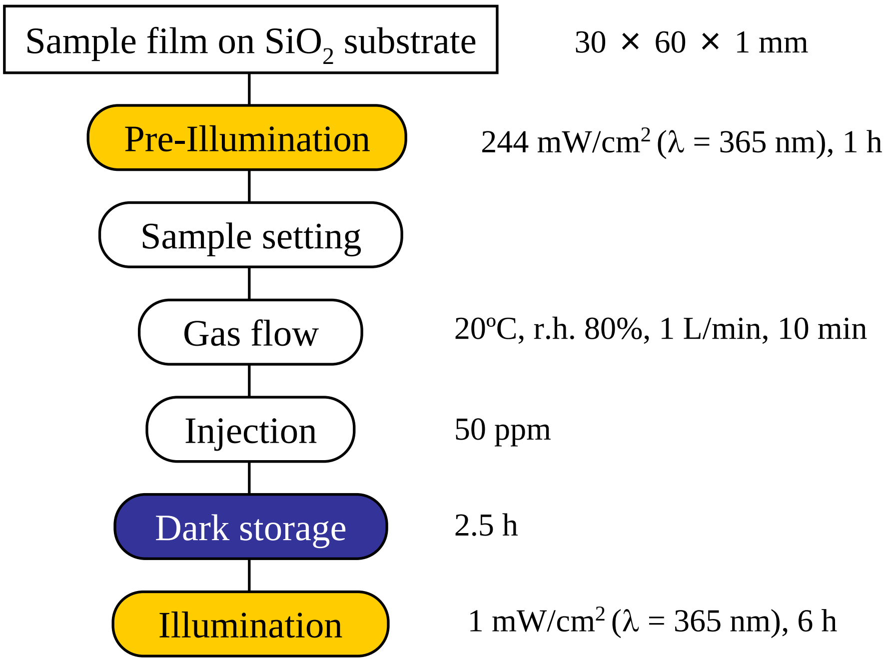

Figure 5-1. Experimental procedure of 2-propanol decomposition.

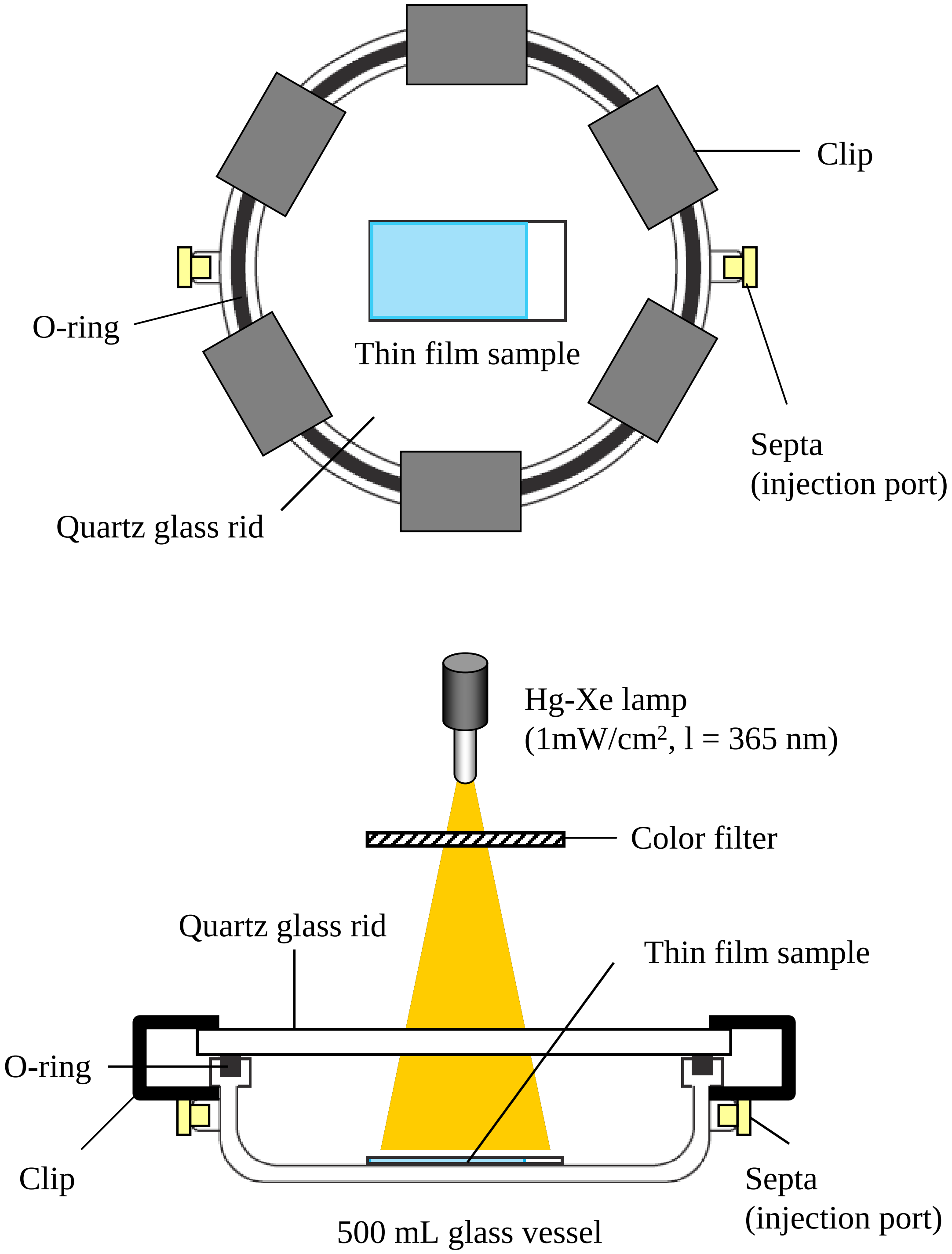

Figure 5-2. Schematic illustration of reactor setting and UV-vis illumination for 2-propanol decomposition.

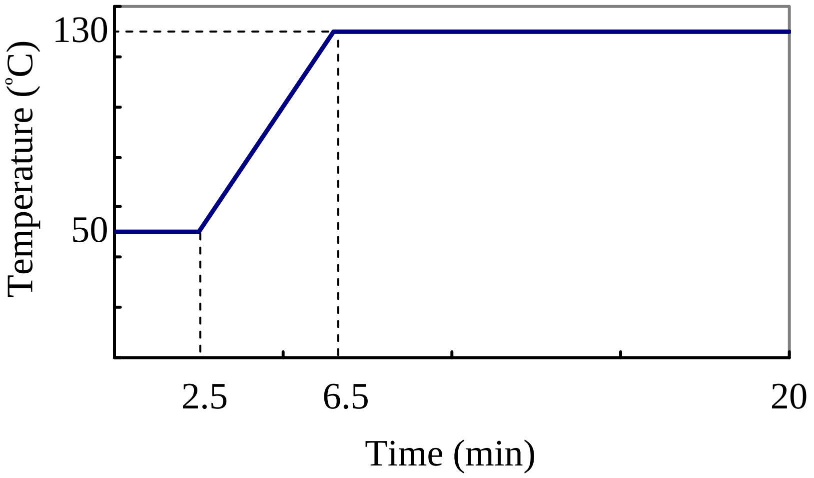

Figure 5-3. Temperature diagram of gas chromatography column oven during analysis.

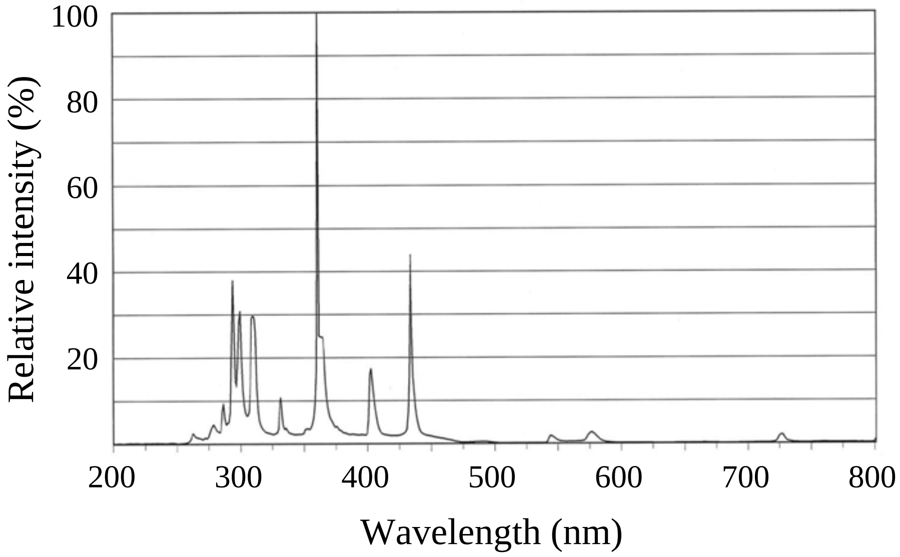

Figure 5-4. Wavelength spectra of the light source. Reprinted with permission from ref [16]. Copyright Hayashi 2000-2006.

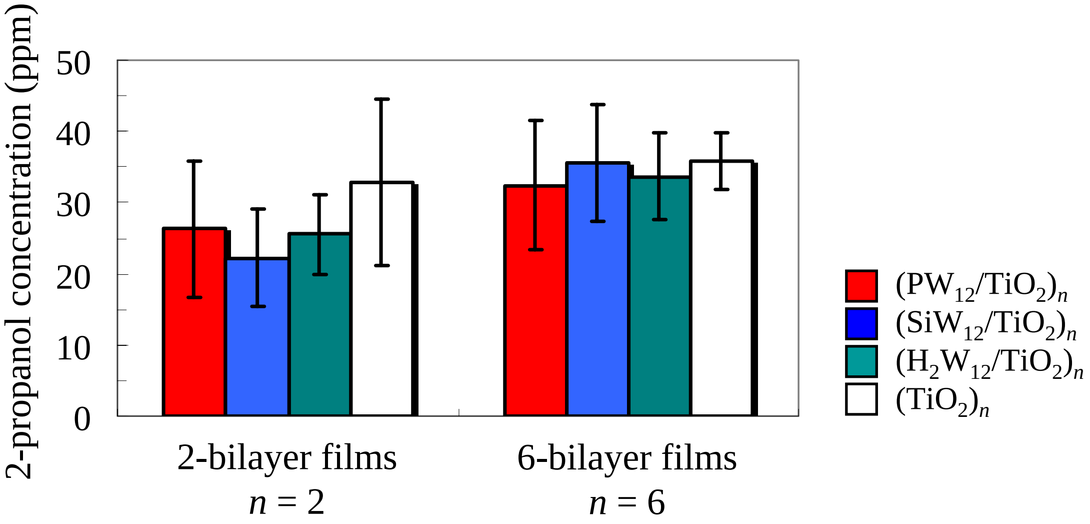

Figure 5-5. Initial concentrations of 2-propanol (C_0) after dark storage. (a) 2-bilayer hybrid thin films and the $(TiO_2)_2$ reference film, (b) 6-bilayer hybrid thin films and the $(TiO_2)_6$ film.

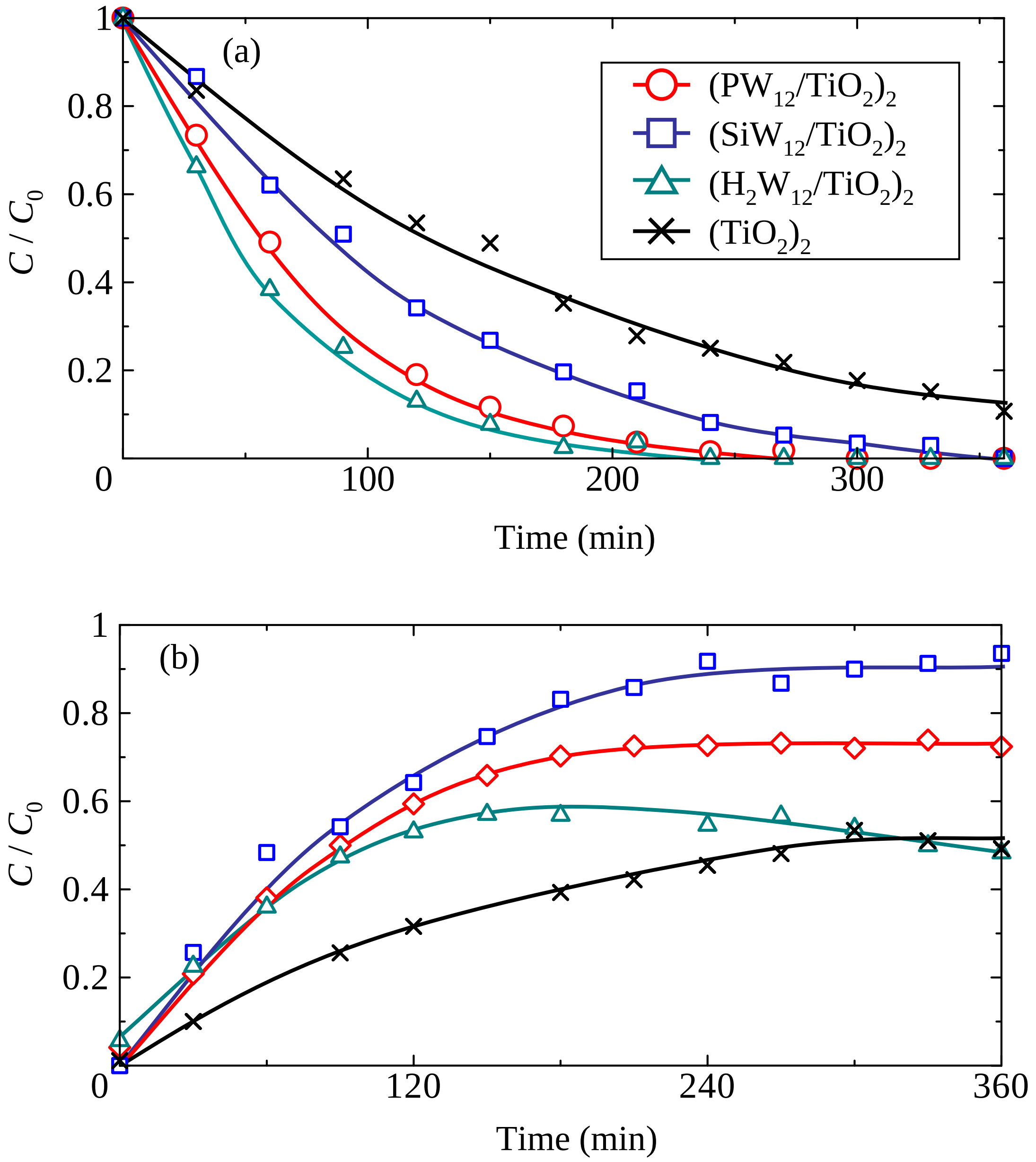

Figure 5-6. Concentration change during UV-vis illumination using n = 2 $(XW_{12}/TiO_2)_n$ thin films and reference thin films.
(a) 2-propanol, (b) acetone.

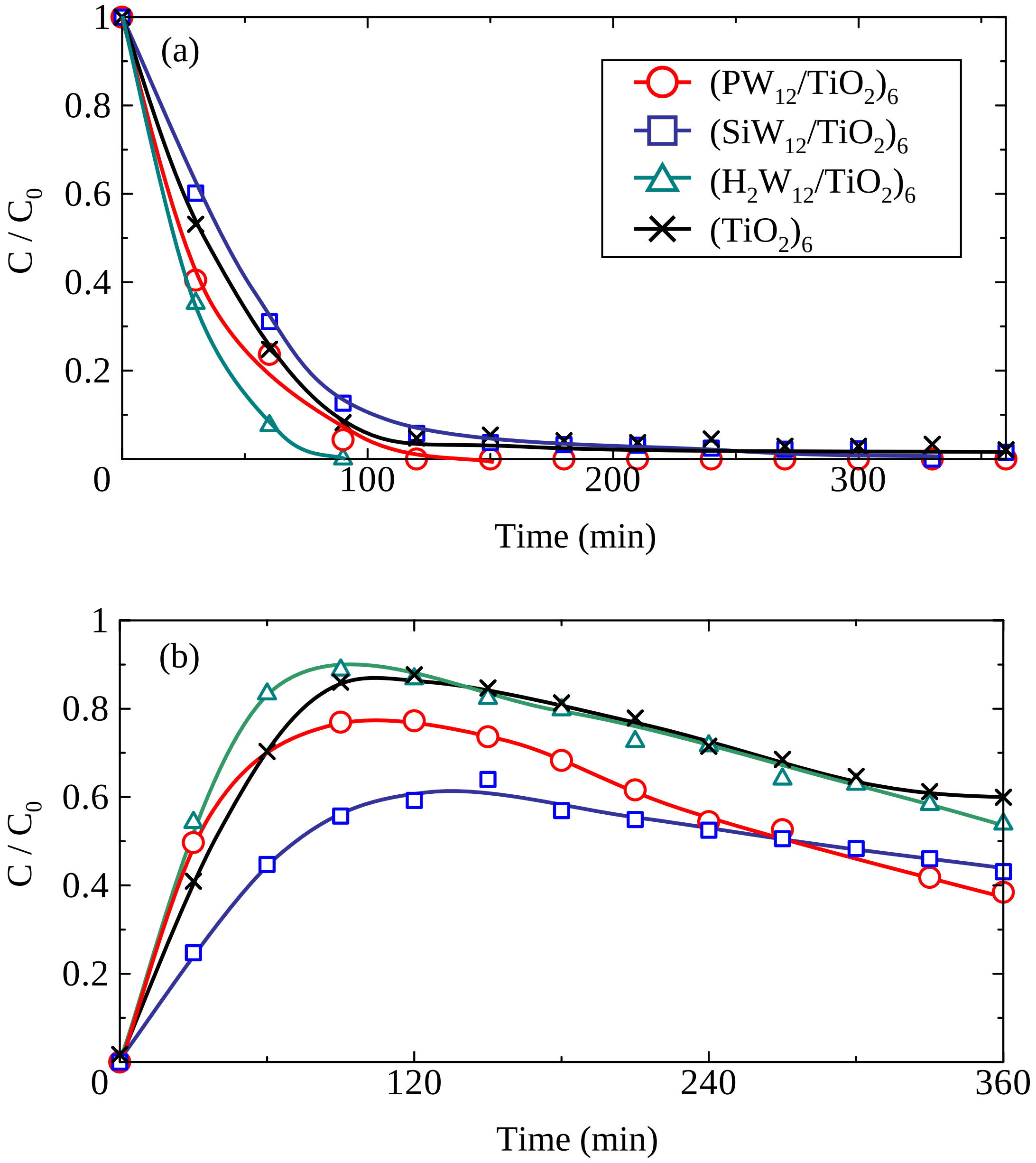

Figure 5-7. Concentration change during UV-vis illumination using n = 6 $(XW_{12}/TiO_2)_n$ thin films and reference thin films.

(a) 2-propanol, (b) acetone.

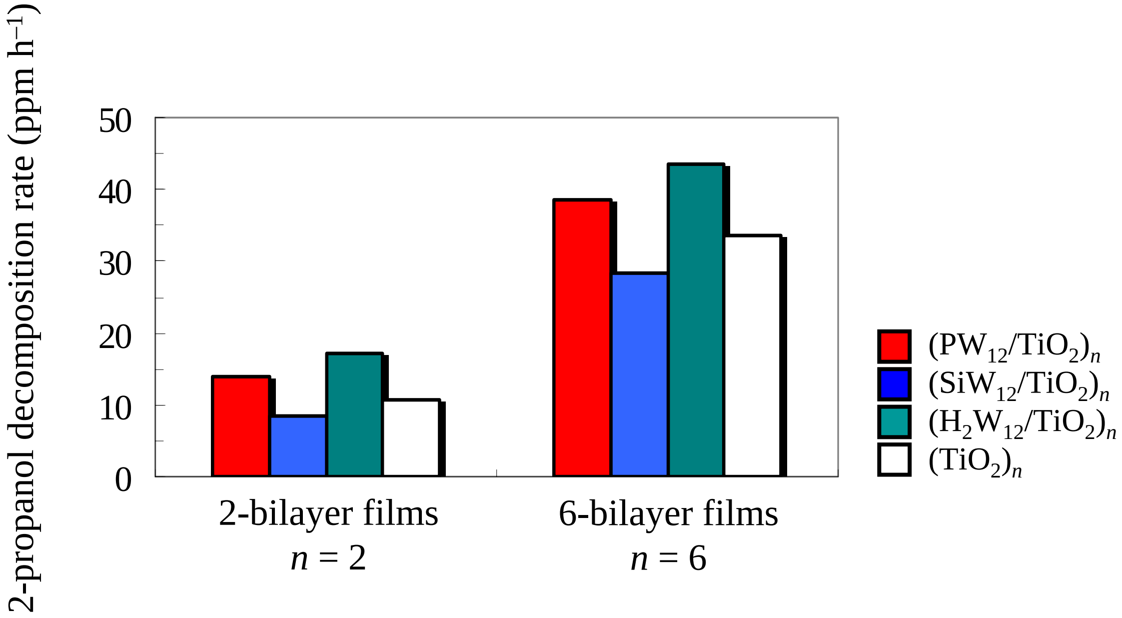

Figure 5-8. Initial decomposition rate of 2-propanol under UV-vis illumination.

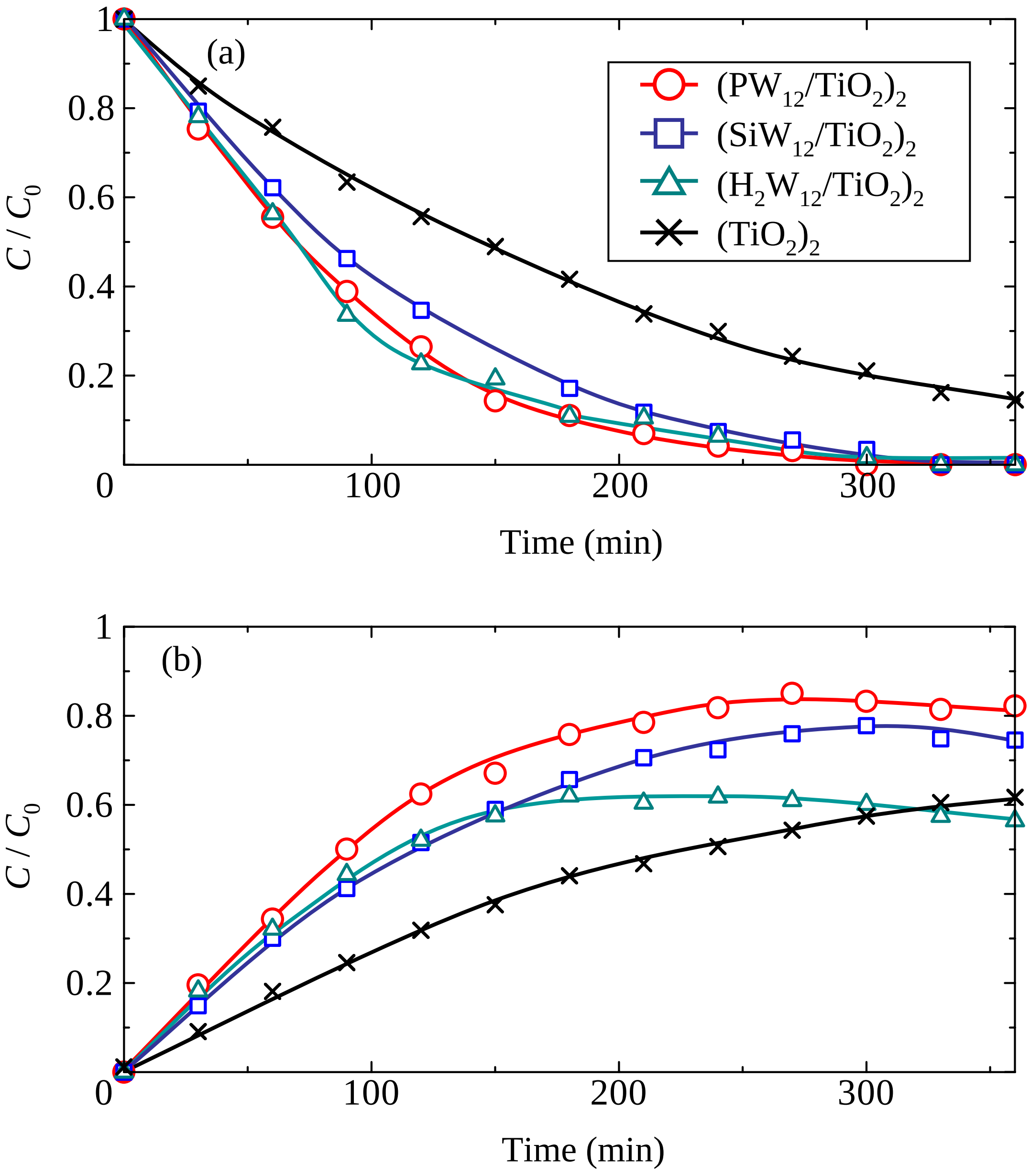

Figure 5-9. Concentration change when visible light (> 400 nm) was cut for $n = 2$ $(XW_{12}/TiO_2)_n$ thin films and reference thin films.
(a) 2-propanol, (b) acetone.

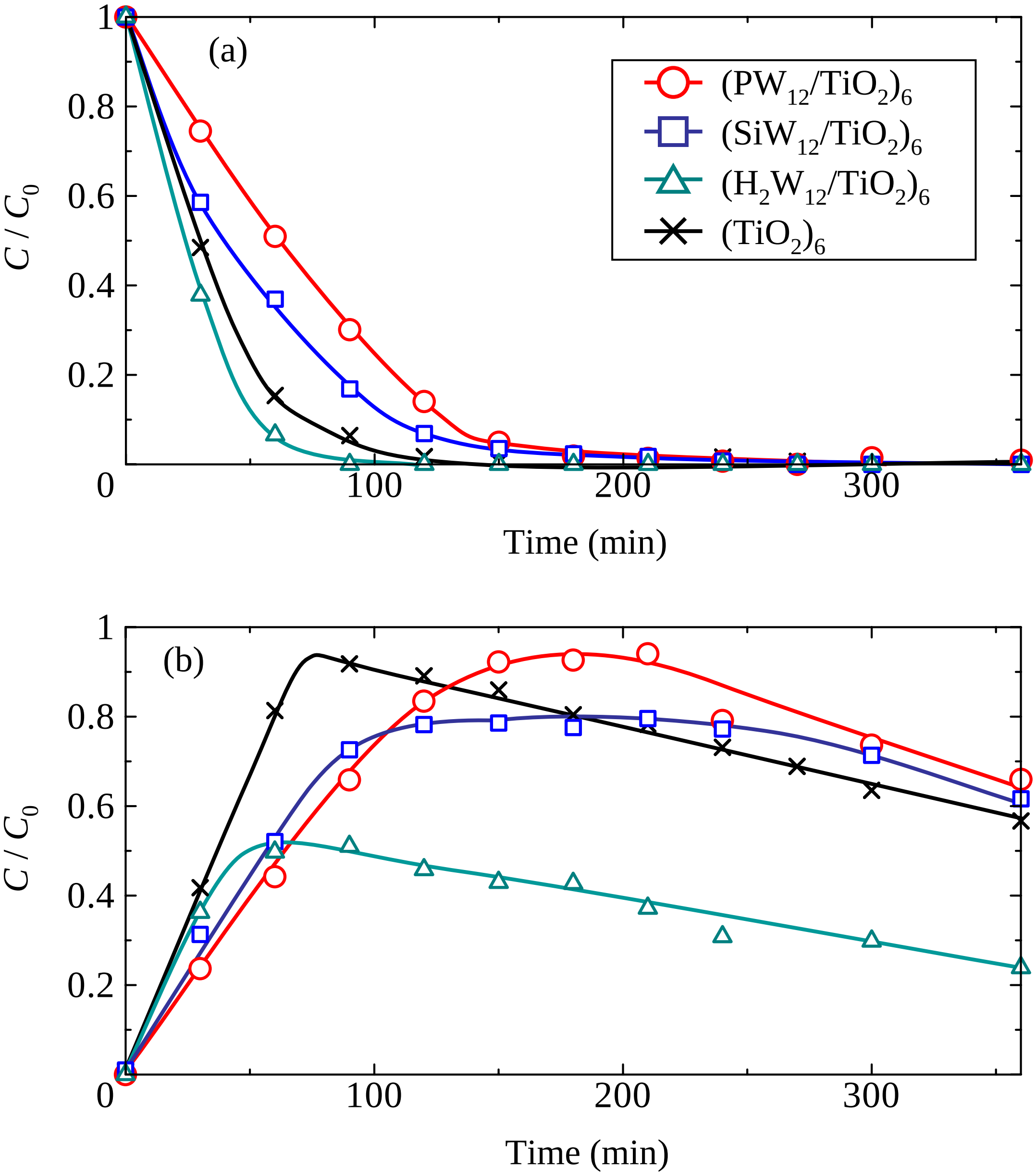

Figure 5-10. Concentration change when visible light (> 400 nm) was cut for $n = 6$ $(XW_{12}/TiO_2)_n$ thin films and reference thin films.
(a) 2-propanol, (b) acetone.

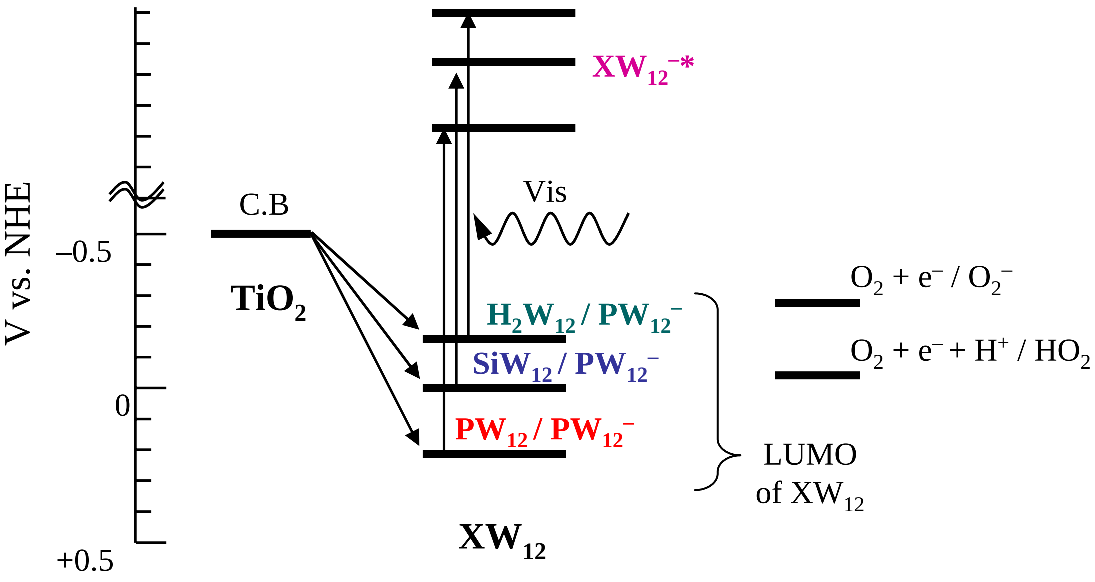

Figure 5-11. Energy diagram of TiO_2 conduction band, XW_{12} reduction potentials, and O_2 reduction potentials.

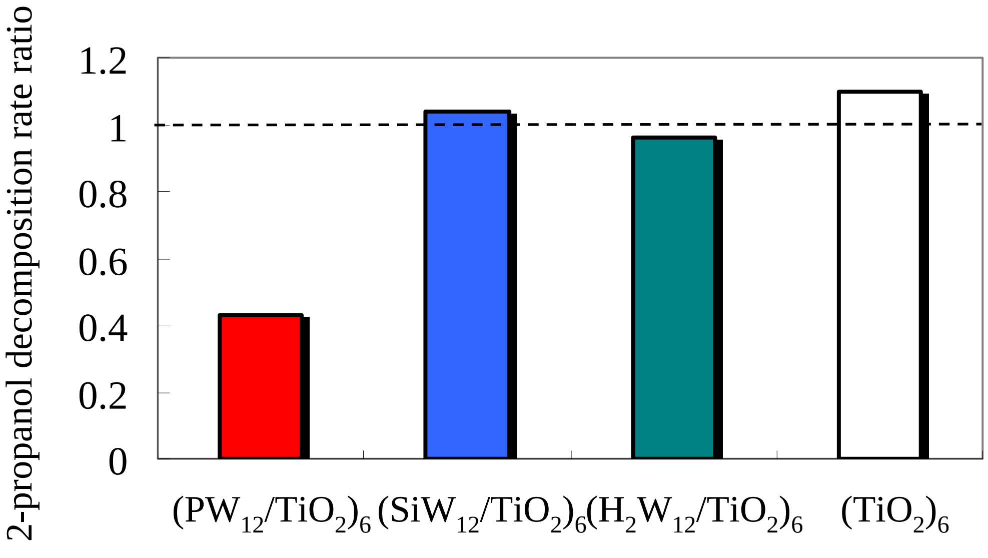

Figure 5-12. Decomposition rate of 2-propanol when visible light (> 400 nm) was cut. They are normalized by each sample's decomposition rate under all-light illumination.

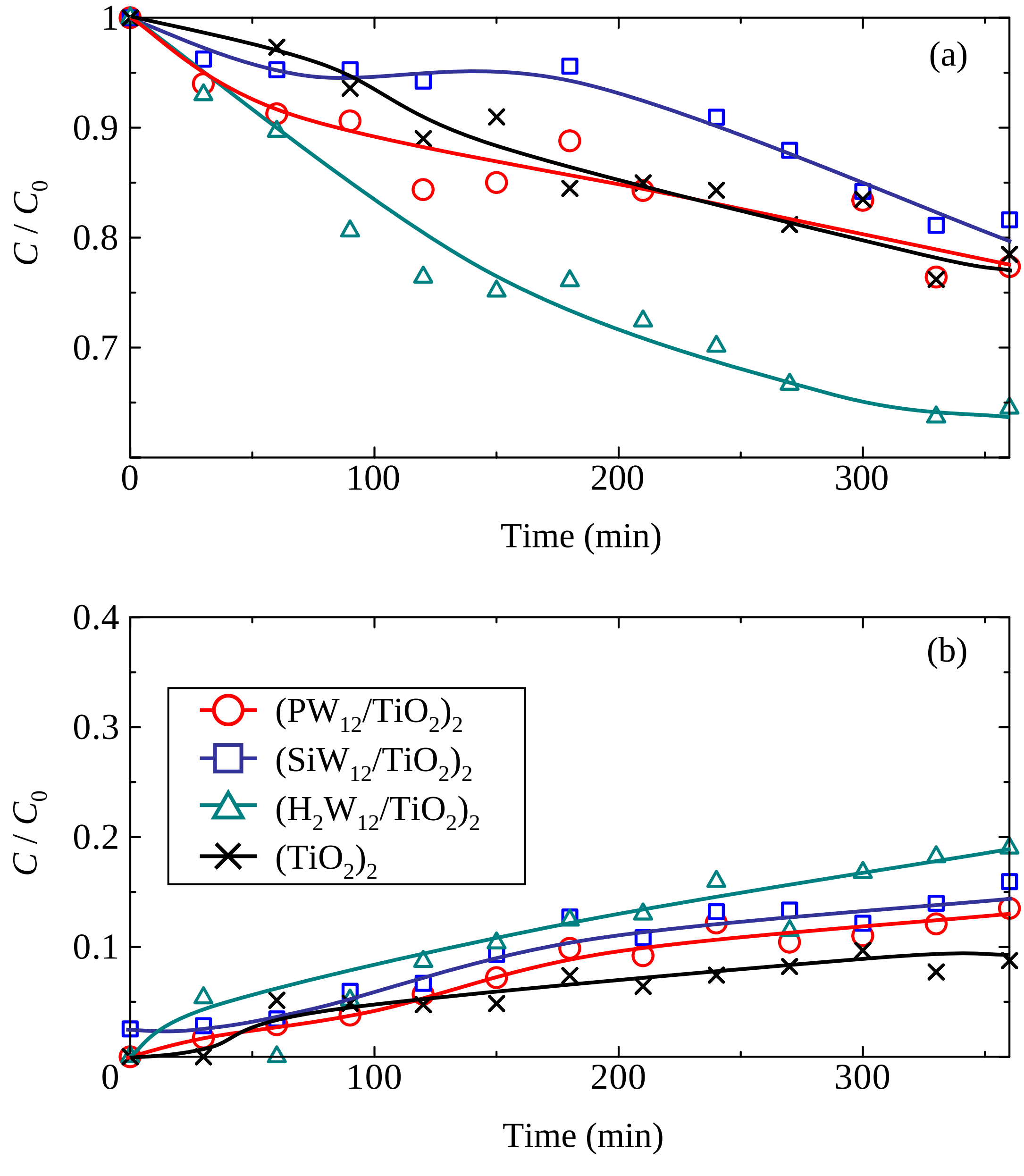

Figure 5-13. Concentration change when short UV (< 330 nm) was cut for $n = 2$ $(XW_{12}/TiO_2)_n$ thin films and reference thin films.
(a) 2-propanol, (b) acetone.

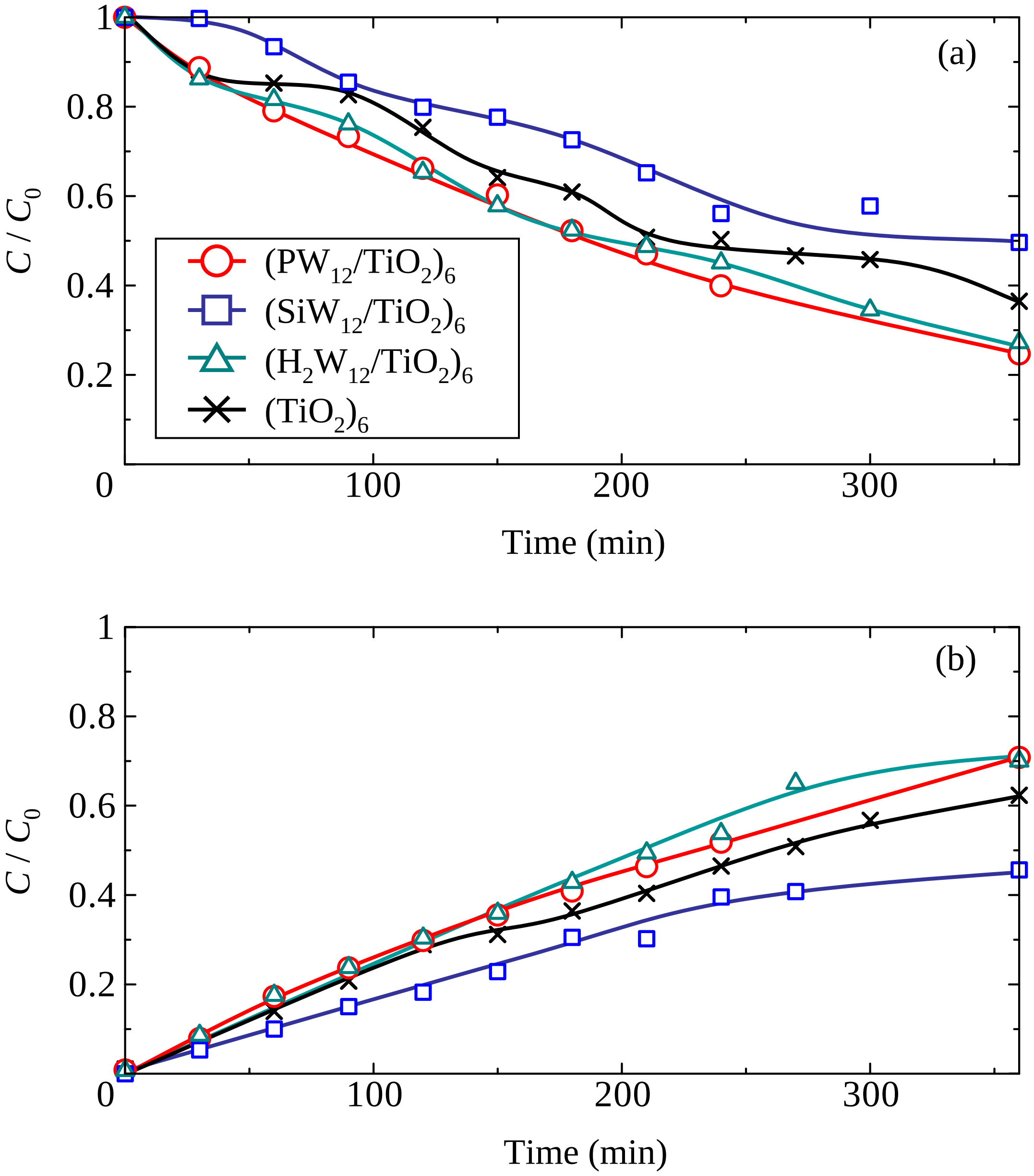

Figure 5-14. Concentration change when short UV (< 330 nm) was cut for $n = 6$ $(XW_{12}/TiO_2)_n$ thin films and reference thin films.
(a) 2-propanol, (b) acetone.

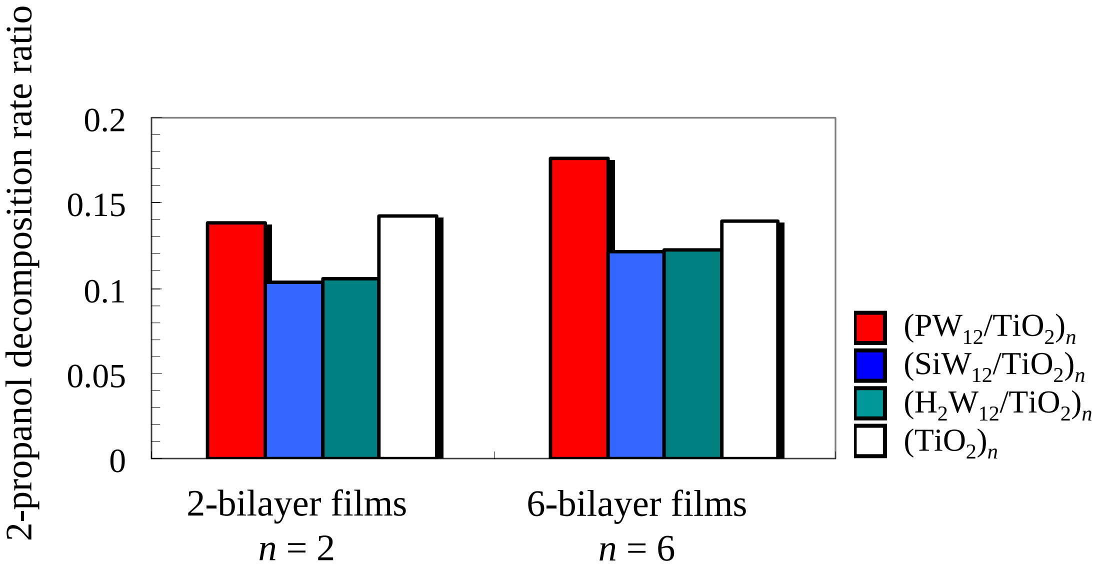

Figure 5-15. Decomposition rate of 2-propanol when short UV (> 330 nm) was cut. The data was normalized by each sample's decomposition rate under all-light illumination.

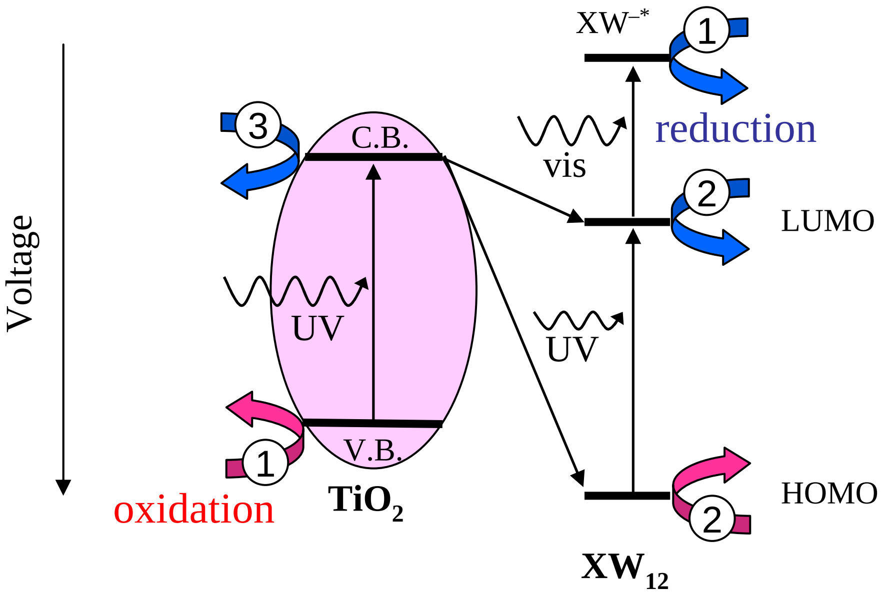

Figure 5-16. Redox and electron transportation in XW_{12}-TiO_2 system.

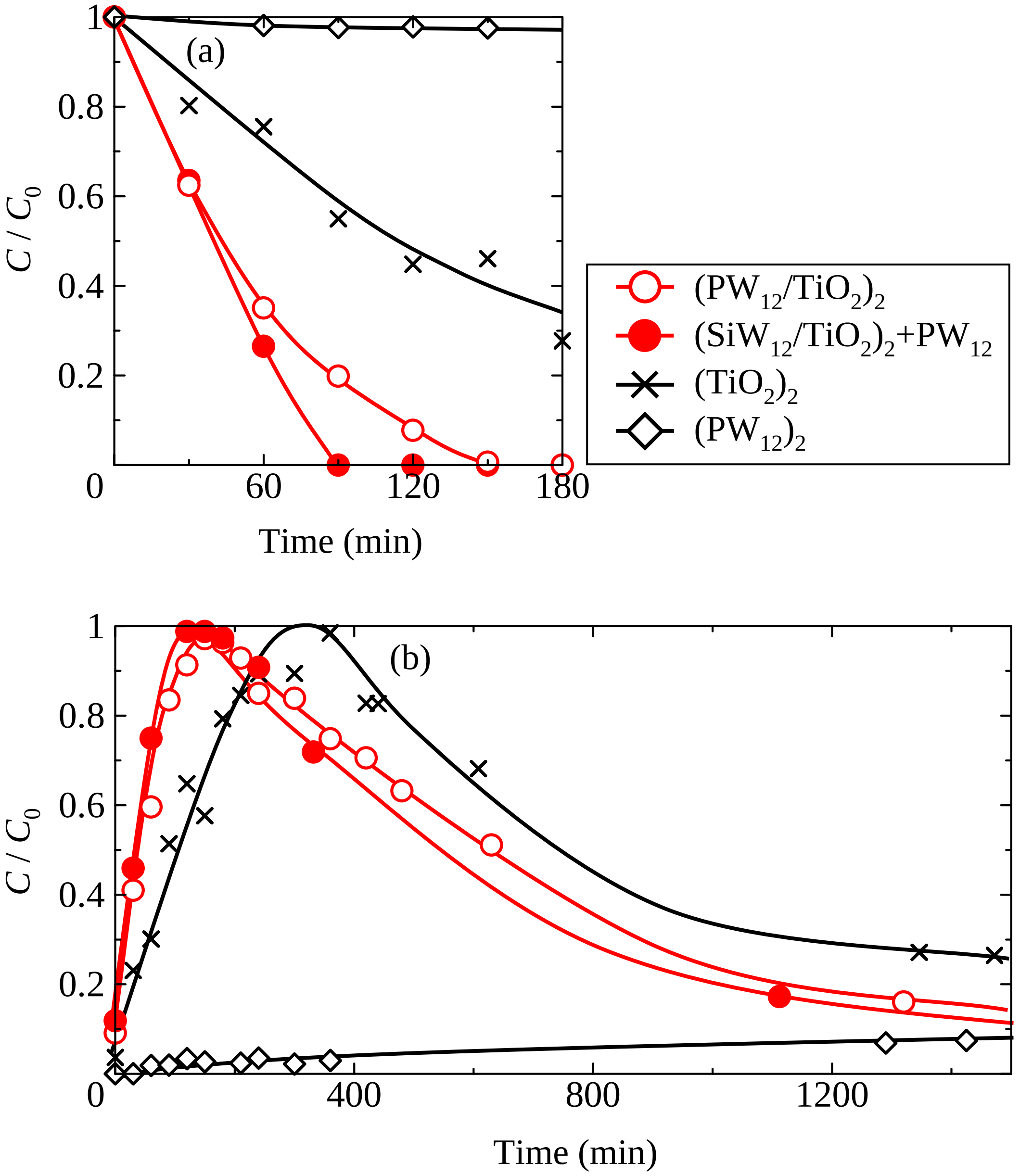

Figure 5-17. Concentration change under all-light illumination for n = 2 $(PW_{12}/TiO_2)_n$ thin films and reference thin films. (a) 2-propanol , (b) acetone.

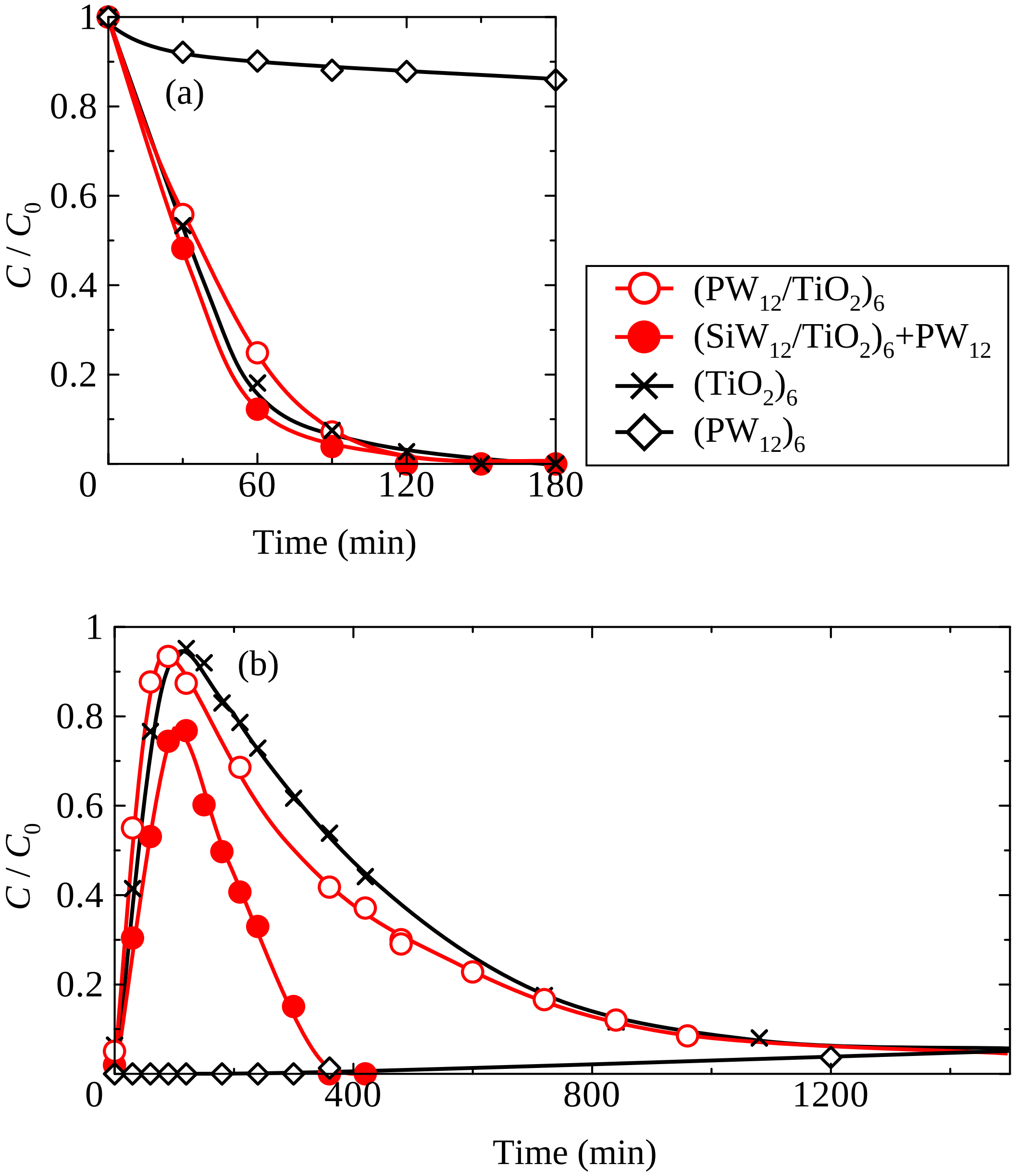

Figure 5-18. Concentration change under all-light illumination for $n = 6$ $(PW_{12}/TiO_2)_n$ thin films and reference thin films. (a) 2-propanol, (b) acetone.

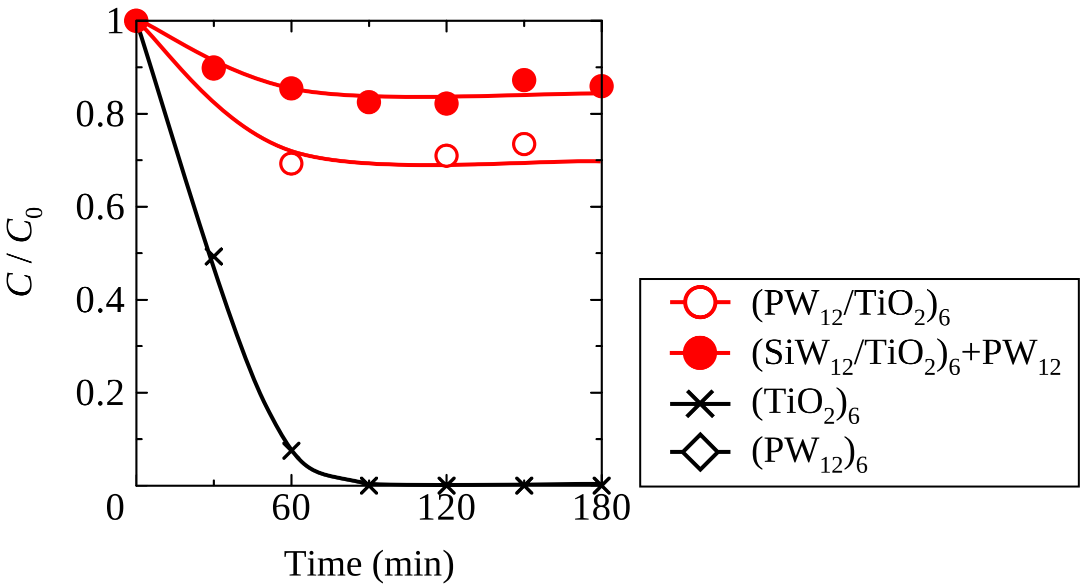

Figure 5-19. Concentration change for 2-propanol when visible light (> 400 nm) was cut.

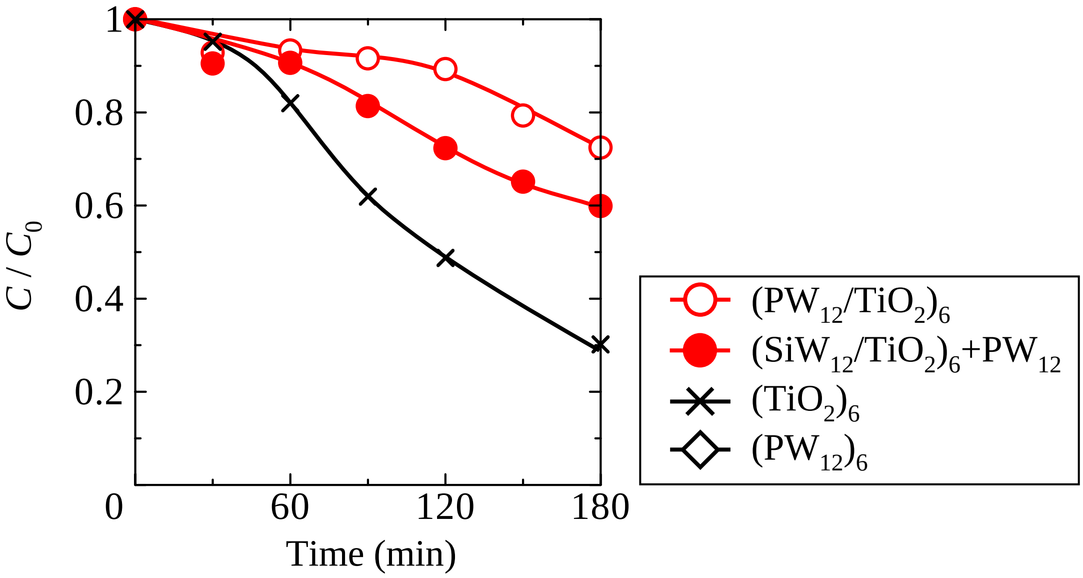

Figure 5-20. Concentration change of 2-propanol when short UV (< 330 nm) was cut.

CHAPTER 6

Photocatalytic Decomposition of Hydrofluorocarbons

6.1. Environmental contamination of Fluorocarbons

6.1.1. Ozone depletion by Chlorofluorocarbons

Chlorofluorocarbons ($C_xCl_yF_z$, hereinafter denoted as CFCs) and Bromochlorofluorocarbons ($C_xBr_yF_z$ or $C_xBr_yCl_zF_s$, halons) are artificial molecules that were first created during the 1930s. They have many unique properties: a relatively low boiling point, non-flammability, chemical stability, and relative safety for humans. They came to be used widely in industry as refrigerants, propellants for aerosol sprays, cleaning solvents for circuit boards, and foam blowing agents. Annual emission amounts of CFC-12, a particular refrigerant, reached 400,000 t in the mid-1970s [1].

In 1974, Molina and Rowland presented their first hypothesis about stratospheric ozone depletion by CFCs [2]. Subsequently, that ozone layer depletion mechanism was clarified in detail by many researchers [3–5]. Actually, CFCs are decomposed by short UV (<240 nm) in the stratosphere, thereby generating radical species that cause catalytic chain reactions. Simplified reactions can be presented as the following reaction formulas:

$Cl\cdot + O_3 \rightarrow ClO\cdot + O_2$

$ClO\cdot + O_3 \rightarrow Cl\cdot + 2O_2$

Bromine in halons also decomposes ozone through similar reactions [5]. Harmful short UV would reach the earth surface if ozone layer depletion were to continue. International regulations were adopted and the Montreal Protocol was signed in 1987; a phase-out schedule for HFCs and some hydrochlorofluorocarbons (HCFCs) was adopted. **Tables 6-1** and **6-2** present compounds under the phase-out schedule adopted under the Montreal

Protocol [1, 6].

Hydrofluorocarbons (HFCs) are widely used as a CFC substitute. Table 6-3 presents HFCs that are used as alternative materials in the chemical industry. They are not ozone-depleting substances but long-lifetime greenhouse gases. Actually, HFC-134a, the most commonly used CFC substitute refrigerant, has 2800 times the global warming potential as that of CO_2. Because of its high global warming potential, CFC emissions have been regulated by the Kyoto Protocol, signed in 1997. In Japan, CFC collection from industrial wastes and subsequent CFC destruction have been obligatory since 2002 [7].

6.1.2. Water contamination with fluorocarbons

Fluorocarbons are very stable and are only slightly decomposed in the environment. Emitted non-volatile fluorocarbons persist in environmental water for a very long time. These compounds have received special attention because of their widespread contamination of oceans and rivers. Suspected of being toxic to humans, they cause developmental disabilities in animals [8]. Currently, perfluorooctanesulfonate (PFOS) and related HFCs are increasingly detected in wild marine mammals, fish, birds, and in human blood [9]. In Japan, Harada reported concentrations of PFOA and PFOS in human sera. He obtained samples of sera from various prefectures: all sera contained slight amounts of PFOS (7.6–26.8 ng/ml) and PFOA (2.3–14.5 ng/ml). Some chemical producers have begun reducing PFOS and PFOA emissions independently.

6.2. Fluorocarbon decomposition

Actually, HFCs and HFCs are very stable compounds. Therefore, both emission bans and development of destruction methods are necessary to prevent environmental contamination. For CFC and HFC destruction, thermal decomposition [10], catalytic decomposition [11, 12], and plasma decomposition [13, 14] are practically used [15]. However, large amounts of energy and massive equipment are required for these processes. Moreover, direct decomposition of concentrated gases is difficult because of consequent HF and HCl gas generation.

Several reports have described HFC and CFC photocatalytic decomposition using TiO_2 photocatalysts [16–20]. In those reports, some features were clarified in gaseous reaction; HFC and CFC photodecomposition is a low-rate reaction because of the high C–F bonding energy (470–530 kJ/mol [21]); the presence of water vapor and O_2 strongly affect decomposition behavior [18–20]; and CFCs and HFCs are finally degraded to CO_2, HF, and HCl. On the other hand, Hori et al. decomposed HFCs using heteropolyacid photocatalyst in a homogeneous reaction in aqueous phase [22, 23]. High oxidation potential and forming complex between PW_{12} and substance were expected to facilitate decomposition. For the investigation described in this chapter, we prepared TiO_2 and PW_{12}-TiO_2 powder photocatalysts to examine its photocatalytic decomposition activity on HFC-134a. This is the first report of CFC-134a photocatalytic decomposition. Decomposition experiments were carried out under various light intensities to obtain fundamental knowledge related to HFC-134a decomposition. Hybridization and particle diameter effects were also discussed.

6.3. Experimental procedure

6.3.1. Preparation of hybrid and reference samples

Commercial high-purity TiO_2 (anatase) powder (ST-21; Ishihara Sangyo Kaisha Ltd., Osaka, Japan) and a commercial TiO_2 aqueous suspension (STS-100, 20 wt%

concentration; Ishihara Sangyo Kaisha Ltd., Mie, Japan) were used as starting materials. Reagent grade 12-tungstophosphoric acid hydride ($H_3PW_{12}O_{40} \cdot nH_2O$, abbreviated as PW_{12}) was used, with no purification, for preparation of PW_{12}-TiO_2 hybrid powder. The PW_{12} (0.06, 0.1, 0.5 g) was dissolved in 100 ml HNO_3 aqueous solution. The PW_{12} solutions were adjusted pH = 1.5 to prevent PW_{12} hydrolysis. Then 2.0 g ST-21 (d = 20 nm) was mixed in the PW_{12} solution and stirred for 24 h. Subsequently, the solid was separated by centrifugation (8000 rpm, 20 min) and then washed twice with diluted HNO_3 (pH = 1.5). After drying (60°C, 24 h), PW_{12}-TiO_2 hybrid powder was obtained.

Fine TiO_2 powder was prepared from STS-100 suspension. The STS-100 (d = 6 nm) was dried on an evaporating dish at 60°C for 24 h. After grinding with an alumina mortar and pestle, a fine TiO_2 sample was obtained.

6.3.2. Characterization

The crystalline phases of the samples were evaluated using X-ray diffractometer (XRD-6100; Shimadzu Corp., Tokyo, Japan) operated at 40 kV and 30 mA. Chemical compositions were evaluated using an X-ray spectrometer (50 kV, 50 mA, RIX 2000; Rigaku Corp., Tokyo, Japan) equipped with Rh X-ray tube. The infrared spectra of hybrid powders were recorded using a Fourier transform infrared (FT-IR) spectrophotometer (8600PC; Shimadzu Corp., Kyoto, Japan) equipped with a diffuse reflectance measuring instrument (DRS-8000). The HPA peak intensity was very small; therefore, we used diffused reflectance method using TiO_2(ST-21) as a reference. The specific surface areas were evaluated using N_2 adsorption and desorption isotherms at 77 K (Autosorb-1; Quantachrome Instruments). The specific surface area was calculated using BET method. Solid acidity was evaluated using NH_3 adsorption. The NH_3-TPD spectra were measured

(TPD-65; Bel Japan). Measurements were made under conditions proposed previously by the Committee on Reference Catalyst in Japan Catalyst Society [24]. The sample (about 50 mg) was heat treated *in vacuo* at 500°C for 1 h, then cooled to 100°C before measurements. Then NH_3 gas was introduced to the sample and adsorbed at 100°C for 10 min. After vacuum evacuation, the sample was heated at 10°C/min with inflowing He carrier gas. The amount of desorbed NH_3 gas was detected using a mass spectrometer at 100–600°C. The measured amount of solid acidity was referenced using a standard zeolite catalyst (JRC-Z5-25H).

6.3.3. Photocatalytic activity

6.3.3.1. Standard gas preparation

Photocatalytic activity was evaluated using 2-propanol and HFC134a decomposition. Reagent-grade 2-propanol (99.5% purity; Wako Pure Chemical Industries Ltd., Tokyo, Japan) and high-pressure liquefied HFC gas (purity > 99.7%, HFC-134a; Daikin Industries, Ltd.) were used. For preparation of 2-propanol standard gas, we used the same method as that explained in chapter 5.2.1. **Figure 6-2** portrays the experimental procedure of HFC-134a gas dilution. After all air in a Tedrer® bag was pumped out using a syringe, the bag was filled with pure HFC-134a gas using a needle. Then, 10 ml pure HFC gas was injected into a 1 l sampling bottle and diluted. Consequently, 10^4 ppm standard gas was obtained.

6.3.3.2. 2-propanol decomposition

Photocatalytic activities of ST-21 and ST-21-PW_{12} hybrid powders were estimated using 2-propanol decomposition. A 50 mg powder sample was spread on a Petri dish.

Then it was illuminated with UV to remove surface organic molecules. **Figure 3-8** in **chapter 3** presents an illustration of settings used for this measurement. A Pyrex glass vessel (500 ml in volume) with a quartz glass lid was used as a batch reactor. The sample powder was set at the center of the vessel in a Petri dish; then the atmosphere in the reactor was replaced with 20ºC and 50% relative humidity air by gas flow (1.0 L/min, 10 min). Subsequently, the vessel was sealed and 2-propanol gas was injected into it. The injected gas amount was equivalent to that for 500 ppm concentration. The vessel was then stored in the dark. During this dark storage, the 2-propanol concentration decreased because of the molecules' adsorption on the sample and the vessel surface. The concentration change was monitored using a gas chromatograph (GC-14A; Shimadzu Corp., Tokyo, Japan), which was equipped with a flame ionization detector (FID) and a Sunpak-A column (Shimadzu Corp.). The carrier gas was nitrogen; the respective temperatures for the detector and injection port were 230°C and 200°C. The time program of the column oven temperature is presented in **Fig. 5-3** in **chapter 5**. After adsorption, the equilibrium was confirmed. Then UV illumination was carried out using a UV illuminator (LA-410UV-1; Hayashi Watch Works Co. Japan) equipped with a Hg-Xe lamp (MX4010). The light wavelength distribution is presented in **Fig. 5-4**. The illumination intensity at the powder surface was 1 mW/cm^2 at 365 nm. Concentrations of 2-propanol, acetone, and CO_2 were evaluated every 30 min for 6 h.

6.3.3.3. HFC-134a decomposition

The HFC-134a decomposition was carried out using ST-21, ST-21-PW_{12} hybrids, and dried STS-100. First, a 100 mg powder sample was spread on a Petri dish and pretreated with UV for 1 h. After sample setting in a 500 ml glass batch reactor, the inside atmosphere replaced with 20°C and 50% relative humidity air using gas flow. Then 2.5 ml standard gas (10^4 ppm) was injected into a glass vessel; the injected HFC was about 50 ppm. The reactor was kept in dark conditions for 2.5 h. Then adsorption at the equilibrium was confirmed and UV illumination (1, 5, 10 mW/cm^2) was carried out. The concentration change was monitored using gas chromatography equipped with FID and a Sunpak-A column (Shimadzu Corp.). The carrier gas was nitrogen. The respective temperatures for the detector and injection port were 230°C and 200°C. The time program of the column oven temperature is depicted in **Fig. 6-3**. Concentrations of HFC-134a were evaluated every 30 min for 6 h.

6.4. Results and discussion

6.4.1. PW_{12}-TiO_2 hybrid powder sample

Figure 6-4 depicts the XRD pattern of the PW_{12}-TiO_2 hybrid samples and reference TiO_2 powder. Hereinafter, hybrid samples with added 0.06 g, 0.1 g, and 0.5 g of PW_{12} are described respectively as hybrid-1, hybrid-2, and hybrid-3. Only anatase phase was identified in these hybrid powders; no HPA peak was observed. Actually, PW_{12} was not crystallized on TiO_2 powder, which indicated that the supported amount of PW_{12} was expected to be small and that PW_{12} was well-dispersed on the TiO_2 surface. Furthermore, the crystallinity of ST-21 did not change after hybridization with PW_{12}. This figure also shows that the STS-100 powder has lower crystallinity than either the ST-21 or ST-21 hybrid. **Figure 6-5** presents IR spectra of hybrid samples and PW_{12} K salt. Characteristic PW_{12} peaks (P-O stretching at 987 cm^{-1} and W-O stretching at 895 cm^{-1}) remained after hybridization. They reflect that the PW_{12} Keggin structure was maintained after hybridization. However, W-O-W bending was too weak to observe. **Table 6-5** portrays the chemical compositions, specific surface areas (SSA), and acid amounts of the starting material and the hybrids. Calculated and measured W/Ti ratios are depicted in Fig. 6**-6**. The starting material ratio was used for calculation. The ratio increased with increasing PW_{12} amount. When 0.5 g PW_{12} was used, W/Ti was less than the starting ratio; saturated adsorption might have occurred and excess PW_{12} might have been washed out from TiO_2 surface [25, 26]. The SSA decreased concomitantly with the supported PW_{12} increase. Two plausible explanations exist for that phenomenon. One is that the gap separating particles was filled with PW_{12}. The other explanation is a sample weight change caused by PW_{12} loading. Tungsten is a heavy atom. For that reason, the sample weight was increased and the surface area per unit of mass was decreased by PW_{12} loading. The same explanation is applicable to the acid amount change. Hybrids had a higher acid amount than the starting material (**Table 6-5**). Hybrid-3 contained about three times more W than hybrid-1. Nevertheless, they exhibited almost identical acid amounts. The acid amount and sample weight are expected to change concomitantly.

6.4.2. Photocatalytic activity

Photocatalytic activities of hybrid-1, hybrid-3, and ST-21 were evaluated according to the 2-propanol decomposition. **Figure 6-7** portrays the concentration changes of 2-propanol, acetone, and CO_2 during illumination. In this figure, C_0 represents the initial concentration of 2-propanol after dark storage. For acetone, $C/C_0 = 1$ was defined as the initial concentration of 2-propanol. The CO_2 concentration was represented by increased amounts from the beginning of illumination ($t = 0$) because the atmosphere in the glass reactor contained CO_2 even before illumination. During dark storage, 2-propanol was adsorbed onto the sample and walls of the glass vessel. Actually, C_0 was found to be 144 ppm for ST-21, 110 ppm for hybrid-1, and 121 ppm for hybrid-3. The PW_{12} supported samples had lower surface area than the reference ST-21, but they show high 2-propanol adsorption activity. Apparently, PW_{12} acted as an adsorbent in the hybrid system. In this experiment, hybrid powders show higher 2-propanol decomposition activity than the starting material. The decomposition rate (k) was calculated using 2-propanol concentration change and the equation $C(t) = C_0 - kt$. The order was the following

hybrid-1 > ST-21 > hybrid-3.

The calculated values of k were 70.3 ppm h^{-1}, 65.7 ppm h^{-1} and 60.6 ppm h^{-1}. Comparing the PW_{12}-TiO_2 hybrid powders, a small amount of PW_{12} increased the decomposition rate. Generally, an appropriate adsorbent amount on the TiO_2 surface accelerated decomposition. However, too much adsorbent prevented a TiO_2 surface reaction and decreased the decomposition rate. Hybrid-1 showed the best balance for rapid decomposition.

Acetone generation depended on the PW_{12} amount. Actually, the maximum concentration changed with the PW_{12} amount.

ST-21 > hybrid-1 > hybrid-3

In fact, C/C_0 for acetone was greater than 1 because of large amount of 2-propanol that had adsorbed onto the photocatalyst at $t = 0$ was decomposed. In both TiO_2 and PW_{12} photodecomposition processes, acetone is the first detectable intermediate by gas chromatography [27, 28]. The total generated acetone amount was not expected to be different. However, the acetone concentration in a glass vessel decreased concomitantly with increased PW_{12}. Results indicate that a part of the acetone was adsorbed onto PW_{12}. Especially in the hybrid-3 experiment, the maximum acetone concentration was the lowest. However, the generated CO_2 amount after 6 h is the smallest among three samples.

Acetone or decomposition intermediates are expected to remain on the catalyst surface. They did not decompose completely. The acetone decomposition rate was changed by PW_{12} support. However, it is difficult to discuss that effect because the adsorption and decomposition contributions to concentration change are only slightly separated.

Photocatalytic decomposition of HFC was carried out using hybrid-1 and ST-21 reference samples. **Figure 6-8** depicts the HFC concentration change during illumination. The value of C_0, the initial concentration of HFC-134a after dark storage, was 37 ppm for ST-21 and 36 ppm for hybrid-1. The adsorption amount was not changed by PW_{12} support, in contrast to the 2-propanol case. For the ST-21 reference sample, the decomposition rate increased with light intensity (**Fig. 6-8(a)**). In contrast, hybrid-1 showed complex light dependency. Its decomposition rate was not so changed between 5 mW/ cm^2 and 10 mW/cm^2, however when the light intensity was 1 mW/cm^2. The HFC concentration did not change during day 2 (**Fig. 6-8(b))**. Results show that the respective rate-control steps of HFC decomposition were different between the 1 and 5 mW/cm^2 cases. In addition, the sample color change occurred during illumination. The color of hybrid sample surfaces changed gradually with illumination from white to yellow or brown. It was inferred that the deposition of intermediate compounds caused catalyst deactivation. **Figure 6-9** shows the hybrid-1 color change occurring before and after decomposition. The sample color strengthened with illumination time. In the reference sample, the sample color change occurred early in the decomposition step. However, the color disappeared after 6 h. In this case, the photocatalytic reaction decomposed the colored intermediates. Under UV intensity of 1–10 mW/cm^2, the ST-21 sample exhibited a higher decomposition rate than that of hybrid-1.

Using dried STS-100 powder, HFC-134a photocatalytic decomposition was carried out at 5 mW/cm^2 to investigate the relation between powder properties and HFC decomposition activity. A blank test without photocatalyst was also undertaken. Concentration changes of 2-propanol during illumination were compared with ST-21 and hybrid-1. Those results are presented in **Fig. 6-10**. After illumination, the STS-100 powder color became brown. However, the 2-propanol concentration remained unchanged. A photocatalytic reaction slightly occurred and deactivated TiO_2. Although STS-100 powder has the largest SSA (235 m^2/g) of all samples, its decomposition activity was very weak. The decomposition activity was dependent on powder properties, not only on the SSA.

Although the composition intermediates on the photocatalyst surface have been identified only slightly and the HFC-134a decomposition pathway has not been reported yet, we can discuss some inferences related to HFC-134a decomposition drawn from our data and those of previous reports. First, the adsorption amount of HFC-134a was not increased by PW_{12} support. Generally, PW_{12} absorbs alcohols, ketones, amines, and formed complexes; however, HFC-134a has poorer basicity than those compounds. For that reason, PW_{12} cannot function as an adsorbent. Secondly, PW_{12} can affect the HFC-134a decomposition. The decomposition pathway might be changed under such a high acidity condition. Thirdly, a possibility of lower reduction level of PW_{12} than TiO_2 was not favorable for HFC-134a decomposition. For CCl_4, the substance reduction is the expected initial step of photocatalytic decomposition. In such a case, Pt loading decreased the decomposition rate and O_2 absence is effective for increasing decomposition [29]. A similar trend might cause a low HFC-134a decomposition rate by hybrid-1. Finally, the generated radical species on the photocatalyst are expected to be changed by PW_{12}. In a TiO_2 photocatalytic reaction, many radicals are generated by reduction on the TiO_2

surface. Generated radical species and the amount must be changed from the TiO_2 case if PW_{12} acts as reduction site. Reduction on PW_{12} might prevent HFC-134a decomposition. In addition, Murakami and Dimon et al. reported that OH radical and that singlet oxygen generation amounts depend on the TiO_2 particle size [30–32]. Actually, STS-100's low reaction rate can be discussed from the perspective if particular radicals play important roles in HCF decomposition. Furthermore, for CCl_4 photocatalytic decomposition, substance reduction is the expected initial step of decomposition. In such a case, Pt loading decreases the decomposition rate.

The PW_{12}-TiO_2 hybrid was effective for 2-propanol and acetone decomposition, but it was not effective for HCF-134a decomposition. For HCF photodecomposition improvement, clarification of the decomposition pathway and active radical species are necessary. Thereafter, suitable catalyst design would be possible.

6.5. Conclusion

For the study described in this chapter, we prepared PW_{12}-TiO_2 hybrid photocatalyst for decomposition of HFC-134a. Hybrid-1 (W/Ti = 0.011) exhibited higher photocatalytic ability and high adsorption ability on 2-propanol decomposition. However, it exhibited a lower decomposition rate than the starting TiO_2 powder. Decomposition behavior was found to depend on organic substances. Because the PW_{12}-TiO_2 system is not a catalyst that is useful in all circumstances, an appropriate catalyst design is necessary for each case.

References

[1] McCulloch, A. *J. Fluorine Chem.*, **100**, 163-173 (1999).

[2] Molina, M. J.; Rowland, F. S. *Nature*, **249**, 810-812 (1974).

[3] Ravishankara, A. R.; Turnipseed, A. A.; Jensen, N. R.; Barone, S.; Mills, M.; Howard, C. J.; Solomon, S. *Science*, **263**, 71-75 (1994).

[4] Farman, J. C.; Gardiner, B. G.; Shanklin, J. D.; *Nature*, **315**, 207-210 (1985).

[5] UK Stratospheric Ozone Review Group, *Stratospheric Ozone, 1996, Sixth Report of the UK Stratospheric Ozone Review Group*; DETR, London (1996).

[6] Meyer, L.D. *IPCC/TEAP Special Report on Safeguarding the Ozone Layer and the Global Climate System: Issues Related to Hydrofluorocarbons and Perfluorocarbons*; Cambridge University Press: Cambridge (2005).

[7] http://www.env.go.jp/en/earth/ozone/laws.html, Ministry of the Environment Government of Japan.

[8] http://www.epa.gov/sab/panels/pfoa_rev_panel.htm, U.S. Environmental Protection agency, *SAB Review of EPA's Draft Risk Assessment of Potential Human Health Effects Associated with PFOA and Its Salts* (EPA-SAB-06-006).

[9] Kannan, K.; Corsolini, S.; Falandysz, J.; Oehme, G.; Focardi, S; Giesy, J. P. *Environ. Sci. Technol.*, **36**, 3210-3216 (2002).

[10] Takizawa, K.; Takahashi, A.; Tokuhashi, K.; Kondo, S.; Sekiya, A. *J. Fluorine Chem.*, **127,** 1547-1553 (2006).

[11] Takita, Y.; Tanabe, T.; Ito, M.; Ogura, M.; Muraya, T.; Yasuda, S.; Nishiguchi, H.; Shihara, T. *Ind. Eng. Chem. Res.*, **41**, 2585-2590 (2006).

[12] Tajima, M. ; Niwa, M. Fujii, Y. ; Koinuma, Y.; Aizawa, R.; Kushiyama, S.;

Kobayashi, S.; Mizuno, K.; Ohuchi, H. *Appl. Catal. B: Environ.*, **14**, 97-103 (1997).

[13] Ogata, A.; Kim, H.-H.; Futamura, S.; Kushiyama, S.; Mizuno, K. *Appl. Catal. B: Environ.*, **53**, 175-180 (2004).

[14] Watanabe, T.; Tsuru, T. *Thin Solid Films*, **516**(13), 4391-4396 (2008).

[15] http://www.env.go.jp/en/earth/ozone/gl199903.pdf, Office of Fluorocarbons Control Policy Global Environment Bureau Ministry of the Environment Government of Japan, *Guidelines on the Destruction of CFCs in Japan.* (1999).

[16] Sangchakr, B.; Hisanaga, T.; Tanaka, K. *Chemosphere*, **36**(9), 1985-1992 (1998).

[17] Théron, P.; Pichat, P.; Guillard, C.; Pétrier, C.; Chopin, T. *Phys. Chem. Chem. Phys.*, **1**, 4663-4668 (1999).

[18] Kutsuna, S.; Takeuchi, K.; Ibuki, T., *J. Atmospheric Chemistry*, **14**, 1-10 (1992).

[19] Ohtani, B.; Ueda, Y.; Nishimoto, S.; Kagiya, T.; Hachisuka, H. *J. Chem. Soc. Perkin Trans.*, **2**, 1955-1960 (1990).

[20] Kiselev, A.; Mattson, A.; Andersson, M.; Palmqvist, A. E. C.; Osterlund, L. *J. Photochem. Photobiol. A: Chem.*, **184**, 125-134, (2006).

[21] The Chemical Society of Japan, *Kagakubinnrann Kisohen,* 5th edition; Maruzen Corp. Ltd.: Tokyo, II-315-317 (2004) in Japanese.

[22] Hori, H.; Takano, Y.; Koike, K.; Takeuchi, K.; Einaga, H. Dnvirln. *Sci. Tech.*, **37**, 418-422 (2003).

[23] Hori, H.; Takano, Y. ; Koike, K.; Takeuchi, K.; Kutsuna, S.; Einaga, H.; Ibuki, T. *Appl. Catal. B: Environ.*, **37**, 333-340 (2003).

[24] The Committee on Reference Catalyst in Japan Catalyst Society, *Shokubai*, **33**, 249–260 (1991).

[25] Ozer. R. R., Ferry, J. L. *Environ. Sci. Technol.*, **35**, 3242-3246 (2001).

[26] Tachikawa, T.; Tojo, S.; Fujitsuka, M.; Majima, T. *Chem. Eur. J.*, **12**, 3124-3131 (2006).

[27] Larson, S. A.; Widegren, J. A.; Falconer, J. L., *J. Catal.*, **157**, 611-625 (1995).

[28] Mylonas, A.; Hiskia, A.; Androulaki, E.; Dimotikali, D.; Papaconstantinou, E., *Phys. Chem. Chem. Phys.*, **1**, 437-440 (1999).

[29] Tomkiewietz, M.; Yoneyami, H.; Hori, Y.; Haynes, R. *Environmental Aspects of Electrochemistry and Photoelectrochemistry*; The Electrochemical Society: Pennington, 112-121 (1993).

[30] Murakami, Y.; Endo, K.; Nosaka, A. Y.; Nosaka, Y. *J. Phys. Chem. C*, **111(**30**)**, 11339-11346 (2007).

[31] Daimon, T.; Hirakawa, T.; Kitazawa, M.; Suetake, J.; Nosaka, Y. *Appl. Catal. A: General,* **340**, 169-175 (2008).

[32] Daimon, T.; Nosaka, Y. *J. Phys. Chem. C*, **111**, 4420-4424 (2007).

Table 6-1. Ozone depleting substances already phased out under the Montreal Protocol [1]

Compound	Chemical formula	b. p.	Atmospheric lifetime (yr)	ODP* relative to CFC-11	GWP* relative to CO_2
CFC-11	CCl_3F	23.8	50	1	4000
CFC-12	CCl_2F_2	-29.8	102	1	8500
CFC-113	CCl_2FClF_2	47.6	85	0.8	5000
CFC-114	$CClF_2CClF_2$	3.6	300	1	9300
CFC-115	$CClF_2CF_3$	-38.7	1700	0.6	9300
Halon-1211	$CBrClF_2$	-4	20	3	no data
Halon-1301	$CBrF_3$	-57.8	65	10	5600
Carbon tetrachloride	CCl_4	76.8	42	1.1	1400
Methyl chloroform	CH_3CCl_3	74.1	5.4	0.1	110

*ODP: Ozone depletion potential
*GWP: Global warming potential

Table 6-2 Ozone depletion substances scheduled for phase-out under the Montreal Protocol [1]

Compound	Chemical formula	b. p.	Atmospheric lifetime (yr)	ODP relative to CFC-11	GWP relative to CO_2
HCFC-22	$CHClF_2$	-40.8	13.3	0.055	1700
HCFC-123	$CHCl_2CF_3$	27.1	1.4	0.022	93
HCFC-124	$CHClFCF_3$	-12	5.9	0.022	480
HCFC-141b	CH_3CCl_2F	32	9.4	0.11	630
HCFC-142b	CH_3CClF_2	-9.2	19.5	0.065	2000
HCFC-225ca	$CHC_{l2}CF_2CF_3$	51.1	2.5	0.025	170
HCFC-225cb	$CHFClCF_2CF_2Cl$	56.1	6.6	0.033	530

Table 6-3. CFC and HFC alternatives: emissions control under the Kyoto Protocol [1]

Compound	Chemical formula	b. p.	Atmospheric lifetime (yr)	ODP relative to CFC-11	GWP
HFC-23	CHF_3	-82.1	264	0	11700
HFC-32	CH_2F_2	-51.7	5.6	0	650
HFC-125	CHF_2CF_3	-48.5	32.6	0	2800
HFC-134a	CH_2FCF_3	-26.5	14.6	0	1300
HFC-143a	CH_3CF_3	-47.6	48.3	0	3800
HFC-152a	CH_3CHF_2	-24.7	1.5	0	140
HFC-227ea	CF_3CHFCF_3	-16.5	36.5	0	2900
HFC-236fa	$CF_3CH_2CF_3$	-0.7	209	0	6300
HFC-245ca	$CHF_2CF_2CFH_2$	25.4	6.6	0	560
HFC-43-10mee	$CF_3CHFCHFCF_2CF_3$	45	17.1	0	1300
PFC-218	$CF_3CF_2CF_3$	-36	2600	0	7000

Table 6-4 Practically used CFC and HFC decomposition methods [15]

Method	Temperature	Feature
Thermal decomposition	1000–1200°C	•Heating with other waste, liquid fuel, or cement
Super heated steam	800–1000°C	•Heating in super-heated steam •Restriction of acid gas generation
Plasma	10000°C	•Concentrated gas decomposition •Restriction of acid gas generation •Requirement of condition tuning
TiO_2 catalyst	400°C	•Relatively low temperature •High efficiency

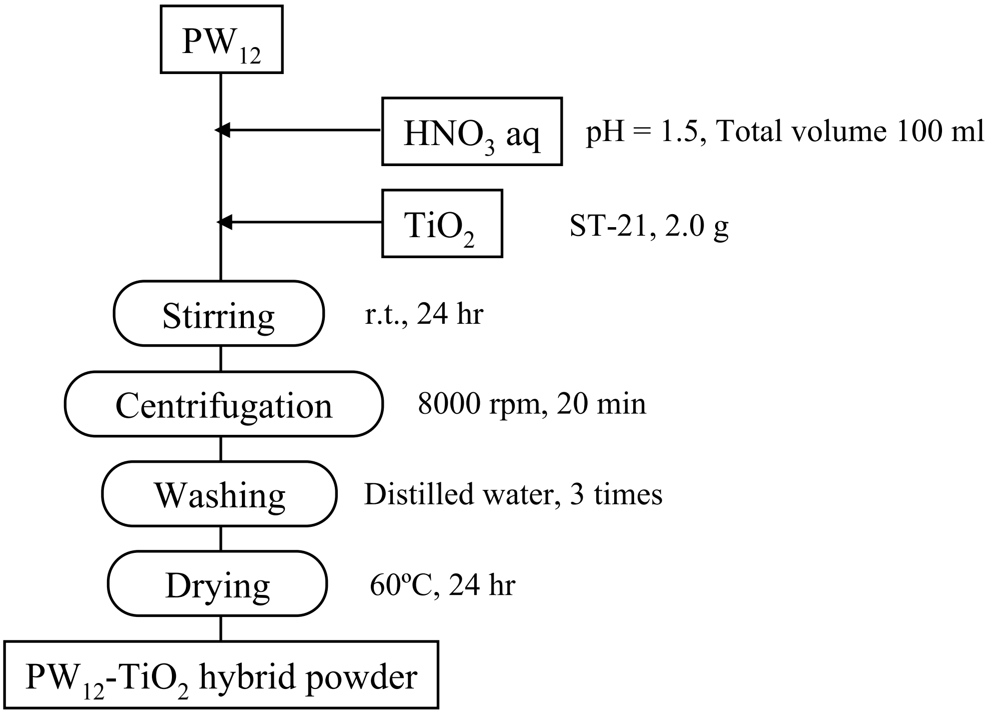

Figure 6-1. Experimental procedure of PW_{12}-TiO_2 hybrid powders.

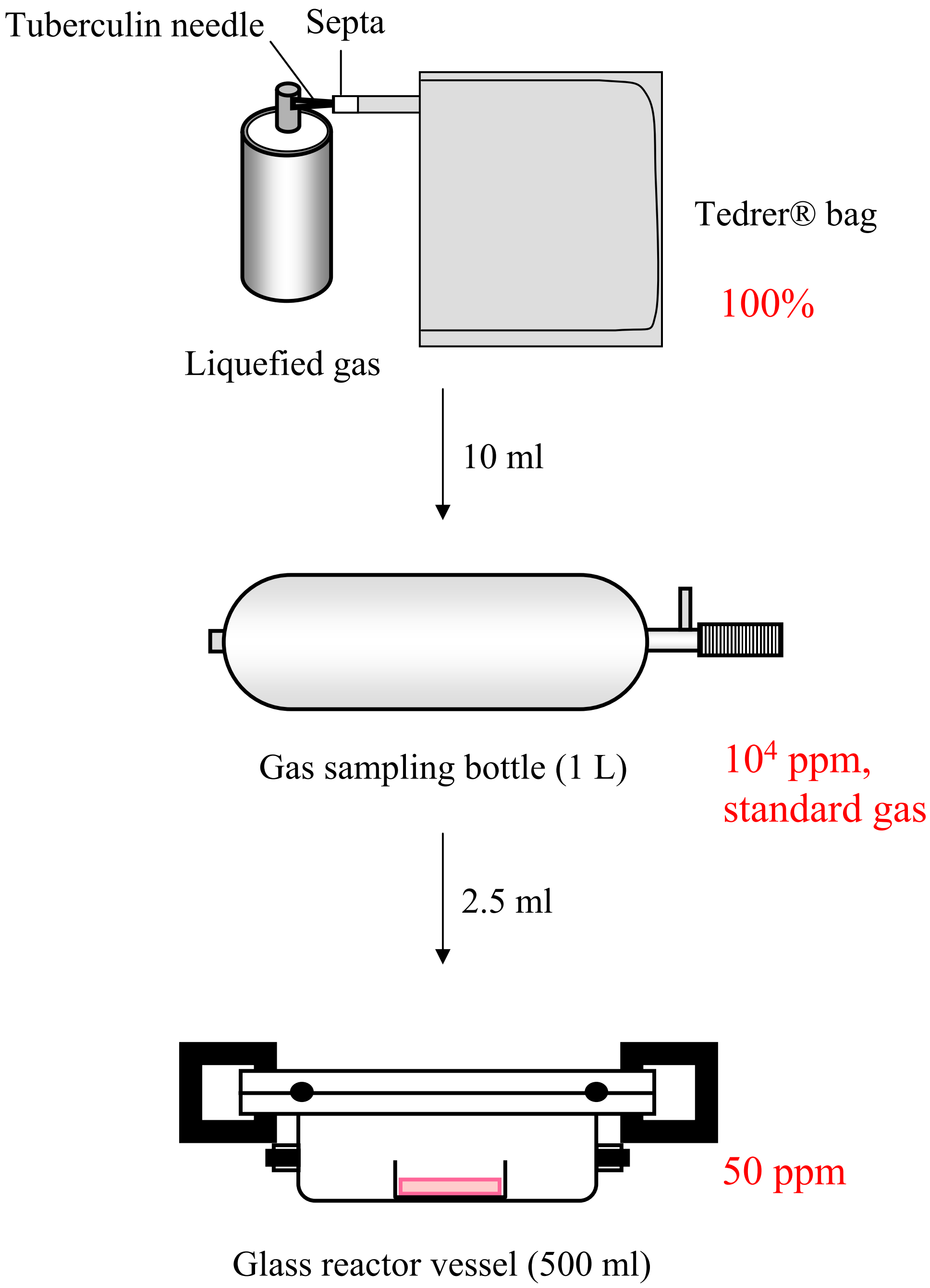

Figure 6-2. Schematic illustration of HFC-134a standard gas preparation.

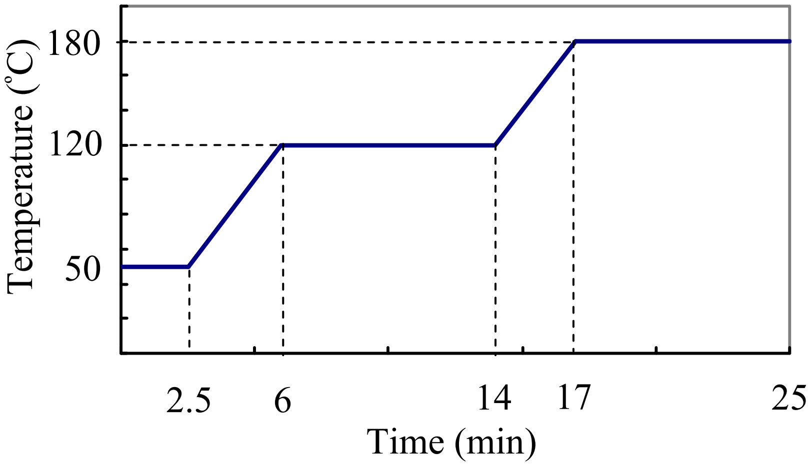

Figure 6-3. Temperature diagram of gas chromatography column oven during analysis.

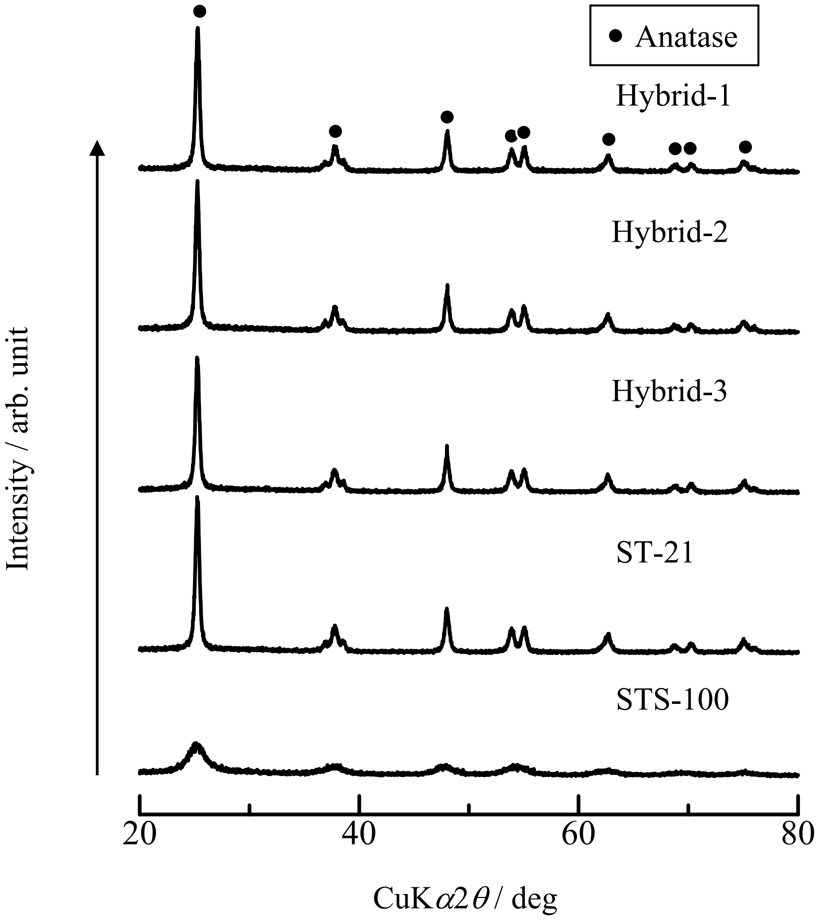

Figure 6-4. XRD patterns of hybrids and reference TiO_2 powders.

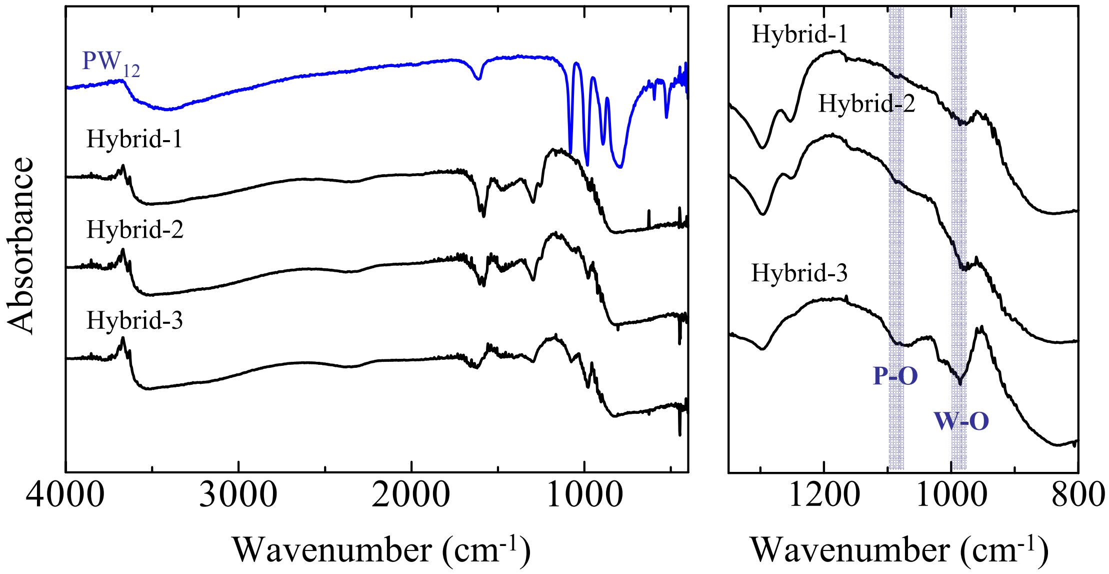

Figure 6-5. IR spectra of PW_{12} K salt (KBr method) and hybrid samples (diffuse reflectance method using ST-21 as reference): 1080 cm^{-1}, P-O stretching; 987 cm^{-1}; W-O stretching, 895 cm^{-1}; W-O-W bending.

Table 6-5. Hybrid and reference sample properties

Sample name	PW_{12} (g)	W/Ti	SSA (m^2/g)	Acid amount (mmol/g)
ST-21 and PW_{12}-TiO_2 composite				
Hybrid-1	0.06	0.011	70	0.136
Hybrid-2	0.1	0.016	69	No data
Hybrid-3	0.5	0.030	62	0.137
ST-21	0	0	72	0.0971
STS-100				
Dried STS-100	0	0	235	0.0747

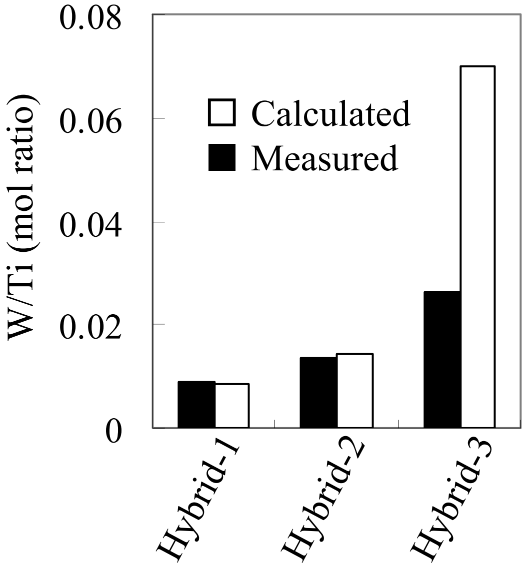

Figure 6-6. W/Ti ratio of the hybrid samples measured using XRF and calculated values.

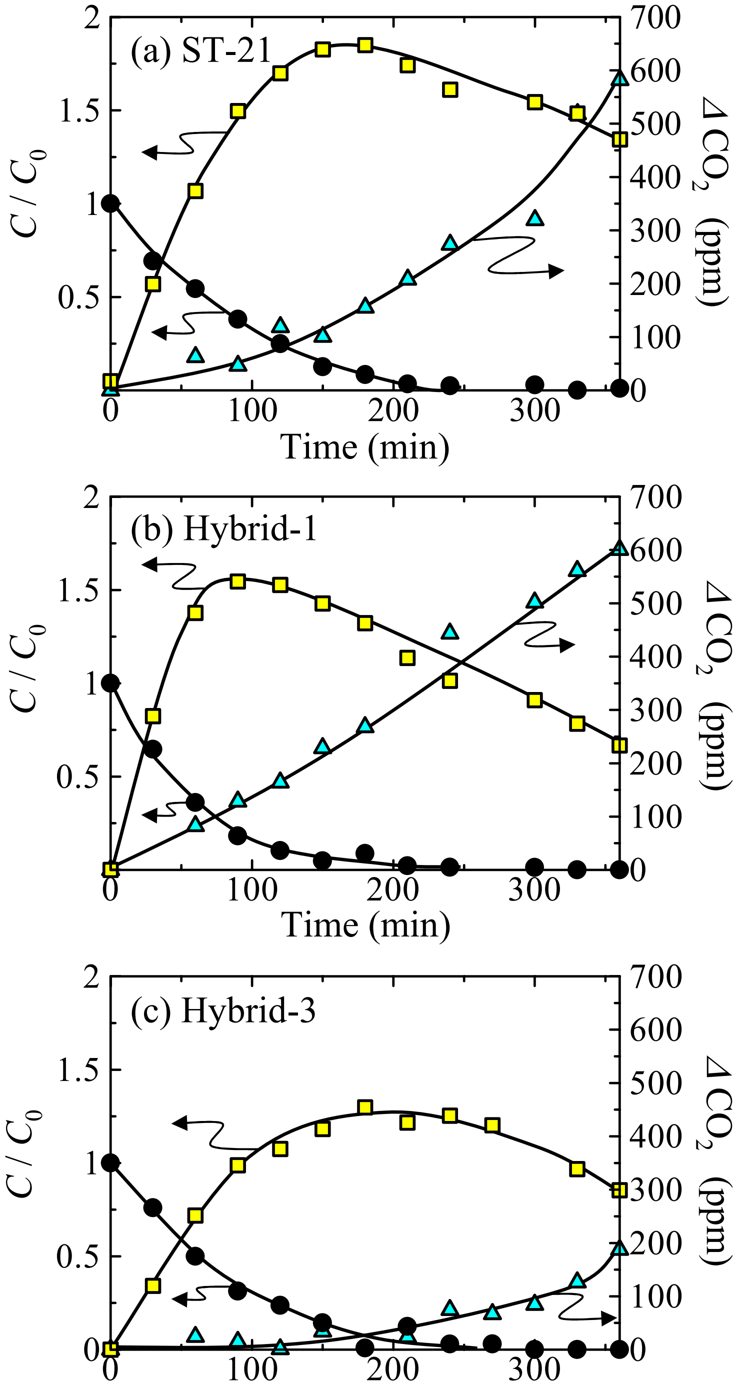

Figure 6-7. Concentration change of 2-propanol, acetone, and CO_2 during illumination: ●, 2-propanol; □, acetone; △, CO_2

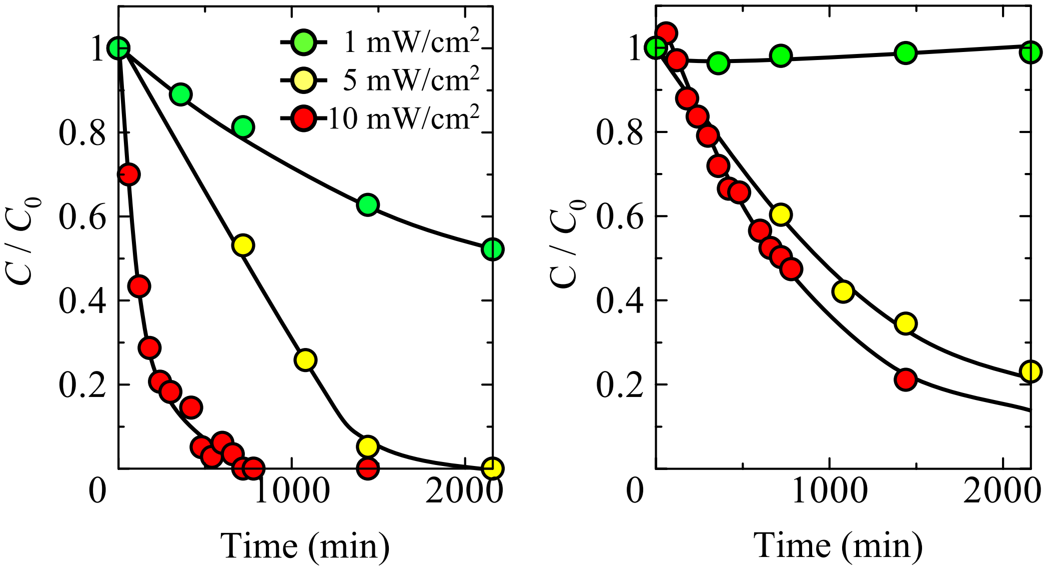

Figure 6-8. HCH-134a concentration change during illumination under 10, 5, 1 mW/cm^2 at 365 nm: (a) ST-21, (b) Hybrid-1.

Before illumination After illumination (48 h)

Figure 6-9. Sample color change after illumination. Sample: hybrid-1, 1 mW/cm^2 light intensity (365 nm).

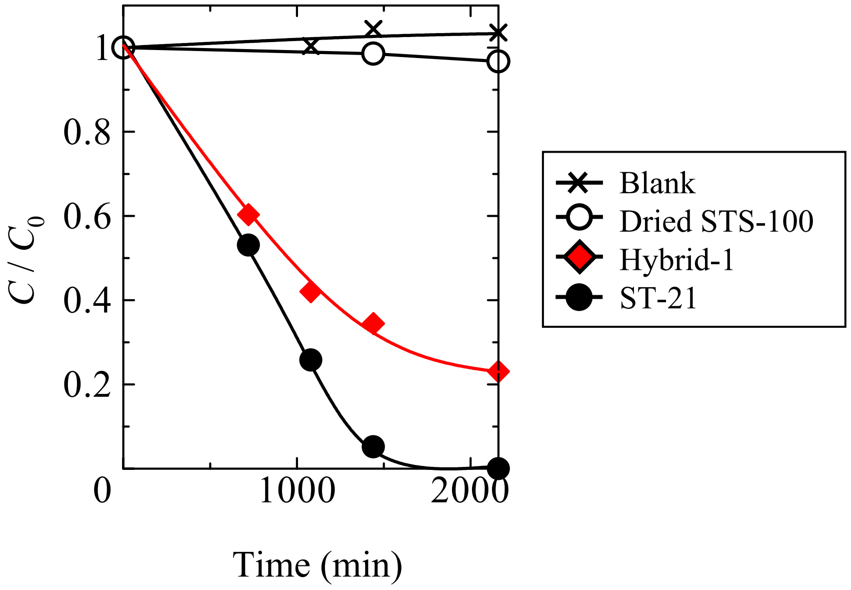

Figure 6-10. HFC-134a concentration change under 5 mW/cm^2 illumination.

CHAPTER7

Summary

7.1. Results and conclusions

For the increase of photocatalytic decomposition activities, various approaches are useful depending on the reaction phase, compounds, and concentration. In this work, we prepared functional TiO_2 coatings using electrophoretic deposition (EPD) and layer-by-layer (LBL) method. Organic compound decomposition was carried out. Through circulation of substances in porous EPD coatings, aqueous phase 1,4-dioxane decomposition was accelerated. On the other hand, heteropolyacid/TiO_2 hybrid thin films prepared using LBL method showed high decomposition activities in gaseous phase because of electron scavenger effects and two-step electron excitation. The outline, results, and conclusions of each chapter can be summarized as follows:

CHAPTER 1: A historical overview of TiO_2 photocatalyst was presented and recent topics in fundamental and application studies were introduced. From discovery of the Honda–Fujishima effect in 1972, TiO_2 photocatalysts have been investigated as a method of energy conversion, a material for environmental purification, and as photo-induced hydrophilic surfaces. Great effort has gone into increasing its photocatalytic activities. For effective environmental purification, low affinity between TiO_2 surface and organic molecules and low charge separation efficiency are salient problems. Especially for aqueous phase reaction, the decomposition rate was very slow; it has not been sufficient for practical use. In previous works, hybridization of TiO_2 with functional materials and combination with external field or other methods were carried out for increasing decomposition performance. However, in those studies, nano–micro-scale catalyst design based on the decomposition condition was absent. The objective of this study is the increase of TiO_2 photocatalytic activities from the approach of nano–micro-level structure and adsorption field design.

CHAPTER 2: In this chapter, purification of 1,4-dioxane contaminated water using porous TiO_2 coatings and voltage application was studied. Crack-free porous TiO_2 coatings were prepared on a stainless steel mesh using electrophoretic deposition (EPD) method for use as an electrode. The TiO_2 coating possessed submicrometer size pores, through which substances moved. When voltage was applied to the TiO_2 coated electrode, molecules were attracted to the inner stainless steel substrate and interrupted the coating. Adsorption experiments using a TiO_2 coated electrode revealed 1,4-dioxane; the EGDF attracted oppositely charged electrodes. Negative voltage application is effective for 1,4-dioxane decomposition; positive voltage application is effective for EGDF decomposition. Therefore, we used the voltage swing method to accelerate diffusion near the illuminated coating surface. The response of 1,4-dioxane and EGDF is different; the concentration of 1,4-dioxane decreased with decreasing voltage swing interval, but the change was small. In contrast, the EGDF concentration was changed remarkably by changing the interval. Moreover, the concentration of EGDF increased with the decreasing interval. These results suggest that the diffusion constant of EGDF molecules in the pore structure differs from that of 1,4-dioxane, and that the response to the voltage swing interval depends on the chemical species.

CHAPTER 3: In this chapter, heterogeneous photocatalyst was prepared using

Keggin-type heteropolyacid: 12-tungstosilicic acid (SiW_{12}), and layered double hydroxides (LDHs). Ion-exchange method and reconstruction method were employed for hybrid synthesis. Results of IR and chemical analyses suggest that SiW_{12} anion $[SiW_{12}O_{40}]^{4-}$ was hydrolyzed to $[SiW_{11}O_{39}]^{8-}$ during ion change and reconstruction. The photocatalytic activity of $[SiW_{11}O_{39}]^{8-}$-Zn_2Al LDH composite was quite low in gaseous 2-propanol decomposition. Because of the low accessibility and UV screening, the photocatalytic reaction in interlayer gallery might not improve well.

CHAPTER 4: In this chapter, Keggin-type polyacid and TiO_2 hybrid transparent thin films were prepared using LBL method. Actually, 12-tungstophosphoric acid (PW_{12}), 12-tungstosilicic acid (SiW_{12}), and ammonium metatungstate (H_2W_{12} ammonium salt) were used for hybrid preparation. Transparent thin films and reference TiO_2 and PW_{12} thin films were obtained using LBL method. Both IR and UV-vis absorbance spectra showed that alternative deposition occurred and that the Keggin structure was maintained after coating. The TiO_2 deposition amount decreased concomitantly with the increased polyanion charge. The repulsion force between polyanions and the surface charge balance with TiO_2 affect these phenomena.

CHAPTER 5: In this chapter, photocatalytic activities of the polyacid (XW_{12})-TiO_2 hybrid thin films $(XW_{12}/TiO_2)_n$ were evaluated using 2-propanol decomposition. The two-bilayer $(H_2W_{12}/TiO_2)_2$ and $(PW_{12}/TiO_2)_2$ films (ca. 15 nm) exhibited higher decomposition rates than that of the control $(TiO_2)_2$ film. Photocatalytic performance of the hybrid thin films was related to the Keggin-type polyacid redox property. Results of decomposition experiments indicate that the O_2 reduction rate on XW_{12} is important for overall decomposition performance. Wavelength-limited experiments revealed a Z-scheme reaction that is expected to occur in $(PW_{12}/TiO_2)_n$ films. The all-solid-state Z-scheme has rarely been reported. In fact, this is the first report of Z-scheme photocatalysis as a thin film. However, the $(SiW_{12}/TiO_2)_n$ and $(H_2W_{12}/TiO_2)_n$ films' decomposition rates did not change when visible light was cut. In these systems, O_2 reduction was not the expected rate controlling step. The photocatalytic decomposition activity also depends on the number of bilayer coatings, the top coating, and organic compounds for decomposition.

CHAPTER 6: In this chapter, using PW_{12}-TiO_2 hybrid powder and pure TiO_2 reference powders, 2-propanol and HFC-134a (CH_2FCF_3) decomposition was carried out and photocatalytic activities were evaluated. The PW_{12}–TiO_2 hybrid powder (W/Ti = 0.011) exhibited higher photocatalytic ability and high adsorption ability on 2-propanol decomposition, but it exhibited a lower decomposition rate than the starting TiO_2 powder. Differing trends between 2-propanol and HFC-134 are expected to originate from the difference of their decomposition mechanisms. Decomposition might not be initiated by oxidation caused by holes: in some cases, radicals or electrons start decomposition.

7.2. Key factors for environmental purification using TiO_2 photocatalysts

Water purification using TiO_2 photocatalysts

In aqueous phase photocatalytic decomposition, the reaction is commonly governed by diffusion. Therefore, adsorption and diffusion enhancement is as important as development of a photocatalyst that has high quantum efficiency. In addition, simple systems and TiO_2 support are desirable for practical use. In this study, we demonstrated voltage swing method increased decomposition rate. Microscale substance circulation was expected to occur in porous coatings. It accelerated diffusion near the reaction area. Flow and diffusion control in micro–nano-scale are unexplored areas of TiO_2 photocatalysis. Therefore, approaches undertaken at this scale present great potential for development of water purification. In our work, by changing adsorption field properties using applied voltage, substances' circulation occurred between the reaction field and adsorption field. Those fields were close, but they were separated by a thin porous TiO_2 coating. Such a space design is one example of a new and simple approach of decomposition enhancement. Space design of a reaction and adsorption field based on dominant factors of the decomposition, especially diffusion, is expected to be a key to effective enhancement of water purification.

Gaseous phase decomposition

In a gaseous phase reaction, increasing charge separation efficiency is considered an effective method for increasing the decomposition rate. Noble-metal loading is effective for charge separation. Notwithstanding, its high cost and difficulty in obtaining transparent film are barriers to its practical use. In this study, W-based Keggin-type heteropolyacids and isopolyacid are hybridized with TiO_2 nanoparticles and the transparent hybrid thin films exhibited higher decomposition activities than TiO_2 did; two-bilayer hybrid films exhibited 1.5 times higher decomposition rate than TiO_2 films did. Polyacids are inexpensive. Layer-by-layer systems require a very small amount of material (ca. nanogram-order). Furthermore, W-based Keggin anions are colorless. These facts suggest that W-base Keggin-type polyacids are attractive electron scavengers for

TiO_2 for a practical system. Transparency promises wide area application; the hybrid thin films show almost identical performance when used repeatedly. Problems that demand consideration are the following: PW_{12} and SiW_{12} are decomposed at high pH (>2 for PW_{12}, >6 for SiW_{12}). However, H_2W_{12} is stable at low to neutral pH; therefore, the materials used are expected to change depending on the decomposition condition.

The Z-scheme is considered to be an effective method for increasing photocatalytic activities. Nevertheless, few reports have described application of a Z-scheme for decomposition acceleration. This approach presents great advantages over doped TiO_2 and simple electron separation; the Z-scheme provides both strong reduction and oxidation power. From the perspective of visible light use, Z-scheme photocatalysis is an expectative system. In this thesis, direct evidence of electron transport from TiO_2 to PW_{12} was not obtained because very rapid steps and femtosecond or nanosecond spectroscopy are required for observation. In future works, such direct evidence will be obtained through spectroscopic studies.

From the discussion presented in chapter 5, O_2 reduction is important for photocatalyst design: two-electron and four-electron reduction are necessary to provide increased reduction potential for O_2. Catalysts which mediate multi-electron reduction can alter photocatalytic efficiency.

For HFC-134a decomposition using PW_{12}-TiO_2 hybrid powder and TiO_2 powder, different trends were apparent from those of 2-propanol decomposition. For HFC-134 decomposition, large TiO_2 particles (d = 20 nm) exhibited higher decomposition activity than fine particles (d = 7 nm) and electron scavenger hybrids (PW_{12}-TiO_2) This result suggests a completely different decomposition mechanism of HFC-134a from that of 2-propanol. A different catalyst design is necessary for effective decomposition of HFC

134a. First, reduction side reactions must be checked by controlling the atmosphere and addition of hole scavengers. The reaction rate was changed by these treatments if radicals and electrons initiate the decomposition. Subsequently, a new structure should be considered.

In this study, we presented some new approaches and proved their efficiency. However, as shown in chapter 6, no approach exists which can solve all problems: the appropriate catalyst design is changed depending on molecular properties and conditions. Selection of a method and optimization of photocatalytic systems, including their structure and chemistry, are necessary for effective decomposition.

List of Publication

1, Yanagida, S.; Nakajima, A.; Kameshima, Y.; K. Okada,

"Effect of Applying Voltage on Photocatalytic Destruction of 1,4-dioxane in Aqueous System"

Catal. Commun., **7**, 1042-1046 (2006)

(**related to CHAPTER 2**)

2, Yanagida, S.; Nakajima, A.; Kameshima, Y.; K. Okada,

"Voltage Swing Interval Effects on Photocatalytic Decomposition of 1,4-dioxane in Aqueous Media using TiO2-coated Stainless Mesh"

J. Ceram. Soc. Jpn., **116**[2], 181-186 (2008)

(**related to CHAPTER 2**)

3, Yanagida, S.; Nakajima, A.; Kameshima, Y.; K. Okada,

"Processing of W-based Heteropolyacid-LDH Composites"

J．Ion Exchange, **18**[4], (2007) p270-275

(**related to CHAPTER 3**)

4, Yanagida, S.; Nakajima, Sasaki, T.; A.; Kameshima, Y.; K. Okada,

"Processing and Photocatalytic Properties of Transparent 12 Tungsto(VI) Phosphoric Acid-TiO_2 Hybrid Films"

Chem. Mater., **20**[11], 3757-3764(2008)

(**related to CHAPTER 4 and 5**)

Acknowledgement

I would like to give my gratitude to my family for their daily support and encouragement. The present study was carried out under Research Fellow of the Japan Society for the Promotion of Science for Young Scientists (DC2; H19-9009). The present study was guided by Assoc. Prof. A. Nakajima in Tokyo Institute of Technology.

It gives me great pleasure to express my appreciation to Assoc. Prof. A. Nakajima and Prof. K. Okada for their careful guidance and advice for my study and life works. I wish to express my acknowledgement to Prof. T. Sasaki in National Institute for Material Science (NIMS) for his helpful advice on this study. I should like to acknowledge Dr. Y. Kameshima in Tokyo Institute of Technology for his careful support in the laboratory. I also would like to express my acknowledgement to Dr. T. Isobe in Tokyo Institute of Technology for his support as both a laboratory staff and a senior associate.

I wish to thank Ms. M. Kurihara in Tokyo Institute of Technology for support for office work and encouragement. I would like to express my appreciation for Dr. S. Suzuki who helped and advised me as a senior associate of a colleague in the laboratory. I would like to thank to Mr. N. Arimitsu and Ms. H. Asakura in Tokyo Institute Technology for their encouragement and good fellowship. I also would like to give my thanks to all the colleagues in the laboratory, especially, Mr. S. Matsui, Mr. T. koike, and Mr. Y. Akiyama who studied about photocatalyst in our laboratory. Finally, I am grateful to Prof. E. Sakai, Prof. M. Hara and Assoc. Prof. A. Nishikata in Tokyo Institute of Technology for their careful reviewing of this thesis.

Sayaka Yanagida